Characterization and application of isolated attosecond pulses

by

Hui Wei

B.E., Xian Jiaotong University, China, 2007

AN ABSTRACT OF A DISSERTATION

submitted in partial fulfillment of the
requirements for the degree

DOCTOR OF PHILOSOPHY

Department of Physics
College of Arts and Sciences

KANSAS STATE UNIVERSITY
Manhattan, Kansas

2017

Abstract

Isolated attosecond pulse (IAP) is a tool of probing electronic dynamics occurring in atoms, molecules, clusters and solids, since the time scale of electronic motion is on the order of attoseconds. The generation, characterization and applications of IAPs has become one of the fast frontiers of laser experiments. This dissertation focuses on several aspects of attosecond physics. First, we study the driving wavelength scaling of the yield of high-order harmonic generation (HHG) by applying the quantum orbit theory. The unfavorable scaling law especially for the short quantum orbit is of great importance to attoseond pulse generation toward hundreds of eVs or keV photon energy region by mid-infrared (mid-IR) lasers. Second, we investigate the accuracy of the current frequency-resolved optical gating for complete reconstruction of attosecond bursts (FROG-CRAB) and phase retrieval by omega oscillation filtering (PROOF) methods for IAP characterization by simulating the experimental data by theoretical calculation. This calibration is critical but has not been carefully carried out before. We also present an improved method, namely the swPROOF which is more universal and robust than the original PROOF method. Third, we investigate the controversial topic of photoionization time delay. We find the limitation of the FROG-CRAB method which has been used to extract the photoionization time delay between the $2s$ and $2p$ channels in neon. The time delay retrieval is sensitive to the attochirp of the XUV pulse, which may lead to discrepancies between experiment and theory. A new fitting method is proposed in order to overcome the limitations of FROG-CRAB. Finally, IAPs are used to probe the dynamic of electron correlation in helium atom by means of attosecond transient absorption spectroscopy. The agreement between the measurement and our analytical model verifies the observation of time-dependent build up of the $2s2p$ Fano resonance.

Characterization and application of isolated attosecond pulses

by

Hui Wei

B.E., Xian Jiaotong University, China, 2007

A DISSERTATION

submitted in partial fulfillment of the
requirements for the degree

DOCTOR OF PHILOSOPHY

Department of Physics
College of Arts and Sciences

KANSAS STATE UNIVERSITY
Manhattan, Kansas

2017

Approved by:

Major Professor
Chii-Dong Lin

Copyright

Abstract

Isolated attosecond pulse (IAP) is a tool of probing electronic dynamics occurring in atoms, molecules, clusters and solids, since the time scale of electronic motion is on the order of attoseconds. The generation, characterization and applications of IAPs has become one of the fast frontiers of laser experiments. This dissertation focuses on several aspects of attosecond physics. First, we study the driving wavelength scaling of the yield of high-order harmonic generation (HHG) by applying the quantum orbit theory. The unfavorable scaling law especially for the short quantum orbit is of great importance to attoseond pulse generation toward hundreds of eVs or keV photon energy region by mid-infrared (mid-IR) lasers. Second, we investigate the accuracy of the current frequency-resolved optical gating for complete reconstruction of attosecond bursts (FROG-CRAB) and phase retrieval by omega oscillation filtering (PROOF) methods for IAP characterization by simulating the experimental data by theoretical calculation. This calibration is critical but has not been carefully carried out before. We also present an improved method, namely the swPROOF which is more universal and robust than the original PROOF method. Third, we investigate the controversial topic of photoionization time delay. We find the limitation of the FROG-CRAB method which has been used to extract the photoionization time delay between the $2s$ and $2p$ channels in neon. The time delay retrieval is sensitive to the attochirp of the XUV pulse, which may lead to discrepancies between experiment and theory. A new fitting method is proposed in order to overcome the limitations of FROG-CRAB. Finally, IAPs are used to probe the dynamic of electron correlation in helium atom by means of attosecond transient absorption spectroscopy. The agreement between the measurement and our analytical model verifies the observation of time-dependent build up of the $2s2p$ Fano resonance.

Table of Contents

List of Figures

List of Tables

Acknowledgments

I would like to give my sincere thanks for all people that have helped me in the past six years while I pursued my Ph.D. study and research.

First of all, I would like to express my immense gratitude to my advisor, Dr. Chii-Dong Lin, for giving me an opportunity to pursue my Ph.D. degree in Kansas State University. His guidance and encouragement have been constantly encouraging and directing me through difficulties in my study and life. He brought me to the field of ultrafast atomic physics and trained me to have a scientific way of thinking in doing research.

Secondly, I want to give my thanks to my committee members, Dr. Uwe Thumm, Dr. Artem Rudenko, Dr. Christine Aikens, and outside chairperson Dr. Behrooz Mirafzal, for their input whether in teaching classes which I took, or in the discussions we have had on various topics.

Thirdly, I would like to thank the previous and present members in Dr. Lin's group. Dr. Anh-Thu Le and Dr. Cheng Jin helped me to run and write computational programs when I joined this group. They gave me great support for my first study on high-order harmonic generation. Dr. Toru Morishita helped me to run his TDSE program. Dr. Zhangjin Chen gave me a lot of advice on computational skills. Dr. Xu Wang, Dr. Qianguang Li, Dr. Chao Yu, Dr. Song-Feng Zhao, Dr. Wei-Chun Chu and Dr. Xi Zhao also gave me constructive suggestions from which I benefited. All my group members have provided elements of an experience that will shape the rest of my life.

Also, I would like to thank the Physics Department for taking good care of my study life and broadening my experience with various seminars and meetings. I have gained many insightful ideas from the lectures given by Dr. Brett Esry and Dr. Carlos Trallero. I served as a teaching assistant for Dr. Larry Weaver during my first year. He has been gracious and

with whom working has most enjoyable. Dr. Guillaume Laurent has inspired me to work on attosecond pulse characterization.

Moreover, I would like to acknowledge my collaboration with people from other institutes. I thank Dr. Claudio Cirelli, Dr. Mazyar Sabbar, and Dr. Ursula Keller from ETH Zurich, Switzerland, for providing valuable discussions on photoionization time delay. I also thank Dr. Andreas Kaldun, Dr. Alexander Blättermann, Dr. Christian Ott, and Dr. Thomas Pfeifer from Max-Planck-Institut für Kernphysik, Heidelberg, Germany, for providing the experimental data of transient absorption spectra for helium from which we have verified our analytical theory of ultrafast dynamics of autoionization.

Last but not least, I would love to acknowledge my wife Dr. Chang Liu, and my parents and parents-in-law, for their continuous love and support.

Dedication

To my lovely wife Chang Liu, my precious daughter Emma, and my parents and parents-in-law.

Chapter 1

Introduction

Since the quantum picture of the world was established in the early 20th century, to probe the ultrafast motion of atoms or electrons in gas phase molecules or solids has been an intriguing topic for physicists, chemists and even biologists. As we know, atomic motions in molecules such as molecular transformation and chemical reaction are mostly on the femtosecond (10^{-15} second) time scale. In the 1980s, laser technology enabled the compression of optical pulses to sub-picosecond, then dynamical imaging of chemical reaction became possible. In 1985, photodissociation of the ICN molecule in gas phase was first studied using optical pump-probe spectroscopy by A. H. Zewails group[1]. Because of his extraordinary contribution of transient dynamic imaging, Zewail was awarded the 1999 Nobel Prize in Chemistry. The term "pump-probe" is prevailing in ultrafast experiments. Typically a "pump" pulse is used to initiate certain dynamics, for example, dissociation, and a "probe" pulse which arrives at different time delays with respect to the pump pulse is used to monitor such dynamics.

Chemists are interested in monitoring and controlling chemical reactions, while physicists have a long-lasting dream of making "movies" for electrons in atoms, molecules and condensed matter. A natural time scale of electron dynamics is on the order of attoseconds (1 as = 10^{-18} s). For example, we can estimate the period of the electron motion in the $1s$

orbital of atomic hydrogen to be 150 as. To make such electron movies requires a "camera" with a "shutter speed" on the order of attoseconds, that is, an attosecond light pulse. To support such a short duration, in the frequency domain the pulse should have a broad bandwidth which is usually in the extreme ultraviolet (XUV) or soft X-ray regime. Nowadays such broadband XUV emissions are produced by high-order harmonic generation (HHG)[2], which is a phenomenon when high-power (10^{14} W/cm^2) short-pulse lasers interact with noble gases. HHG is a dramatically nonlinear process that converts the laser frequency which is always in the infrared (IR) region to multiples of this fundamental frequency up to the XUV region. By manipulating the HHG process, either attosecond pulse train (APT)[3] or isolated attosecond pulse (IAP)[4] can be generated. Taking advantage of such novel attosecond techniques, in the past decade experimentalists have performed many pioneering investigations on atomic, molecular and solid-state physics, for example, on electron correlation effects[5], time delays in photoionization[6] and charge transfer in complex molecules[7]. These experimental results have triggered an intense theoretical activity, resulting in hundreds of experimental and theoretical publications. Attosecond science and technology have revitalized the traditional atomic and molecular physics. The generation and characterization of attosecond pulses as well as their applications in observing and controlling physical processes have become one of the fastest growing frontiers in laser research.

1.1 Generation of attosecond pulses

1.1.1 High-order harmonic generation

Attosecond pulses are inevitably produced in the process of HHG. HHG was first discovered in 1987 by using a KrF laser[8] and in 1988 by a Nd:YAG laser[9]. In the 1990s, high-power femtosecond Ti:Sapphire laser system[10] was developed and became the main technology for HHG experiments. A typical Ti:Sapphire laser has a central wavelength of about 800 nm (1.55 eV in photon energy). It can routinely produce nanojoule pulses with a few

optical cycles in duration. Using novel pulse compression techniques, the pulse duration can even reach 5 fs or shorter[11]. The pulses can be amplified to a few mJ or higher by chirped pulse amplification (CPA), and the carrier-envelope phase (CEP) of the femtosecond laser can be stabilized by using the $f-to-2f$ technique developed for optical frequency metrology[12]. The typical laser intensity on the gas target is on the order of 10^{14} W/cm^2. The corresponding electric field of the light is comparable with the internal Coulomb field in an atom. Therefore strong field theory instead of the pertubative theory was needed to explain the HHG phenomenon.

In 1965 Keldysh[13] suggested an alternative tunneling mechanism for strong field ionization under certain conditions. At modest laser intensities ($< 10^{14}$ W/cm^2), if the ionization potential is low compared with the frequency of the light and large compared with the electric field of the laser, the normal multiphoton excitation scheme for ionization via intermediate states applies. On the other hand, if the incident field is strong enough, the atomic potential can be significantly distorted to such an extent that a potential barrier is formed. Furthermore, if the light frequency is low enough such that the electron can respond to this changing potential, within a quasi-stationary approximation, the electron can tunnel out through a static potential barrier. Keldysh introduced a parameter known as the "Keldysh parameter"

$$\gamma = \sqrt{\frac{I_p}{2U_p}} \tag{1.1}$$

which determine whether the atom is ionized in the tunneling ($\gamma \ll 1$) or the multiphoton regime ($\gamma \gg 1$). In Eq. (1.1), I_p is the ionization energy of the target, and U_p is called the ponderomotive energy defined by (in atomic units)

$$U_p = \frac{E_0^2}{4\omega^2} \propto I\lambda^2. \tag{1.2}$$

Here E_0 and ω are the electric field strength and frequency, while I and λ are the peak intensity and wavelength of the laser, respectively. The tunneling ionization model is an

essential element in the theory of HHG.

A typical HHG spectrum starts with a fast decrease of intensity versus photon energy (or harmonic order), followed by a broad plateau that extends to the XUV region and then an abrupt cutoff. Theoretical understanding of HHG was initiated in 1992-1993 by Krause [14] and Corkum [15]. According to their works, a semiclassical theory named by "simple-man's model" or "three-step model" was built to explain the plateau behavior of the HHG spectrum. According to this model, in the strong laser field, an outermost electron is first tunnel ionized from the atom when the electric field of the laser is close to its peak during an optical cycle. Second, this electron is driven away from the nucleus. When the oscillating laser field changes its sign (about a quarter of an optical cycle later), the electron first decelerates, and then starts to re-accelerate back towards the parent ion. Therefore, the electron can gain a significant amount of kinetic energy, much larger than the fundamental photon energy. Third, the returning electron recombines with its parent ion, this kinetic energy plus the ionization potential can be released in the form of high energy photon. The semiclassical three-step model predicts that the cutoff position in the HHG spectrum followed a universal law of $I_p + 3.17U_p$. This model was confirmed by a quantum-mechanical treatment which includes quantum effects, such as the depletion of the ground state, wave packet spreading and interference, based on a strong-field approximation (SFA) by Lewenstein *et al*[16].

The geometries widely used in HHG is that a gas jet or a gas cell is positioned in a focused laser beam. The cutoff photon energy and the yield of HHG is determined by not only the single atom response but also the macroscopic phase matching, because both the laser and the generated harmonic fields propagate in the gaseous medium, and they are influenced by nonlinear effects such as dispersion, absorption, generation of plasma, and ionization[17]. Harmonic generation will be efficient only if the good phase-matching is achieved, requiring that the generated XUV field to be in phase with the laser-induced polarization over the medium's length.

The harmonic emission can be understood intuitively as ultrashort bursts emitted at each recollision of the electron with the parent ion, which takes place during every half optical cycle. Based on the semiclassical model, the recollision electrons can be separated by different quantum orbits. A quantum orbit is a semiclassical mapping of a moment of birth into a moment and energy of recollision. Especially, the electrons born in the same quarter optical cycle can be divided into two sets that generate the same XUV frequency: the electrons born closely after the field crest and returning between three-quarters to one optical cycle belong to the "long orbit"; the electrons born later and returning earlier belongs to the "short orbit". When considering macroscopic effects, either phase matching in the medium or spatial filtering in the far field tends to select the contribution of only one of these orbits, usually the short orbit contribution. As a result, harmonic radiation consists of a train of sharp short-wavelength pulses with sub-femtosecond duration (that is an APT), with only one pulse per half cycle. By symmetry, an APT only contains odd harmonics in the frequency domain. Experimentally, an APT with duration of 250 as was first demonstrated by Paul *et al.*[3] through HHG in Ar. The APT generated from HHG usually contains attochirp. The attochirp is the dispersion of XUV photon energy with emission time. If the short orbit is selected by phase matching, the harmonic emission time increases as photon energy increases, that is, the harmonics have positive attochirp, which leads to temporal broadening. To improve the harmonic synchronization, one can propagate the harmonics in a negative chirp medium to compensate the positive chirp introduced in the HHG process[18].

1.1.2 Generating isolated attosecond pulses using gating methods

In APTs, although each burst is of sub-femtosecond duration, the whole pulse train is still a few to tens of femtoseconds. For applications in dynamic systems that require sub-femtosecond temporal resolution one would need IAPs. To generate IAPs the fundamental laser must be CEP stable. The key issue is to isolate a single emission event in the HHG process. A few gating schemes have been applied to produce IAPs, and in the following we

briefly mention some of them.

Amplitude gating

In the amplitude gating approach the harmonic emission is spectrally filtered. For a short enough driving pulse, only the attosecond pulse generated by the most intense half cycle of the driving pulse, which corresponds to the cutoff portion of the HHG spectrum, can pass the high photon energy bandpass filter. For 800 nm laser, pulses as short as about 3.6 fs have been used for the generation of IAP. Using this method, with Ne as the target, IAP with central energy of 80 eV and pulse duration of 80 as has been reported[4].

Ionization gating

This method relies on generating harmonics using intense lasers beyond the saturation intensity. The neutral medium is completely depleted within the leading edge of the driving pulse. The leading edge of the driving pulse severely ionized the gas medium and creates a dense plasma. At the trailing half, plasma dispersion and the absence of neutral atoms turns off the harmonic emission. The gating obtained by confining the harmonic emission on the leading edge may not produce a very narrow pulse, thus additional spectral filtering is needed[19].

Polarization gating

The amplitude gating and ionization gating methods preclude the generation of IAPs with ultrabroad bandwidths because the usable cutoff spectrum typically covers a relatively small portion of the total spectrum. This limitation can in principle be overcome by using a half-cycle IR driving pulse. However, to synthesize such a pulse is difficult. On the other hand, it is possible to generate a long pulse where the polarization of the driving pulse is manipulated such that the rising edge and the trailing edge of the pulse are elliptically polarized, while the central cycle is linearly polarized, as originally proposed by Corkum *et al.*[20]. Harmonic

generation is sensitive to the ellipticity, thus the rising and the trailing edges of the pulse do not generate harmonics, and high harmonics are generated only from the central portion of the pulse which is linearly polarized. Using this polarization gating (PG) method, IAP as short as 130 as in the spectral range of 25-50 eV with an energy of 70 pJ was first generated and characterized in 2006[21].

A laser pulse with time-dependent ellipticity can be formed by combining a left-hand circularly polarized pulse and a right-hand circularly polarized pulse with a time delay T_d [22]. For such a pulse, the time interval wherein the ellipticity $\varepsilon(t)$ is less than a certain threshold ε_{th} can be given approximately by

$$\delta t_{PG} = \frac{\varepsilon_{th}}{\ln 2} \frac{\tau^2}{T_d}, \tag{1.3}$$

where τ is the duration of both circularly polarized pulses. Since harmonic yield drops by about a factor of two when the ellipticity changes from 0 to 0.13, and if we choose T_d about equal to τ, then the gate window where ε is less than 0.2 will be given by $\delta t_{PG} = 0.3\tau$. This gate window should be less than the time between two successive emissions. For a 800 nm driving pulse, this would require a pulse duration of about 5 fs. In other words, one would need to start with 5-fs circularly polarized light. Besides, taking into account the depletion of the ground state population by the circularly polarized leading edge, the PG method also requires short driving laser pulses.

To relax the need of using short pulses, one way is to change the period of HHG from half optical cycle to full optical cycle by adding a second harmonic with proper energy and phase to the driving laser. This method is called DOG (double-optical gating). For the same pulse energy this method will enhance the generation efficiency because of less ionization at the leading edge of the driving pulse. One can also use higher intensity driving laser to reach higher intensity IAP using DOG than the polarization gating method. In 2009 Mashiko *et al.*[23] reported the measurement of XUV bursts with a bandwidth of 200 eV that was generated by a main 8 fs-800 nm driving pulse and a second harmonic using the

DOG technique. To use even longer driving pulses, one can replace each of the circularly polarized pulse by an elliptically polarized light with ε about 0.5. This method is named by Generalized DOG (GDOG) and would allow IAPs with 148 as duration generated with 800 nm-28 fs driving pulses[24]. At present, the DOG method appears to be the most commonly used for IAP generation. Using 7 fs-750 nm-1 kHz Ti-Sapphire laser focused to 1×10^{15} W/cm^2 on Ne at high gas pressure, Zhao *et al.* reported 67-as pulses with energy centered at 80 eV[25].

Attosecond lighthouse

This method was first introduced by Vincenti and Quéré[26]. It is carried out by inserting a pair of glass prisms in the beam path before focusing to generate a time-dependent wavefront, a wavefront that changes directions continuously throughout the beam. With such rotating wavefront, each attosecond pulse generated in a train is emitted in a different direction. If the wavefront rotation within one half cycle of the driving laser field is larger than the divergence of the individual attosecond pulses, then each attosecond burst can be separated spatially. This method, known as "attosecond lighthouse", will prove a powerful resource for attosecond science. The method still requires relatively short pulses and has been demonstrated with a 5-fs CEP stabilized 800-nm laser[27].

1.1.3 Generation of attosecond pulses by mid-infrared driving lasers

For atomic physics, condensed matter, chemical and biological applications, it is important to extend the harmonic spectrum to the "water window", i.e., the photon energy range from 280 to 530 eV, between the K-absorption edge of carbon and oxygen. Such soft X-ray light sources will allow studying electron dynamics in materials containing carbon, nitrogen, oxygen and several other key elements using core-level transitions. The conventional 800-nm Ti:Sapphire laser is very inefficient to generate such a harmonic spectrum. According to

the semiclassical model, the cutoff energy of HHG is $I_p + 3.17U_p$ where $U_p \propto I\lambda^2$, therefore mid-IR driving sources seem promising for generating broadband attosecond pulses covering the water window. So far many mid-IR lasers for HHG and strong field experiments have been developed, exploiting the optical parametric amplification (OPA)[28–31] or optical parametric chirped pulse amplification (OPCPA)[32–35]. The typical central wavelength of the driving pulse lies in 1.5 to 2 μm. Unfortunately, the HHG yield scales roughly like $\lambda^{-(5-6)}$[36], then the efficiency of generating high-energy photons drops rapidly for mid-IR driving lasers. To overcome this unfavorable scaling law with driving wavelength, Popmintchev *et al.* improved phase matching by focusing the driving pulse into a hollow-core fiber filled with He gas at very high pressure[37]. The attochirp of the harmonics goes like $1/\lambda$[38], which implies that shorter attosecond pulses can be generated by mid-IR sources with respect to Ti:Sappire lasers.

Recently, IAPs reaching the carbon K-shell edge (284 eV) have been demonstrated using the attosecond lighthouse technique[39]. A two-cycle CEP-stabilized 1850 nm, 1 kHz, 230 μJ laser system is implemented with wavefront rotation to generate continuum harmonics. After filtering a broad spectrum covering 225 to 300 eV was observed. By spatiotemporal isolation an IAP was obtained with pulse duration estimated below 400 as. The PG method was also used to generate continuum harmonics from 50 to 450 eV by a two-cycle, 1.7 μm driving field obtained using OPCPA[40].

1.2 Characterization of attosecond pulses

The application of attosecond pulses requires the development of attosecond metrology. Because the power spectrum can be easily measured, the main task is to determine the spectral phase. Due to the low efficiency of HHG process, the energies of attosecond pulses are on the order of picojoules to nanojoules today. The low intensity as well as the broad bandwidth of attosecond pulses preclude the implementation of phase retrieval techniques

developed for femtosecond lasers that rely on nonlinear optical gating such as autocorrelation, spectral phase interferometry for direct electric field reconstruction (SPIDER)[41] or frequency-resolved optical gating (FROG)[42]. Because of the lack of effective nonlinear materials in the XUV region, up to date most of the attosecond pulse characterizations take advantage of the photoionization process. The phase retrieval of either APT or IAP relies on analyzing the photoelectron spectrum emitted from noble gas atoms ionized by the XUV pulse. To measure the phase, certain nonlinear processes are needed so that one can compare the spectral phase at different frequencies. This was fulfilled by adding a phase-locked IR laser field to the XUV photoionization process. Therefore the photoelectron is emitted when an atom absorbs an XUV photon and then absorbs (or emits) one or more IR photons. By changing the time delay τ between the XUV pulse and the IR field, a set of photoelectron spectra which is often called a spectrogram or a trace can be achieved. The information of the spectral phase of attosecond pulse has been embedded into the photoelectron spectrogram.

1.2.1 Phase retrieval for attosecond pulse trains

The phase retrieval method for APTs has usually been referred to as "reconstruction of attosecond beating by interference of two-photon transitions" (RABITT)[43] since the first observation of APT[3]. The intensities of the XUV harmonics are too weak to cause nonlinear effects, and thus only cause single XUV photon ionization processes. Without the IR field the photoelectron spectrum will show peaks at $E = (2q+1)\omega - I_p$ from the odd harmonics. Here ω is the fundamental frequency used to generate high harmonics. I_p is the ionization potential of the target. The delayed IR field is usually from the one that generates harmonics so it also has frequency ω. In the RABITT case its intensity is very low (typically less than 10^{12} W/cm^2). Thus the electron can only absorb or emit one IR photon, and the whole process can be treated by second-order perturbation theory. Due to the IR field, sidebands at $E = 2q\omega - I_p$ appear in the photoelectron spectrum. The

sidebands can be simply explained by two-path interference: the sideband S_{2q} comes from the electron ionized by $(2q-1)\omega$ harmonic followed by absorbing one IR photon, or ionized by $(2q+1)\omega$ harmonic followed by emitting one IR photon. Moreover, the sideband varies as we change the time delay τ between the XUV harmonics and the IR field, which can be calculated via the second order perturbation theory:

$$S_{2q} = A_{2q} + B_{2q}\cos\left[2\omega\tau + (\phi_{2q+1} - \phi_{2q-1}) + \Delta\phi_{2q}^{\text{atom}}\right]. \tag{1.4}$$

Here ϕ_{2q+1} and ϕ_{2q-1} are the phase of two neighboring harmonics. $\Delta\phi_{2q}^{\text{atom}}$ is an intrinsic phase for a given target atom, often called the atomic phase. This phase depends on the phase of matrix elements for above-threshold, two-photon ionization involved in the generation of the sideband, and thus can be calculated theoretically. Clearly by measuring the delay-dependent sideband signal, the phase difference between consecutive harmonics $\phi_{2q+1} - \phi_{2q-1}$ can be retrieved. The RABITT method has been employed for measuring the attochirp of harmonics on a broad spectral range[44].

1.2.2 Characterizing isolated attosecond pulses

IAP was first generated and measured by the attosecond streaking technique in 2001[45]. In the streaking measurement, the XUV pulse generates a replica of the amplitude and phase of this attosecond pulse in the form of an electron wave packet by single-photon ionization. The IR field acts as an ultrafast phase modulator that modulates the energy spectra of the photoelectrons as a function of the time delay between the XUV and IR pulses. Attosecond streaking can be understood classically[46]. After an electron is released to the continuum at the time t, it is accelerated by the electric field of the laser and thus gains energy from the time-dependent field from the moment of ionization to the end of the laser pulse. If the electron is released with a kinetic momentum $\mathbf{p}_0$, then the detected momentum after the turning off of the IR field can be predicted as $\mathbf{p}_0 - \mathbf{A}(t)$. Here $\mathbf{A}(t)$ is the vector

potential of the laser pulse which is assumed to vanish after the pulse is over. To retrieve the spectral phase of the XUV pulse from the streaking spectrogram, the "frequency-resolved optical gating for complete reconstruction of attosecond bursts" (FROG-CRAB)[47] was routinely used. If the IR intensity is weak like in the RABITT measurement, only one IR photon contributes to the photoionization. Then the second-order perturbation theory can be applied to analyze the spectrogram, which leads to another pulse characterization method called "phase retrieval by omega oscillation filtering" (PROOF)[48]. The FROG-CRAB and the PROOF method will be discussed in details in chapters 3 and 4 of this dissertation.

A different attosecond pulse characterization scheme is based on the implementation of all-optical methods. This method is based on *in situ* measurements[49, 50] where the production and the measurement of attosecond pulses are entangled. During the HHG process, a weak control field is used to perturb the trajectory of the re-collision electron. Using a perturbing field incident at an angle produces a modification to the phase of the re-collision electron wave packet, which varies as the detection is translated across the attosecond pulse wavefront. Therefore a spatial modulation can be induced on the attosecond pulse and information of the electron wave packets can be transferred into the XUV radiation. By measuring the far-field spatial profile of the XUV radiation at each frequency, it is possible to obtain a complete space-time characterization of attosecond pulses in the generation medium and in the far-field. Recently the attosecond lighthouse technique has been used to generate IAPs with 2-cycle 1.8 μm laser[51]. The spatial and temporal profile of each attosecond pulse were measured by the *in situ* method. The measurement confirmed that at the beam center the near-field pulse duration is 390 as and it increases to 420 as in the far field. The advantages of the *in situ* method lie in its very high detection efficiency and high signal-to-noise ratio, which allows single-shot measurement of the pulse. The drawback of this method is that only the pulse created in the generation medium can be measured. It is not applicable when the pulse has been filtered or transported.

So far none of these pulse characterization methods can measure the CEP of the attosec-

ond pulses. Liu *et al.*[52] have demonstrated theoretically that the photoelectron spectra generated by an IAP in the presence of an intense CEP-stable IR field (4.5×10^{13} W/cm^2) are sensitive to the CEP of the attosecond pulse. This CEP dependence can be understood in terms of the coherent superposition of two electron wave packets. The electron in the first wave packet comes from direct photoionization by absorbing one XUV photon, like in the standard situation of pulse characterization, while the electron in the second wave packet is released by the intense IR field and then re-scattered by the parent ion, which is the same as the above threshold ionization (ATI) electron. This sensitivity of the photoelectron spectrum to the CEP of the IAP makes some possibility of the CEP measurement, however such a measurement has not yet been demonstrated by experiment.

1.3 Probing ultrafast dynamics using attosecond pulses

Because of the rather low flux of attosecond pulses, the majority of attosecond experiments that have been performed up to now have been two-color XUV-IR experiments where the APT or IAP is combined with a delayed few-cycle IR pulse which serves as a clock. Charged particles such as photoelectrons and ions formed in experiments can be detected by multi-dimensional detectors such as the velocity map imaging (VMI) detectors[53] or the cold target recoil ion momentum spectroscopy (COLTRIMS) detectors[54]. Recently the attosecond transient absorption spectroscopy (ATAS)[55] was also developed which has become a popular method.

The ATAS is an all-optical technique which measures the XUV absorption spectrum. A typical experimental setup for ATAS is described in the following paragraph[56, 57]. A few-cycle near-IR pulse is first split by a beam splitter in an interferometer. One arm of the interferometer generates the attosecond pulse, while the other arm acts as the IR probe pulse. The IAP generating arm may apply a certain optical gating technique to manipulate the laser field, then the laser pulse enters the vacuum system and is focused

into a gas cell, in which the HHG process occurs. After this gas cell, an IAP is produced and propagates collinearly with the residual femtosecond laser field. This residual light is subsequently blocked by a metal foil, which also acts as a filter for the attosecond pulse spectral bandwidth. The attosecond pulse is then focused by a gold-coated grazing incidence toroidal mirror. The IR probe arm propagates outside the vacuum system. A relative delay can be introduced in this arm, and fused silica can be added for optimal pulse compression. The IR pulse is first focused by a spherical focusing mirror and then is recombined with the XUV pulse by a mirror with a small hole drilled in the center. The XUV pulse passes through the hole in the center of the mirror, while the IR pulse reflects off the mirror, resulting in an annular beam. The IR and XUV pulses are then overlapped spatially in a gas cell or jet where they interact with the sample. After passing through the sample, the IR pulse is blocked by a metal foil. The XUV pulse is dispersed by a grating and its spectrum is detected, typically by an X-ray CCD camera. The temporal resolution of a transient absorption experiment depends on the duration of the laser pulses used in the experiment while the resolution in the frequency domain depends on the energy resolution of the spectrometer. Therefore good temporal and frequency resolution can be achieved, and the ATAS can provide powerful details about line shapes, wave packet superpositions and decays.

In this section we briefly introduce a few important attosecond measurements using attosecond pulses.

1.3.1 Probing electron correlation effects

The first investigation of electronic correlation on the few-femtosecond timescale was reported in krypton using a sub-femtosecond XUV pulse centered around 97 eV by Drescher *et al.*[5]. Ionization can occur from the $3d$ shell and the excited ionic core relaxes through electron correlation by Auger decay, which leads to a doubly charged ion and the ejection of a second electron. Using a synchronized few-cycle IR pulse the time-resolved Auger decay

process was observed. The emission of the Auger wave packet in the continuum extends over several optical cycles of the IR field due to the lifetime of the excited state. By measuring the delay dependence of the sideband signal corresponding to the main Auger line, a lifetime of 7.9 fs was estimated. This value corresponds to a line width of 88 ± 10 meV which is in good agreement with the previous spectroscopic measurement.

The ATAS has been used to measure the dynamics of the two bound and correlated electrons in helium atoms[58]. In this experiment the manifold of autoionizing states below the $N = 2$ ionization threshold was excited by a broadband IAP and the time evolution of the two-electron wave packet was observed by using a synchronized IR pulse. The IR pulse can couple the two lowest-lying autoionizing states ($2s2p$ and $sp_{2,3+}$), and the quantum beat among these two states was observed as a modulation of the absorption spectrum with a period of 1.2 fs. From the beating one could retrieve the relative phase between the two autoionizing components in the two-electron wave packet, and thus the time-dependent real-space correlated electronic motion involving these autoionizing states can be visualized. It was also demonstrated that the correlated electronic motion is not only probed but also controlled by the intense IR field. The Fano line shape of the autoionizing states can be strongly modified as the intensity of the IR pulse varies[56].

Attosecond spectroscopy also allow us to observe and order sequential relaxation processes, that is, the ion-charge-state chronoscopy. If an intermediate ionic species of charge is formed as the result of photoionization or of Auger decay, the synchronized IR pulse can probe its formation and decay time and thus determine a variation in the yield of multiply charged ions. The relaxation processes of highly excited xenon[59] and krypton[60] atoms have been investigated by attosecond technique.

1.3.2 Delay in photoemission from atoms and solids

The interaction of XUV pulses with atoms or solids can lead to electron emission from different atoms in mixture of gases, from different orbitals within the same atom, or from

different band features of surfaces or solid-state materials. In a pioneering experiment done by Schultze *et al.*[6], the photoionization "time delay" from the $2p$ and $2s$ subshells of Ne was measured by attosecond streaking method. The IAP used in this experiment was centered at 106 eV with a full width at half maximum (FWHM) bandwidth of 14 eV, which supports a pulse duration below 200 as if it is transform-limited (TL). Near-single-cycle IR pulses (750 nm in wavelength, 3.3 fs in FWHM duration) were used, with peak intensities of the order of 10^{13} W/cm^2. The photoelectron spectrum was composed by two electron wave packets corresponding to the $2p$ and $2s$ shells, and was a function of the relative delay between the XUV and the IR pulses. The analysis of the delay-dependent spectrogram relied on a reconstruction method that stems from the FROG-CRAB. The reconstruction evidences a delay of about 20 as between the emission of electrons from the $2p$ subshell with respect to the $2s$ subshell, with the $2s$ electrons being emitted first. This work had triggered a bunch of theoretical discussion on the physical origin of the observed time delay. It was believed that such time delay measurements can deliver information about the electronic structure of the target system including electron correlation, and about the electronic dynamics during the photoionization process. However, theoretical investigations to date can only predict time delays half of the measured value or even less[61]. Photoionization time delays between the $3s$ and $3p$ subshells of Ar in the photon energy range between 32 and 42 eV have also been investigated by Klünder *et al.*[62], by using the RABITT technique in which the temporal information is encoded in the phase of sideband oscillations. In this energy range, electronic correlation is expected to play an important role. Therefore to explain the measured results, electron correlation effects were explicitly taken into account by calculating the phase of the single-photon transition matrix element using the random-phase approximation with exchange (RPAE)[63]. Photoemission time delays between different noble gas atoms were also measured, using either APTs[64, 65] or IAPs[66].

Photoemission delay in solids was first observed by Cavalieri *et al.* in 2007[67], where a delay of about 100 as in the emission of photoelectrons from the $4f$ core shell and the

conduction band of single-crystal tungsten was retrieved from attosecond streaking. Later the same approach was applied to single-crystal magnesium[68], showing that the emission from the $2p$ core-level and the valence band occurs simultaneously within the error bar of 20 as. Such measurements provide the possibility of studying the properties of the electronic response and electronic transport during photoionization[69–71], for example, the formation of the Bloch wave packet, its propagation up to the surface-vacuum interface and the electron-electron scattering[72]. The optical-frequency screening effect of the surface and the penetration of the IR field to a single atomic layer was also investigated[73]. In a recent streaking experiment on photoemission from solid magnesium[74], the time delays of collective electron oscillations were investigated. Using an IAP with a central energy of 118 eV, the measured spectrogram consisted of both the band feature of the $2p$ level and the first plasmon-like resonance feature at lower kinetic energies. The measured 60 as delay of the plasmon feature was interpreted in terms of the intrinsic plasmon excitation and extrinsic plasmon excitation. Another measurement took advantage of the RABITT technique and investigated the photoemission time delay on the surfaces of noble metals Ag(111) and Au(111)[75]. The measurement in Ag indicated a strong variation of the photoemission delay as a function of the sideband, while the results for Au showed much weaker variations. It was indicated that the observed time delays cannot be interpreted only in terms of initial state localization and electronic transport, and that other effects such as final state effects might play an important role in the measured time delays. Photoemission time delays from the Cu(100) and Cu(111) surfaces have been investigated theoretically within the RABITT framework[76], which shows that the inclusion of the Fresnel-reflected incident IR pulse at the metal-vacuum interface modifies photoelectron spectra and photoemission time delays in a characteristic way. More discussions on attosecond streaking spectroscopy of atoms and solids can be found in Ref. [77].

1.3.3 probing electron wave packet dynamics in molecules

Attosecond technology paves a way of following and ultimately controlling the photo-induced electron and nuclear dynamics in molecules. The first application of ion momentum imaging with IAPs was reported in 2010, with the measurement of the electron localization in hydrogen molecules after attosecond excitation[78]. Dissociative ionization of D_2/H_2 molecules were induced by a sequence of an IAP and an intense few-cycle IR pulse. The main experimental observation consisted of a measurement of the kinetic energy-resolved asymmetry of the ejection of D^+/H^+ ions left or right along the laser polarization axis. This asymmetry results from two-color dissociative ionization as a function of the XUV-IR time delay. The main observation is that oscillations occur in the asymmetry over a wide range of kinetic energies and a wide range of time delays, including both positive delays (where IR follows the IAP) and the region of time-overlap. The parity breaking of wave function implies electron localization. Such localization is caused by two mechanisms. A first mechanism, which is dominant in the temporal overlapping region, is related to the excitation of autoionizing states of D_2/H_2 followed by decay processes to the ground state $1s\sigma_g$ of D_2^+/H_2^+. The second mechanism is based on the coupling between the $2p\sigma_u$ and $1s\sigma_g$ states of D_2^+/H_2^+ by the IR pulse. Further works conducted with multi-electron diatomic molecules have been reported. Using both APTs and IAPs, the dissociative ionization dynamics of O_2[79, 80] and N_2[81, 82] have been investigated through the XUV-IR pump-probe measurements.

1.3.4 Charge migration in molecules

Sudden ionization of a biologically relevant molecule by an XUV pulse can create a localized hole. Since this state is non-stationary, charges across this molecule will be redistributed by a correlation-driven process. This charge flow, which has been referred to as charge migration, precedes any rearrangement of the nuclear skeleton and it can evolve on a temporal scale ranging from a few femtoseconds down to tens of attoseconds. Such charge dynamics have been theoretically predicted[83] and attracted many experimental groups to observe the

charge migration along the molecular structure. The first experiment in this direction was taken in 2012 on the aromatic amino acid phenylalanine[84], which revealed the presence of a dynamics on a temporal scale of a few tens of femtoseconds triggered by ionization induced by short APTs. A pioneering work performed on the same molecule but with a higher resolution revealed the charge migration in this molecule after XUV photoionization[7]. In this experiment, a 300-as IAP with photon energy between 15 and 35 eV was used to create a sudden hole in the molecule. Therefore numerous excited states of the phenylalanine ion can be produced. A 4-fs waveform controlled near-IR pulse was then used to fragment the ion by strong field dissociative ionization as a function of time delay, resulting in COOH plus the $C_6H_5CH_2CHNH_2^{++}$ dication. Charge migration was evidenced as an oscillatory evolution in the yield of this doubly charged ion fragment. The 4.3 fs oscillation period is shorter than the vibrational response of the molecule. Numerical simulations of the temporal evolution of the electron wave packet created by the XUV pulse provided compelling evidence that the measured oscillations can be related to a periodic charge density oscillation around the amine functional group of this molecule. Moreover, a different kind of experiment based on the electron re-collision and HHG spectroscopy was performed on the HCCI molecule[85], where the hole migration in the HCCI ion after strong field ionization in the IR field was observed.

1.4 Overview of this dissertation

In this thesis, our main focus is to investigate the accuracy of the current method of IAP characterization and of photoionization time delay retrieval from XUV plus IR streaking experiments, and also to propose new methods that can improve the accuracy or extend the range of application. This thesis also includes quantum orbit analysis of HHG using mid-IR driving lasers and therefore the long-wavelength behavior of the HHG yield for different quantum orbits, which is of great importance to generating attosecond pulses in the soft

X-ray region. Moreover, an example of probing ultrafast dynamics of electron correlation in helium atom is given in this thesis as well.

In Chapter 2 we study the HHG process using the quantum orbit theory so that we can separate the contribution of each individual quantum orbit to the HHG spectrum. To be specific, we are interested in the long-wavelength behavior of these quantum orbits. Wavelength scaling laws of the HHG yield at single-atom level corresponding to different quantum orbits are obtained. The macroscopic phase matching of the harmonic field due to different quantum orbits is also studied.

In Chapter 3 we check the accuracy of the FROG-CRAB method in IAP characterization by using the photoelectron spectrograms calculated from both SFA and TDSE as the input data. In Chapter 4 we carry out similar calibrations but for the PROOF method and its improvement swPROOF. These methods are based on second-order perturbation theory for weak IR field instead of the SFA model. These results can be treated as benchmarks of accurate IAP measurement.

In Chapter 5 we take a fresh look at the main method of extracting temporal information from the streaking spectrogram, namely FROG-CRAB. It looks possible to use FROG-CRAB to extract the phase of the transition dipole from which the "photoionization time delay" can be derived. By simulating the streaking spectrograms using SFA or TDSE, We identify the conditions and demonstrate how the FROG-CRAB can be used to retrieve the phase of the transition dipole. Due to the limitation of FROG-CRAB, we also propose a fitting approach to extract the unknown dipole phase of an atom with the help of another well-known reference target.

In Chapter 6 we present a recent experiment where the buildup of the $2s2p$ Fano resonance of helium was observed by using ATAS technique. We have derived an analytical model to interpret the measured delay-dependent photoabsorption spectra. The agreement between theory and experiment confirms that we have observed the dynamics of two-electron correlation in the form of the time-dependent buildup of Fano line shape.

Finally, we summarize this thesis in Chapter 7. Atomic units are used in this dissertation unless otherwise indicated.

Chapter 2

Quantum orbit analysis of HHG with long-wavelength Lasers

The typical photon energy range available from HHG sources with a 800-nm Ti:Sapphire laser has been limited to about 100 eV. The well-known cut-off law $I_p+3.17U_p$ with $U_p \propto I\lambda^2$ suggests that higher energy photons can be produced by the driving lasers with longer wavelengths. Increasing the peak laser intensity is not an option because of the strong depletion as well as the phase mismatch caused by excessive free electrons in the generation medium. With recent development in OPA and OPCPA techniques, mid-IR lasers with a wavelength of a few micrometers are available today, pushing the HHG photon energy range beyond the water window and even to the keV region[30–34, 37, 40, 86]. Wavelength scaling of HHG yield has been studied both theoretically and experimentally. A careful experimental investigation demonstrated that HHG yield at constant laser intensity scales as $\lambda^{-6.3\pm1.1}$ in xenon and $\lambda^{-6.5\pm1.1}$ in krypton over the wavelength range of 800-1850 nm[36]. Early theoretical investigation was mostly based on numerical solution of the time-dependent Schrödinger equation (TDSE)[87–89]. These studies showed that HHG yield at constant driving laser intensity drops as λ^{-x} with $x \approx 5-6$. All these studies were limited to wavelengths below 2 μm and within a fixed photon energy range from 20 to 50 eV. More

recent studies based on the strong field approximation (SFA) showed a scaling behavior with a slightly different x[90–93]. By applying the quantum orbit (QO) theory[94–96], scaling laws for long and short quantum orbits have also been investigated[93, 97–99].

In this chapter we apply the QO theory to separate the contribution of each individual quantum orbit to the HHG spectrum, and therefore to study the long-wavelength behavior of these quantum orbits. Section 2.1.1 gives a derivation of the widely-used SFA or Lewenstein model[16] for HHG, through the S-matrix theory[100]. In Section 2.1.2 we first introduce the saddle-point approximation to the SFA integral and obtain the basic equations for QO theory. The concept of quantum orbit is a counterpart of the classical electron trajectory in the laser field. In the middle of Section 2.1.2 a monochromatic laser field is considered, then we discuss the born time, return time and returning energy which correspond to a particular quantum orbit, within one half optical cycle. We split the quantum orbits into long and short orbits as well as higher-order returns, and calculate the harmonic spectrum given by each orbit separately. The calculations for a few-cycle driving laser are given at the end of Section 2.1.2. In Section 2.2.1 we simplify the saddle-point equations in long-wavelength limit and investigate the behavior of short and long orbits when mid-IR driving wavelengths are applied. In Section 2.2.2 we use the idea of quantitative rescattering theory (QRS)[101] to obtain the returning electron wave packet. We then study the wavelength scaling of the wave packet at a fixed scaled photon energy. At long wavelengths, the wave packets as functions of the scaled energy that belong to a particular quantum orbit are found to have a universal form. Section 2.3 considers the propagation of each individual quantum orbit in the generation medium. We verify that phase matching conditions are different for different quantum orbits. Finally we give a brief summary of this chapter in Section 2.4. The material in this chapter is adapted from the publication [99].

2.1 Theoretical models for HHG

2.1.1 The Lewenstein model or SFA

SFA is a widely used model for atoms or molecules in an intense laser field. The main assumption made in SFA is that the continuum electron dynamics is dominated by the laser field while the core potential is a small perturbation that can be ignored to the lowest order. The majority of strong field effects can be understood at least qualitatively by the SFA model, which is much less computational demanding than solving the TDSE numerically. In this subsection the SFA model describing HHG process is derived using a number of approximations from the TDSE in the length gauge. This model is usually referred to as Lewenstein model[16] that serves as a starting point in many HHG studies.

Consider an atom (or an ion) in a single-active-electron (SAE) approximation under the influence of an intense laser field $\mathbf{E}(t)$, the Schrödinger equation in the length gauge takes the form

$$i\frac{\partial}{\partial t}|\Psi(\mathbf{r},t)\rangle = \left(-\frac{1}{2}\nabla^2 + V(\mathbf{r}) + \mathbf{r}\cdot\mathbf{E}(t)\right)|\Psi(\mathbf{r},t)\rangle, \tag{2.1}$$

where $V(\mathbf{r})$ is the potential due to the ionic core.

The total Hamiltonian can be decomposed as

$$H(t) = H_0 + \mathbf{r}\cdot\mathbf{E}(t). \tag{2.2}$$

The field free Hamiltonian

$$H_0 = -\frac{1}{2}\nabla^2 + V(\mathbf{r}) \tag{2.3}$$

determines the ground state $|g\rangle$ and the excited bound states $\{|e\rangle\}$ of this system

$$H_0|g\rangle = -I_p|g\rangle, \tag{2.4}$$

$$H_0|e\rangle = E_e|e\rangle, \tag{2.5}$$

where I_p is the ionization energy.

The electron in the continuum can also be described by the eigenstates of H_0

$$H_0|\mathbf{k}\rangle = \frac{k^2}{2}|\mathbf{k}\rangle, \tag{2.6}$$

where $\mathbf{k}$ is the kinetic momentum of the outgoing electron. $|g\rangle$, $\{|e\rangle\}$ and $\{|\mathbf{k}\rangle\}$ form a complete basis set of the whole Hilbert space.

Consider the case that the field intensity is large enough so that the Keldysh parameter $\gamma = \sqrt{I_p/2U_p} \lesssim 1$, with $U_p = \frac{E_0^2}{4\omega_L^2}$ being the ponderomotive energy. By assuming that the electron in the ground state is tunnel ionized into continuum directly without intermediate resonances, then all the excited bound states can be ignored. Furthermore, consider the situation of weak ionization, which requires the intensity be much smaller than the saturation intensity. In this situation only a small fraction of the targets are ionized during the interaction time so that the depletion of the ground state can be neglected. Within the above assumptions the wavefunction can be expanded as

$$|\Psi(t)\rangle = e^{iI_p t}\left\{|g\rangle + \int d^3k\, b(\mathbf{k},t)|\mathbf{k}\rangle\right\}. \tag{2.7}$$

The HHG spectrum with polarization along a direction $\mathbf{e_i}$ can be calculated from the time-dependent induced dipole moment

$$D_i(t) = \mathbf{e_i}\cdot\mathbf{D}(t) = \mathbf{e_i}\cdot\langle\Psi(t)|\mathbf{r}|\Psi(t)\rangle \tag{2.8}$$

from its Fourier components as

$$P(\omega) \propto \omega^4|D_i(\omega)|^2. \tag{2.9}$$

Consider the transitions between continuum state and ground state which contribute to the harmonics while dropping the higher order continuum-continuum part, the induced

dipole can be written as

$$\mathbf{D}(t) = \int d^3k \, \langle g|\mathbf{r}|\mathbf{k}\rangle b(\mathbf{k},t) + c.c.. \tag{2.10}$$

Next we use the Keldysh theory (or the KFR model)[13, 102, 103] in the length gauge[104] to evaluate the induced dipole moment. The KFR model (or its generalization in the form of the S-matrix theory[100]), was initially derived for strong field above-threshold ionization[13, 102–105]. The approach to HHG process here is equivalent to the original derivation given by Lewenstein[16].

We introduce the time evolution operator $U(t,t')$ for the total Hamiltonian $H(t)$ such that

$$|\Psi(t)\rangle = U(t,-\infty)|\Psi(-\infty)\rangle = U(t,-\infty)|g\rangle, \tag{2.11}$$

and the time evolution operator $U_0(t,t')$ for the field-free Hamiltonian H_0 such that

$$U_0(t,-\infty)|g\rangle = e^{iI_p t}|g\rangle. \tag{2.12}$$

From Eq. (2.7), $b(\mathbf{k},t)$ can be solved as

$$b(\mathbf{k},t) = e^{-iI_p t}\langle \mathbf{k}|U(t,-\infty)|g\rangle. \tag{2.13}$$

By substituting Eq. (2.13) into Eq. (2.10) we obtain

$$\begin{aligned} \mathbf{D}(t) &= \int d^3k \, e^{-iI_p t}\langle g|\mathbf{r}|\mathbf{k}\rangle\langle \mathbf{k}|U(t,-\infty)|g\rangle + c.c. \\ &= e^{-iI_p t}\langle g|\mathbf{r}U(t,-\infty)|g\rangle + c.c.. \end{aligned} \tag{2.14}$$

Based on the S-matrix theory[103, 104], the above equation can be rewritten as

$$\begin{aligned}\mathbf{D}(t) &= e^{-iI_p t}\left\{-i\int_{-\infty}^{t} dt'\langle g|\mathbf{r}U(t,t')\mathbf{r}\cdot\mathbf{E}(t')U_0(t',-\infty)|g\rangle\right\}+c.c. \\ &= -i\int_{-\infty}^{t} dt' e^{-iI_p t}\langle g|\mathbf{r}U(t,t')\mathbf{r}\cdot\mathbf{E}(t')e^{iI_p t'}|g\rangle+c.c.. \end{aligned} \tag{2.15}$$

The total Hamiltonian can also be decomposed as

$$H(t) = H_F(t) + V(\mathbf{r}). \tag{2.16}$$

$H_F(t)$ is the Hamiltonian of a free electron in the laser field

$$H_F(t) = -\frac{1}{2}\nabla^2 + \mathbf{r}\cdot\mathbf{E}(t), \tag{2.17}$$

whose eigenstates are the Volkov states (in the length gauge)

$$|\chi_{\mathbf{p}}(t)\rangle = |\mathbf{p}+\mathbf{A}(t)\rangle e^{-i\int_{-\infty}^{t} dt''\frac{1}{2}[\mathbf{p}+\mathbf{A}(t'')]^2}. \tag{2.18}$$

Here $|\mathbf{p}\rangle$ denotes the plane wave state

$$\langle\mathbf{r}|\mathbf{p}\rangle = \frac{1}{(2\pi)^{3/2}}e^{i\mathbf{p}\cdot\mathbf{r}}, \tag{2.19}$$

and $\mathbf{A}(t)$ is the vector potential of the laser field

$$\mathbf{A}(t) = -\int_{-\infty}^{t} dt'\mathbf{E}(t'). \tag{2.20}$$

The time evolution operator corresponding to $H_F(t)$ can be constructed by Volkov states

$$U_F(t,t') = \int d^3p|\chi_{\mathbf{p}}(t)\rangle\langle\chi_{\mathbf{p}}(t')|. \tag{2.21}$$

The operator $U(t,t')$ satisfies the Dyson equation

$$U(t,t') = U_F(t,t') - i\int_{t'}^{t} dt'' U_F(t,t'')VU(t'',t'). \tag{2.22}$$

In the strong field regime, the electron-core potential $V(\mathbf{r})$ can be treated as a small perturbation for the electron in the continuum. In the lowest order approximation, Eq. (2.22) is

$$U(t,t') = U_F(t,t'). \tag{2.23}$$

In essence, within the above approximation, the electron in the continuum is treated as a free particle moving in the strong laser field. Equation (2.15) is then reduced to

$$\begin{aligned}
\mathbf{D}(t) &= -i\int_{-\infty}^{t} dt' e^{-iI_p t}\langle g|\mathbf{r}U_F(t,t')\mathbf{r}\cdot\mathbf{E}(t')e^{iI_p t'}|g\rangle + c.c. \\
&= -i\int_{-\infty}^{t} dt' \int d^3p\, e^{-iI_p t}\langle g|\mathbf{r}|\chi_{\mathbf{p}}(t)\rangle\langle\chi_{\mathbf{p}}(t')|\mathbf{r}\cdot\mathbf{E}(t')e^{iI_p t'}|g\rangle + c.c. \\
&= -i\int_{-\infty}^{t} dt' \int d^3p\, e^{-iI_p t}\langle g|\mathbf{r}|\mathbf{p}+\mathbf{A}(t)\rangle\mathbf{E}(t')\cdot\langle\mathbf{p}+\mathbf{A}(t')|\mathbf{r}|g\rangle e^{iI_p t'}e^{-i\int_{t'}^{t} dt''\frac{1}{2}[\mathbf{p}+\mathbf{A}(t'')]^2} + c.c. \qquad (2.24) \\
&= -i\int_{-\infty}^{t} dt' \int d^3p\, \mathbf{d}^*(\mathbf{p}+\mathbf{A}(t))\mathbf{E}(t')\cdot\mathbf{d}(\mathbf{p}+\mathbf{A}(t'))e^{-iS(\mathbf{p},t,t')} + c.c.. \qquad (2.25)
\end{aligned}$$

In Eq. (2.25), $\mathbf{d}(\mathbf{p}) = \langle\mathbf{p}|\mathbf{r}|g\rangle$ is the dipole matrix element for the bound-free transition where $|\mathbf{p}\rangle$ denotes the plane wave state, and the phase factor

$$S(\mathbf{p},t,t') = \int_{t'}^{t} dt'' \frac{1}{2}[\mathbf{p}+\mathbf{A}(t'')]^2 + I_p(t-t') = \int_{t'}^{t} dt'' \left(\frac{1}{2}[\mathbf{p}+\mathbf{A}(t'')]^2 + I_p\right). \tag{2.26}$$

The integral in Eq. (2.24) has a simple and intuitive interpretation which corresponds to the quasi-classical three step model[15, 16]: $\mathbf{p}$ can be treated as the classical canonical momentum, since the electron-ion interaction is neglected for the continuum electron, $\mathbf{p}$ turns into a conserved quantity; $\mathbf{p}+\mathbf{A}(t)$ can be assumed as the instantaneous velocity at

time t; the factor $\mathbf{E}(t') \cdot \langle \mathbf{p} + \mathbf{A}(t')|\mathbf{r}|g\rangle e^{iI_p t'}$ describes the ionization process which occurs at time t' while $e^{-iI_p t}\langle g|\mathbf{r}|\mathbf{p} + \mathbf{A}(t)\rangle$ determines the amplitude of photo-recombination at time t; the factor $e^{-i\int_{t'}^{t} dt'' \frac{1}{2}[\mathbf{p}+\mathbf{A}(t'')]^2}$ is the phase accumulated from t' to t while the electron propagating in the continuum; at a given recombination (or photon emission) time t the induced dipole is obtained by integrating over the contributions from all ionization time $t' < t$ and all canonical momentum $\mathbf{p}$. The factor $S(\mathbf{p}, t, t')$ in Eq. (2.25) is often referred to as the quasi-classical action but it also incorporates some effects of the ionization and recombination process through its dependence on I_p, see Eq. (2.26). The complex conjugate part in the dipole moment is the time reversal of the above three-step process which is a pure quantum contribution and has no classical interpretation.

In practice the SFA form of Eq. (2.25) is rarely used. Instead, a simpler form, based on the saddle point approximation for the integral over 3D momentum $\mathbf{p}$ in Eq. (2.25), has been used more often. Mathematically, one can apply the saddle-point approximation to a n-dimensional integral as the following

$$\int d^n\omega \; E(\omega)e^{if(\omega)} \approx \sum_s \sqrt{\frac{(2\pi i)^n}{\det(f''(\omega_s))}} E(\omega_s)e^{if(\omega_s)}. \tag{2.27}$$

In Eq. (2.27) the saddle point ω_s is determined by the saddle point equation

$$\nabla_\omega f(\omega_s) = 0, \tag{2.28}$$

and $f''(\omega_s) = \nabla_\omega \nabla_\omega f(\omega_s)$ is the $n \times n$ Hessian matrix at the saddle point ω_s.

Now the saddle point equations for $\mathbf{p}$ in Eq. (2.25) can be written in a vector form as

$$\begin{aligned} &\nabla_{\mathbf{p}} S(\mathbf{p}, t, t') = \nabla_{\mathbf{p}} \int_{t'}^{t} dt'' \left(\frac{1}{2}[\mathbf{p} + \mathbf{A}(t'')]^2 + I_p \right) \\ &= \int_{t'}^{t} dt'' \nabla_{\mathbf{p}}[\mathbf{p} + \mathbf{A}(t'')] \cdot [\mathbf{p} + \mathbf{A}(t'')] = \int_{t'}^{t} [\mathbf{p} + \mathbf{A}(t'')] dt'' = 0, \end{aligned} \tag{2.29}$$

which gives the saddle point solution $\mathbf{p}_s$ as

$$\mathbf{p}_s = -\frac{1}{t-t'}\int_{t'}^{t} \mathbf{A}(t'')dt''. \tag{2.30}$$

Since $\nabla_{\mathbf{p}} S(\mathbf{p},t,t') = \int_{t'}^{t} \mathbf{v}(t'')dt'' = \mathbf{r}(t) - \mathbf{r}(t')$, the semi-classical interpretation of Eq. (2.29) is clear: the dominant contribution to the HHG photon emission comes from the trajectory with canonical momentum $\mathbf{p}_s$ such that the electron born at time t' returns to the same position at time t.

The Hessian matrix of $S(\mathbf{p},t,t')$ is given by

$$\nabla_{\mathbf{p}}\nabla_{\mathbf{p}} S(\mathbf{p},t,t') = \int_{t'}^{t} \nabla_{\mathbf{p}}[\mathbf{p}+\mathbf{A}(t'')]dt'' = (t-t')\mathbf{I}, \tag{2.31}$$

where $\mathbf{I}$ is the 3×3 unit matrix.

By using Eq. (2.27) the saddle-point approximation of Eq. (2.25) can be written as

$$\begin{aligned}
\mathbf{D}(t) &= -i\int_{-\infty}^{t} dt' \sqrt{\frac{(2\pi i)^3}{\det(-(t-t')\mathbf{I})}}\mathbf{d}^*(\mathbf{p}_s+\mathbf{A}(t))\mathbf{E}(t')\cdot\mathbf{d}(\mathbf{p}_s+\mathbf{A}(t'))e^{-iS(\mathbf{p}_s,t,t')} + c.c. \\
&= -i\int_{-\infty}^{t} dt' \left(\frac{-2\pi i}{t-t'-i\epsilon}\right)^{3/2} \mathbf{d}^*(\mathbf{p}_s+\mathbf{A}(t))\mathbf{E}(t')\cdot\mathbf{d}(\mathbf{p}_s+\mathbf{A}(t'))e^{-iS(\mathbf{p}_s,t,t')} + c.c..
\end{aligned} \tag{2.32}$$

Here ϵ is an arbitrary small positive regularization constant introduced to smooth out the singularity. The saddle-point approximation for the integral over $\mathbf{p}$ yields a factor $(t-t')^{-3/2}$ which accounts for the quantum diffusion effect, i.e., the spread of the wave packet of the continuum electron. Larger excursion time in the continuum will have less contribution to the harmonic emission.

Consider the case that the electric field is linearly polarized along the x-axis. Equation (2.30) shows that $\mathbf{p}_s$ is also along the x-axis. Equation (2.32) for the induced dipole

moment $D_x(t)$ along the x-axis reduces to a one-dimensional equation

$$D_x(t) = -i\int_{-\infty}^{t} dt' \left(\frac{-2\pi i}{t-t'-i\epsilon}\right)^{3/2} d_x^*(p_s+A(t))d_x(p_s+A(t'))E(t')e^{-iS(p_s,t,t')} + c.c., \tag{2.33}$$

in which $d_x(p) = \langle p\mathbf{e}_x|x|g\rangle$ is the x component of the dipole transition matrix element from the ground state to the plane wave state propagating along x axis with momentum p.

Equations (2.25), (2.32) and (2.33) are the standard equations in the SFA (or the Lewenstein model) for the laser induced dipole moment. To account for the ground state depletion a damping factor $a(t)$ is introduced[16]. This factor is often calculated by using the Ammosov-Delone-Krainov (ADK) theory[101, 106].

2.1.2 The quantum orbit theory

Formulation and basic equations

Equation (2.33) shows the time dependent dipole moment induced by the laser field. The HHG power spectrum is given by

$$P(\omega) \propto \omega^4 |D_x(\omega)|^2, \tag{2.34}$$

in which ω is the harmonic photon energy. $D_x(\omega)$ is the Fourier transform of $D_x(t)$

$$D_x(\omega) = \int_{-\infty}^{\infty} D_x(t)e^{i\omega t}dt = \int_{-\infty}^{\infty} \left[D_x^{(+)}(t) + c.c.\right] e^{i\omega t}dt = D_x^{(+)}(\omega) + \left[D_x^{(+)}(-\omega)\right]^*, \tag{2.35}$$

where

$$D_x^{(+)}(\omega) = -i\int_{-\infty}^{\infty} dt \int_{-\infty}^{t} dt' \left(\frac{-2\pi i}{t-t'-i\epsilon}\right)^{3/2} d_x^*(p_s+A(t))d_x(p_s+A(t'))E(t')e^{-i\Theta(p_s,t,t')}. \tag{2.36}$$

In the above equation

$$\Theta(p_s, t, t') = S(p_s, t, t') - \omega t, \tag{2.37}$$

$$S(p_s, t, t') = \int_{t'}^{t} dt'' \left(\frac{1}{2}[p_s + A(t'')]^2 + I_p \right), \tag{2.38}$$

and

$$p_s = -\frac{1}{t - t'} \int_{t'}^{t} A(t'')dt''. \tag{2.39}$$

The basic idea of the QO theory is to further apply the saddle-point approximation to the two-dimensional integral Eq. (2.36) over t and t'[16, 96]. Saddle point equations for t and t' reads

$$\begin{aligned} &\frac{\partial \Theta}{\partial t'} = \frac{\partial S}{\partial t'} = -\frac{1}{2}[p_s + A(t')]^2 - I_p = 0 \\ &\Rightarrow \frac{1}{2}[p_s + A(t')]^2 = -I_p, \end{aligned} \tag{2.40}$$

$$\begin{aligned} &\frac{\partial \Theta}{\partial t} = \frac{\partial S}{\partial t} - \omega = \frac{1}{2}[p_s + A(t)]^2 + I_p - \omega = 0 \\ &\Rightarrow \frac{1}{2}[p_s + A(t)]^2 = \omega - I_p. \end{aligned} \tag{2.41}$$

Equation (2.40) implies that when the electron is born to the continuum, the "kinetic energy" is a negative value $-I_p$, which accounts for the quantum effect of tunneling ionization. Equation (2.41) describes energy conservation when the electron recombines with the ionic core. Upon recombination the electron returns to the ground state and emits a photon with energy ω. For a given ω one can solve Eqs. (2.40) and (2.41) [with p_s given in Eq. (2.39)] simultaneously to find a series of saddle points (t'_s, t_s). Due to the constraint imposed by Eq. (2.40) both the solutions t'_s and t_s are complex-valued. Each solution (t'_s, t_s) determines a unique "quantum orbit" which can be viewed as an extension of the classical orbit of an electron moving in the electric field[95, 96]. The saddle-point approximation of

Eq. (2.36) reads

$$D_x^{(+)}(\omega) = -i\sum_s \sqrt{\frac{(2\pi i)^2}{\det(\Theta'')}}\left(\frac{-2\pi i}{t_s - t'_s}\right)^{3/2} d_x^*(p_s + A(t_s))d_x(p_s + A(t'_s))E(t'_s)e^{-i\Theta(p_s,t_s,t'_s)}. \tag{2.42}$$

In the spirit of Feynman's path integrals[94], $D_x^{(+)}(\omega)$ is a superposition of the contribution from individual quantum orbit weighted by $e^{-i\Theta(p_s,t_s,t'_s)}$. The quantum orbit that corresponds to negative ω does not have any classical counterpart and will have little contribution. For this reason in a typical quantum orbits calculation, the second term on the right hand side of Eq. (2.35) is dropped, i.e.

$$D_x(\omega) \approx D_x^{(+)}(\omega) = \sum_s D_{xs}(\omega), \tag{2.43}$$

where $D_{xs}(\omega)$ denotes the induced dipole moment by an individual quantum orbit

$$D_{xs}(\omega) = \frac{2\pi}{\sqrt{\det(S'')}}\left(\frac{-2\pi i}{t_s - t'_s}\right)^{3/2} d_x^*(p_s + A(t_s))d_x(p_s + A(t'_s))E(t'_s)e^{-i\Theta(p_s,t_s,t'_s)}. \tag{2.44}$$

Here the 2×2 Hessian matrix S'' is given as

$$S'' = \left(\begin{array}{cc} \frac{\partial^2 S(p_s,t,t')}{\partial t^2} & \frac{\partial^2 S(p_s,t,t')}{\partial t \partial t'} \\ \frac{\partial^2 S(p_s,t,t')}{\partial t' \partial t} & \frac{\partial^2 S(p_s,t,t')}{\partial t'^2} \end{array}\right)_{t=t_s,t'=t'_s}. \tag{2.45}$$

From Eqs. (2.38) and (2.39) one can obtain

$$\left.\frac{\partial^2 S}{\partial t^2}\right|_{t_s,t'_s} = -\frac{[p_s + A(t_s)]^2}{t_s - t'_s} - E(t_s)[p_s + A(t_s)], \tag{2.46}$$

$$\left.\frac{\partial^2 S}{\partial t'^2}\right|_{t_s,t'_s} = -\frac{[p_s + A(t'_s)]^2}{t_s - t'_s} + E(t'_s)[p_s + A(t'_s)], \tag{2.47}$$

$$\left.\frac{\partial^2 S}{\partial t \partial t'}\right|_{t_s,t'_s} = \left.\frac{\partial^2 S}{\partial t' \partial t}\right|_{t_s,t'_s} = \frac{[p_s + A(t_s)][p_s + A(t'_s)]}{t_s - t'_s}. \tag{2.48}$$

In Eq. (2.43) only the quantum orbits leading to negative $\mathrm{Im}\{\Theta\}$ are included in order to obtain converged results.

QO theory of HHG by monochromatic laser fields

In this subsection we consider harmonic emission by a monochromatic laser field within the QO theory where the laser-induced dipole can be calculated analytically. The laser field is given by $E(t) = E_0 \cos(\omega_L t)$. Here ω_L is the frequency of the driving laser, and the optical period is $T_L = 2\pi/\omega_L$. Due to the periodicity and symmetry the HHG spectrum induced by such a monochromatic laser field contains only odd harmonics of the fundamental frequency ω_L. The intensity of these harmonics is fully determined by the induced dipole moment within half optical cycle. Therefore in the following discussion we focus mainly on the sub-cycle dynamics. In the quantum orbits analysis only the orbit that has a ionization time (often called born time) within the half optical cycle, $(-T_L/4, T_L/4)$, has to be considered.

For a monochromatic electric field,

$$A(t) = -\int E_0 \cos(\omega_L t')dt' = -\frac{E_0}{\omega_L}\sin(\omega_L t), \tag{2.49}$$

and

$$p_s = -\frac{1}{t - t'}\int_{t'}^{t} A(t'')dt'' = -\frac{E_0}{\omega_L}\left(\frac{\cos(\omega_L t) - \cos(\omega_L t')}{\omega_L t - \omega_L t'}\right). \tag{2.50}$$

The saddle point equations (2.40) and (2.41) now become

$$\left(\frac{E_0}{\omega_L}\right)^2 \left(\frac{\cos(\omega_L t) - \cos(\omega_L t')}{\omega_L t - \omega_L t'} + \sin(\omega_L t')\right)^2 = -2I_p, \tag{2.51}$$

$$\left(\frac{E_0}{\omega_L}\right)^2 \left(\frac{\cos(\omega_L t) - \cos(\omega_L t')}{\omega_L t - \omega_L t'} + \sin(\omega_L t)\right)^2 = 2(\omega - I_p). \tag{2.52}$$

By introducing the ponderomotive energy $U_p = \frac{E_0^2}{4\omega_L^2}$, the equations above can be rewritten as

$$\left(\frac{\cos\theta - \cos\theta'}{\theta - \theta'} + \sin\theta'\right)^2 = -\frac{I_p}{2U_p} = -\gamma^2, \tag{2.53}$$

$$\left(\frac{\cos\theta - \cos\theta'}{\theta - \theta'} + \sin\theta\right)^2 = \frac{(\omega - I_p)}{2U_p} = \frac{\tilde{\omega}}{2}, \tag{2.54}$$

where $\theta' = \omega_L t'$, $\theta = \omega_L t$ are the born and return time scaled by the optical period, $\gamma = \sqrt{\frac{I_p}{2U_p}}$ is the Keldysh parameter and $\tilde{\omega} = \frac{\omega - I_p}{U_p}$ can be interpreted as the kinetic energy of the returning electron scaled by the ponderomotive energy. By including the quantum origin of the tunneling process, the solutions θ_s' and θ_s are all complex values.

The simple classical model assumes the electron is born with zero kinetic energy, which is equivalent to $\gamma = 0$. Then Eqs. (2.53) and (2.54) reduce into

$$(\cos\theta_c - \cos\theta_c') + (\theta_c - \theta_c')\sin\theta_c' = 0, \tag{2.55}$$

$$2(\sin\theta_c - \sin\theta_c')^2 = \tilde{\omega}. \tag{2.56}$$

In this classical picture θ_c' and θ_c are all real quantities. We can expect that real parts of quantum orbit solutions $\mathrm{Re}\{\theta_s'\}$ and $\mathrm{Re}\{\theta_s\}$ are counterparts of the classical born and return time and will approach them as $\gamma \to 0$.

In the classical picture, as shown in Fig. 2.1 and Fig. 2.2, the electron born before the peak field ($-90° < \theta' < 0°$) will not return to the core. The electron born after the peak field ($0° \leq \theta' < 90°$) has a chance to revisit the core with kinetic energy $\tilde{\omega}U_p$. Moreover, the electron born in the region $0° \leq \theta' < 12°$ may revisit its core more than once, which is often named higher order returns. The recombination time for the first return roughly lies in $110° \leq \theta < 360°$, for the second return $360° \leq \theta < 540°$, for the third return $540° \leq \theta < 720°$. Each return has its maximum return energy (cutoff) such as $\tilde{\omega} = 3.2$ for

the first return ($\theta' = 17°$ correspondingly), $\tilde{\omega} = 1.5$ for the second, $\tilde{\omega} = 2.4$ for the third. The overall cutoff of the HHG is dominated by the first return, i.e. $\omega_{\text{cutoff}} \approx 3.2U_p + I_p$. In each return the orbit that has a particular return energy $\tilde{\omega}$ below cutoff splits into two branches: the orbit which returns earlier is named "short" orbit while that returns later is named "long" orbit. For odd-number returns (the first, third, fifth ...) the electron born earlier will follow the long orbit, however for even-number returns (the second, fourth, ...) the electron born earlier will follow the short orbit. In our discussion the label 'S1' refers to the short orbit in the first return, 'L1' refers to the long orbit in the first return and so forth.

Figures 2.1 and 2.2 show that the quantum orbit solutions $\text{Re}\{\theta'_s\}$ and $\text{Re}\{\theta_s\}$ (at $\gamma = 0.94$) in general agree with the classical quantities θ'_c and θ_c. However our example also illustrates some discrepancies between them. The time interval of ionization given by the QO is always narrower than the classical prediction, in particular, the born interval of the S1 orbit is reduced to $17° < \theta' < 35°$. Compared to the classical result, the cutoff of the first return is extended to $\tilde{\omega} = 3.8$ due to quantum tunneling and diffusion[16, 96], and the cutoff of the third return is also increased, while the cutoff of the second return is decreased.

The imaginary part of the born time $\text{Im}\{\theta'_s\}$ is a direct consequence of the quantum tunneling. As we shall discuss in Section 2.2.1, $\text{Im}\{t'_s\}$ may be interpreted as the time required for the electron to tunnel through the barrier[107]. This tunneling time mainly depends on I_p and the field strength when the electron is born. As Fig. 2.3(a) shows, $\text{Im}\{\theta'_s\}$ for all orbits except S1 are very close to each other, because these orbits are all born in a narrow time interval right after the peak field so that the electric field at their born time are almost the same. On the contrary the S1 orbit is born later so that the corresponding electric field is much weaker, which leads to a longer tunneling time. Figure 2.3(b) shows that the imaginary part of the return time $\text{Im}\{\theta_s\}$ is close to zero for all orbits except S1. In other words, for the orbits with long excursion time the recombination is well separated from tunneling so θ_s is dominated by the real classical recombination time. On the contrary,

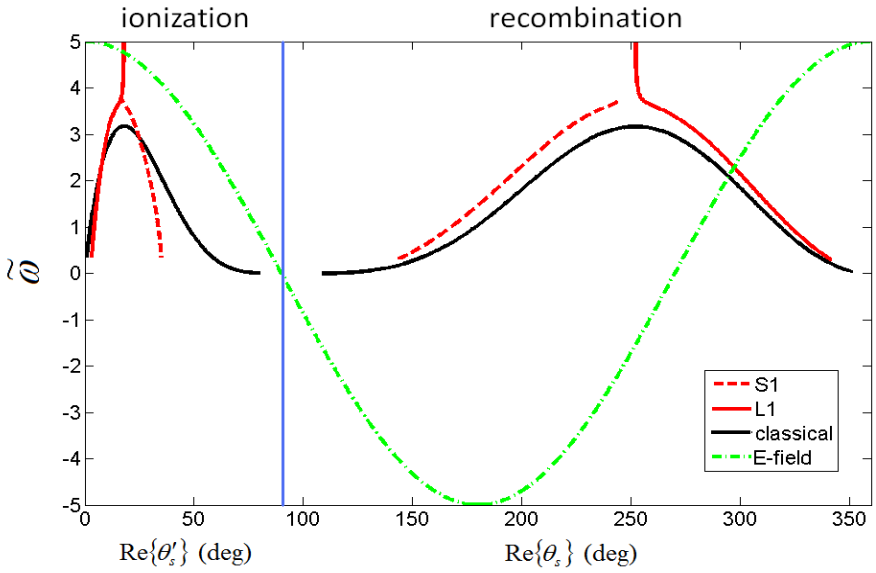

Figure 2.1: *Red line: the real part of ionization time and recombination time for S1 (dashed) and L1 (solid) as functions of* $\tilde{\omega}$*, obtained from Eqs. (2.53) and (2.54) with parameters: 800 nm wavelength,* 1.5×10^{14} *W/cm*^{2} *peak intensity, argon target (*$\gamma = 0.94$*). Solid black line: classical born and return time calculated from Eqs. (2.55) and (2.56). Dot-dashed green line: profile of the electric field.*

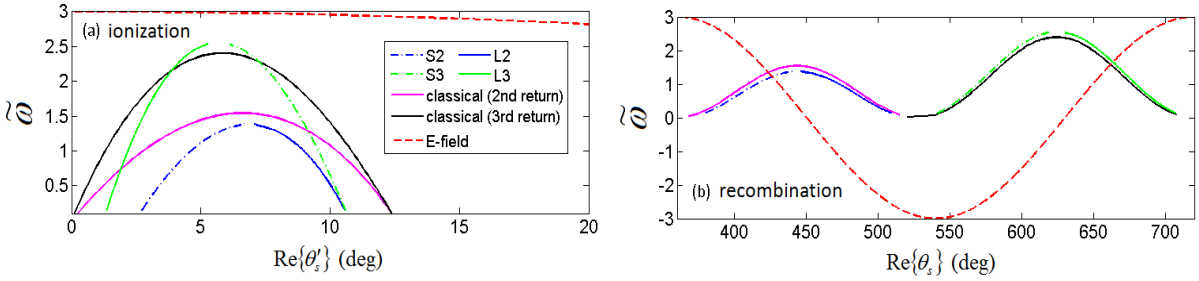

Figure 2.2: *The real part of (a) ionization time and (b) recombination time for higher order returns as functions of* $\tilde{\omega}$ *calculated from both quantum orbits and classical equations. The parameters are the same as in Fig. 2.1.*

for the S1 orbit, especially at low energies $\tilde{\omega} \leq 2$, the excursion time is relatively small so that the recombination feels the influence of the quantum nature of the tunneling ionization, which gives rise to the nonzero imaginary return time.

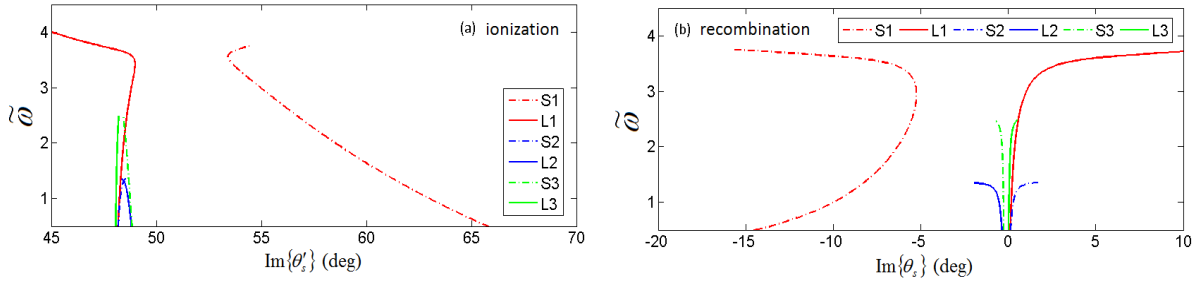

Figure 2.3: *(a)* $\mathrm{Im}\{\theta_s'\}$ *and (b)* $\mathrm{Im}\{\theta_s\}$ *for quantum orbits up to the third return as functions of* $\tilde{\omega}$ *calculated from Eqs. (2.53) and (2.54). The parameters are the same as in Fig. 2.1.*

From Eqs. (2.37) and (2.38) the factor Θ corresponding to the saddle point solution (t_s', t_s) can be derived as follows:

$$
\begin{aligned}
\Theta_s &= \int_{t_s'}^{t_s} dt'' \left(\frac{1}{2}[p_s + A(t'')]^2 + I_p \right) - \omega t_s \\
&= I_p(t_s - t_s') + \frac{1}{2}p_s^2(t_s - t_s') + p_s \int_{t_s'}^{t_s} A(t'')dt'' + \frac{E_0^2}{2\omega_L^2} \int_{t_s'}^{t_s} \sin^2(\omega_L t'')dt'' - \omega t_s \\
&= I_p(t_s - t_s') - \frac{E_0^2}{2\omega_L^2} \left(\frac{\cos(\omega_L t_s) - \cos(\omega_L t_s')}{\omega_L t_s - \omega_L t_s'} \right)^2 (t_s - t_s') \\
&+ \frac{E_0^2}{4\omega_L^2} \left[(t_s - t_s') - \frac{\sin 2\omega_L t_s - \sin 2\omega_L t_s'}{2\omega_L} \right] - \omega t_s \\
&= \left[\frac{I_p}{\omega_L} - \frac{E_0^2}{2\omega_L^3} \left(\frac{\cos\theta_s - \cos\theta_s'}{\theta_s - \theta_s'} \right)^2 + \frac{E_0^2}{4\omega_L^3} \right] (\theta_s - \theta_s') - \frac{E_0^2}{8\omega_L^3}(\sin 2\theta_s - \sin 2\theta_s') - \frac{\omega}{\omega_L}\theta_s \\
&= \frac{2U_p}{\omega_L} \left\{ \left[\gamma^2 + \frac{1}{2} - \left(\frac{\cos\theta_s - \cos\theta_s'}{\theta_s - \theta_s'} \right)^2 \right] (\theta_s - \theta_s') - \frac{1}{4}(\sin 2\theta_s - \sin 2\theta_s') - \left(\frac{\tilde{\omega}}{2} + \gamma^2 \right) \theta_s \right\}.
\end{aligned}
\tag{2.57}
$$

Since θ_s', θ_s are complex, Θ_s is also a complex quantity. The real part $\mathrm{Re}\{\Theta_s\} = \mathrm{Re}\{S_s\} -$

$\omega \mathrm{Re}\{t_s\}$, in which $\mathrm{Re}\{S_s\}$ is the phase accumulated during the electron excursion in the continuum. As Fig. 2.4(a) shows, larger excursion time leads to larger phase accumulated. From Fig. 2.4(b), the imaginary part $\mathrm{Im}\{\Theta_s\}$ is always negative, which will result in a damping factor $e^{\mathrm{Im}\{\Theta_s\}}$ in the induced dipole Eq. (2.44) and thus a factor $e^{2\mathrm{Im}\{\Theta_s\}}$ to the HHG yield. This exponential factor is very critical to the HHG yield and it is related to the tunneling ionization rate[97]. We shall discuss this point further in Section 2.2.1. This ionization rate depends sensitively on the strength of the electric field when the electron is born. Since the field strength at born time does not significantly change for L1 and all higher order returns, $\mathrm{Im}\{\Theta_s\}$ for those orbits are almost on top of each other and independent of $\tilde{\omega}$. On the other hand, the S1 orbit is born in a weaker field so that its $\mathrm{Im}\{\Theta_s\}$ value is well below others'. For S1 orbit, as $\tilde{\omega}$ grows the field strength at born time will have a considerable increase [see Fig. 2.1] and $\mathrm{Im}\{\Theta_s\}$ will also increase.

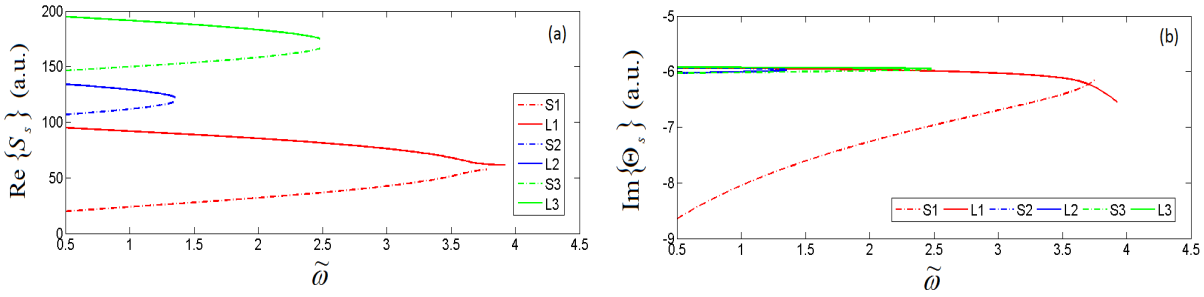

Figure 2.4: *(a)* $\mathrm{Re}\{S_s\}$ *and (b)* $\mathrm{Im}\{\Theta_s\}$ *for quantum orbits up to the third return as functions of* $\tilde{\omega}$ *calculated from Eq. (2.57). The parameters are the same as in Fig. 2.1.*

To evaluate $D_{xs}(\omega)$ one needs to know the bound-free transition dipole matrix element $d_x(p) = \langle p\mathbf{e}_x|x|g\rangle$. In our quantum orbit analysis the ground state is approximated by a Gaussian form[16]

$$\langle \mathbf{r}|g\rangle = \left(\frac{a}{\pi}\right)^{3/4} e^{-ar^2/2}. \tag{2.58}$$

So $d_x(p)$ has a simple analytical expression

$$d_x(p) = i\left(\frac{1}{\pi a}\right)^{3/4} \frac{p}{a} e^{-p^2/2a}, \tag{2.59}$$

with $a = 0.8I_p$. This Gaussian form is convenient since the transition dipole does not have any singularity in the complex plane which could lead to unnecessary complications.

Figure 2.5(a) plots the contribution $|D_{xs}(\omega)|^2$ from each quantum orbit driven by an 800 nm laser. There are two main factors that determine the HHG yield: the ionization rate given by $e^{2\mathrm{Im}\{\Theta_s\}}$ and the quantum diffusion described by $|t_s - t_s'|^{-3}$. The S1 orbit has the least excursion time and thus the least quantum diffusion, however its ionization rate is considerably smaller. The quantum orbit method shows the latter will dominate so that S1 is weaker than L1. In the lower plateau region S1 may be comparable or even weaker than some of the higher order returns. For the orbits other than S1, since their ionization rates are comparable the dominant factor will be diffusion. Therefore HHG yield drops as the excursion time grows. For example, in the energy range that all returns up to the third contribute, L1>S2>L2>S3>L3, as expected. At the cutoff of each return the short and long orbits merge together and the saddle-point approximation produces a spike. Beyond the cutoff the contribution from the short orbit diverges so it must be discarded. Such unphysical divergence can be removed by including the third order derivative term in the Taylor expansion of S[93] and applying the uniform approximation[95]. We remark that the SFA based quantum orbit method tends to underestimate the contribution from S1 as compared to the TDSE simulation[108, 109]. Figure 2.5(b) shows the HHG spectrum as the coherent superposition of various quantum orbits. S1+L1 has a relatively simple oscillating profile since only two orbits are involved. After including higher order returns the spectrum has a more complicated structure, which indicates considerable contribution from higher order returns to the lower plateau. Therefore at single atom level the effect from higher order returns cannot be neglected. However as we consider the macroscopic propagation

effect this situation may be changed due to the phase matching of each orbit, see Section 2.3.

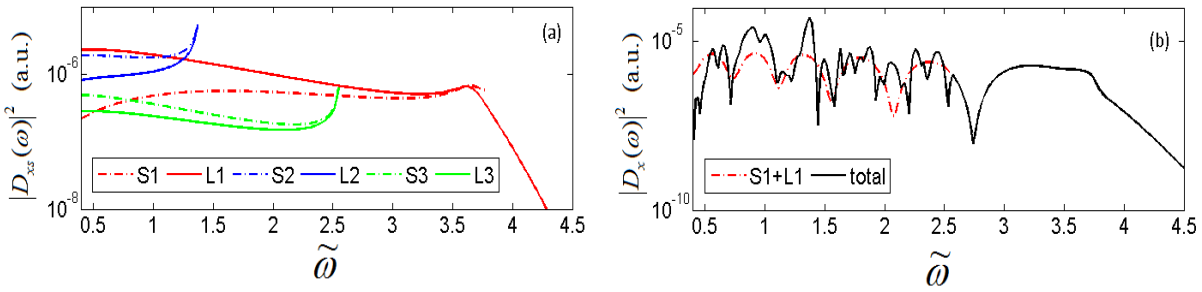

Figure 2.5: *(a) HHG spectrum from each individual quantum orbit born in half cycle. (b) HHG spectrum as a coherent summation of S1 and L1 (dashed red line) and summation of all orbits up to the fifth return (solid black line). The parameters are the same as in Fig. 2.1.*

QO theory for few-cycle laser pulses

The QO analysis can also be applied to the situation when the driving laser is a short pulse, for instance, a pulse with a cosine-squared envelope

$$E(t) = E_0 \cos^2\left(\frac{\pi t}{\tau}\right)\cos(\omega_L t + \psi) \quad -\frac{\tau}{2} \leq t \leq \frac{\tau}{2}. \tag{2.60}$$

Here τ is the total duration of this pulse, or equivalently, a full width at half maximum (FWHM) duration is approximately $\tau/2.75$, ψ is the carrier-envelope-phase (CEP), and E_0 is the peak electric field strength.

In the short pulse case (also called non-adiabatic case), due to the breakdown of periodicity we have to treat each half optical cycle individually. Specifically, we need to solve the saddle point equations (2.40) and (2.41) to get all quantum orbits for the whole pulse. Figure 2.6 shows the time profile of a short pulse and the corresponding HHG emission time of the first return as function of photon energy. Clearly, photons emitted in different half cycles have different cutoff energies. The total HHG spectrum is dominated by the emission

from a few half cycles near the center of the laser pulse, where the photon has the largest cutoff and ionization is also strongest. This is different from the monochromatic light case in which there are numerous half cycles that contribute to the harmonic spectrum equally. The HHG spectrum from a short laser pulse shows a complicated structure as in Fig. 2.7 other than sharp odd harmonics. Generally, a few-cycle laser pulse will yield a relatively broad and continuous HHG spectrum in the higher plateau. Fig. 2.7 also shows that the QO method is in qualitative agreement with the direct SFA integral given by Eq. (2.33). The cutoff position and the main features of the HHG spectrum are successfully reproduced by QO.

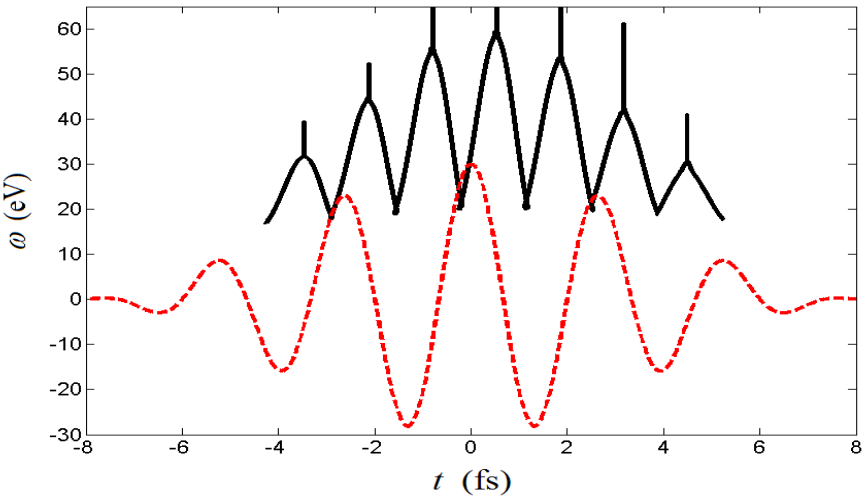

Figure 2.6: *Dashed red line: profile of the electric field of a short laser pulse. Solid black line: HHG emission time* $\mathrm{Re}\{t_s\}$ *as a function of photon energy (first return only), obtained from Eqs. (2.40) and (2.41) for argon* (I_p*=15.76 eV). Laser parameters: wavelength 800nm, peak intensity* 2.0×10^{14} *W/cm*^{2}*, FWHM 6 fs,* $\psi = 0$.

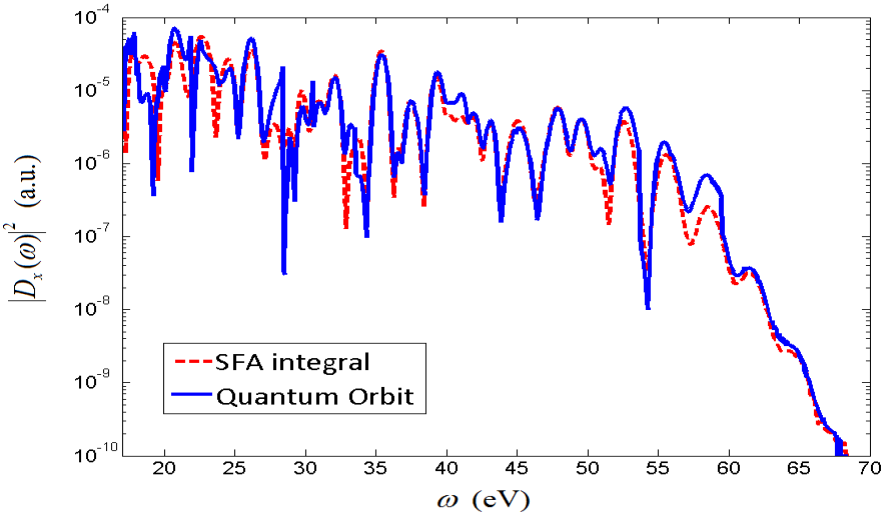

Figure 2.7: *HHG spectrum with the short pulse as given in Fig. 2.6, obtained from numerical SFA integral Eq. (2.33) (red dashed line) and from the quantum orbit method (blue solid line).*

2.2 QO analysis on HHG with mid-IR driving lasers

2.2.1 Long and short orbits at long wavelengths

In this section we apply the quantum orbit analysis on HHG driven by mid-infrared lasers. Let's imagine a situation when the laser wavelength λ is increased gradually while the field strength E_0 is fixed, such that the laser-atom interactions are kept in the tunneling regime. Since the HHG cutoff is determined by $I_p + 3.2U_p$ and $U_p \propto \lambda^2$, by using a mid-infrared laser the HHG spectrum may be extended to the water window or even the keV region. The Keldysh parameter

$$\gamma = \sqrt{\frac{I_p}{2U_p}} = \frac{\sqrt{2I_p}}{E_0}\omega_L \propto \lambda^{-1}, \tag{2.61}$$

where $\omega_L = 2\pi c/\lambda$ is the laser frequency. Clearly γ decreases as the wavelength is increased, thus in the long wavelength limit $\gamma \ll 1$ and ionization falls into the deep tunneling regime. In this limit tunneling (imaginary part of the born time) only occurs within a very tiny time interval compared to the optical period. Our goal here is to seek further simplification

in the QO theory in order to investigate the behavior of harmonics due to long and short orbits in this regime.

In the long wavelength limit, the saddle point equations (2.53) and (2.54) can be simplified by approximating the recombination time θ to be a real quantity[97, 110] while keeping the born time θ' complex. Here we separate the real and imaginary part of the ionization time explicitly: $\theta' = \alpha + i\beta$, $0 < \alpha < \frac{\pi}{2}$ and $\beta > 0$. The $\sin\theta'$ and $\cos\theta'$ term can be rewritten as

$$\sin\theta' = \sin(\alpha + i\beta) = \sin\alpha\cosh\beta + i\cos\alpha\sinh\beta, \tag{2.62}$$

$$\cos\theta' = \cos(\alpha + i\beta) = \cos\alpha\cosh\beta - i\sin\alpha\sinh\beta. \tag{2.63}$$

Since $\sin\theta$ is real in this approximation, by following the constraint Eq. (2.54), we have to approximate $\frac{\cos\theta - \cos\theta'}{\theta - \theta'}$ to be real consistently, i.e.

$$\begin{aligned}\frac{\cos\theta - \cos\theta'}{\theta - \theta'} &\approx \mathrm{Re}\left\{\frac{\cos\theta - \cos\theta'}{\theta - \theta'}\right\} = \mathrm{Re}\left\{\frac{\cos\theta - \cos\alpha\cosh\beta + i\sin\alpha\sinh\beta}{\theta - \alpha - i\beta}\right\} \\ &= \frac{(\cos\theta - \cos\alpha\cosh\beta)(\theta - \alpha) - \beta\sin\alpha\sinh\beta}{(\theta - \alpha)^2 + \beta^2}.\end{aligned} \tag{2.64}$$

Then Eqs. (2.53) and (2.54) can be reduced to

$$\cos\alpha\sinh\beta = \gamma, \tag{2.65}$$

$$\frac{(\cos\theta - \cos\alpha\cosh\beta)(\theta - \alpha) - \beta\sin\alpha\sinh\beta}{(\theta - \alpha)^2 + \beta^2} + \sin\alpha\cosh\beta = 0, \tag{2.66}$$

$$2(\sin\theta - \sin\alpha\cosh\beta)^2 = \tilde{\omega}. \tag{2.67}$$

When $\gamma \ll 1$ and the ionization time is not too far from the (sub-cycle) peak of the electric field, for example $0 < \alpha < \frac{\pi}{3}$, from Eq. (2.65) we get

$$\sinh\beta = \frac{\gamma}{\cos\alpha}, \tag{2.68}$$

$$\cosh\beta = \sqrt{1+\left(\frac{\gamma}{\cos\alpha}\right)^2} \approx 1+\frac{\gamma^2}{2\cos^2\alpha}, \tag{2.69}$$

$$\beta = \ln\left[\frac{\gamma}{\cos\alpha}+\sqrt{1+\left(\frac{\gamma}{\cos\alpha}\right)^2}\right] \approx \frac{\gamma}{\cos\alpha}-\frac{\gamma^3}{6\cos^3\alpha}. \tag{2.70}$$

Substituting Eqs. (2.68)-(2.70) into Eqs. (2.66) and (2.67) yields

$$(\cos\theta-\cos\alpha)+(\theta-\alpha)\sin\alpha+\frac{\gamma^2}{2\cos\alpha}\left(\frac{(\theta-\alpha)\sin\alpha}{\cos\alpha}-1\right)=0, \tag{2.71}$$

$$2(\sin\theta-\sin\alpha)^2-\frac{2\sin\alpha(\sin\theta-\sin\alpha)}{\cos^2\alpha}\gamma^2=\tilde{\omega}. \tag{2.72}$$

In Eqs. (2.71) and (2.72) we keep terms up to the order of γ^2. One can solve these equations to obtain the real born time α_s and return time θ_s for a given scaled photon energy $\tilde{\omega} = (\omega - I_p)/U_p$. These solutions will depend on the Keldysh parameter γ. Clearly as $\gamma \to 0$, Eqs. (2.71) and (2.72) reduce to classical equations (2.55) and (2.56), thus α_s and θ_s will converge to their classical counterparts θ_c' and θ_c, respectively. This convergence is shown in Fig. 2.8 for the first return. Higher order returns also have similar convergence. While clear differences can be seen for the 0.8 μm case in Fig. 2.8, the QO results become very close to the classical values quickly for $\lambda \gtrsim 1.6$ μm. Additionally, the born time of S1 converges slower than L1 in the small $\tilde{\omega}$ region. When $\tilde{\omega} \approx 1$ we observe that the born time of S1 changes significantly from 34° (0.8 μm case) to 48° (long wavelength case).

From Eq. (2.70) one can deduce that

$$\mathrm{Im}\{t_s'\} = \frac{\beta_s}{\omega_L} \approx \frac{\gamma}{\omega_L\cos\alpha_s} = \frac{\sqrt{2I_p}}{E_0\cos\alpha_s} = \frac{\sqrt{2I_p}}{E_s}. \tag{2.73}$$

Here $E_s = E_0\cos\alpha_s = E_0\cos(\omega_L \mathrm{Re}\{t_s'\})$ is the electric field right at the born time. When $\gamma \ll 1$, during the tunneling process the electric field can be treated as quasi-static with the strength E_s. Equation (2.73) indicates that the imaginary part of t_s' can be interpreted as a timescale of quantum tunneling[13]. Fig. 2.9(a) verifies that as the wavelength increases,

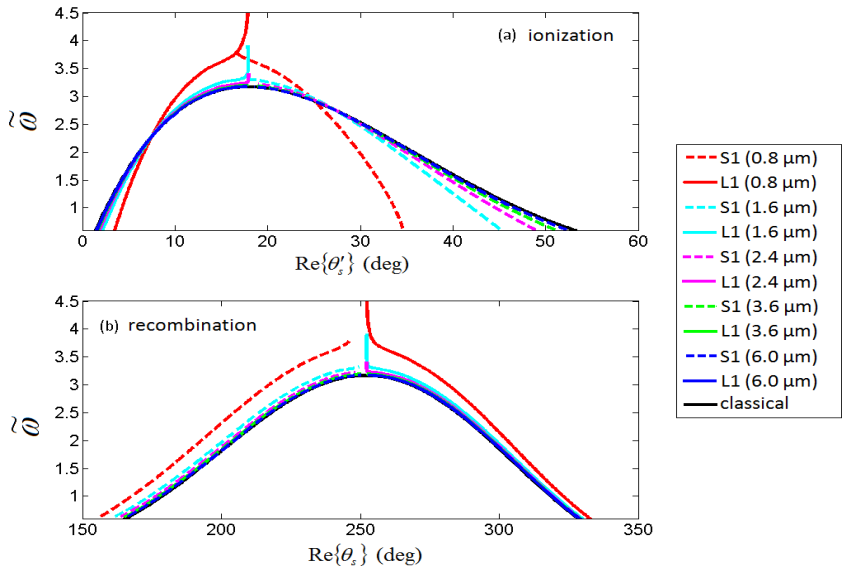

Figure 2.8: *The real part of (a) ionization time and (b) recombination time for the long (L1) and short (S1) orbit of the first return as functions of* $\tilde{\omega}$*, obtained by solving Eqs. (2.53) and (2.54) for wavelengths* $[0.8 - 6.0]$ *μm, peak intensity* 1.5×10^{14} *W/cm*^{2}*, argon target (*I_p*=15.76 eV). The classical born and return time are also shown as solid black curves.*

$\mathrm{Im}\{t_s'\}$ converges to $\frac{\sqrt{2I_p}}{E_0 \cos\theta_c'}$ (black curve) predicted by Eq. (2.73). Figure 2.9(b) shows that for long wavelengths the imaginary part of the recombination time $\mathrm{Im}\{t_s\}$ quickly converges to zero, which validates the approximations made in the above derivation.

Starting from Eq. (2.57), for a long quantum orbit ($\alpha_s < 17°$), when $\gamma \ll 1$, $\mathrm{Im}\{\Theta_s\}$ can

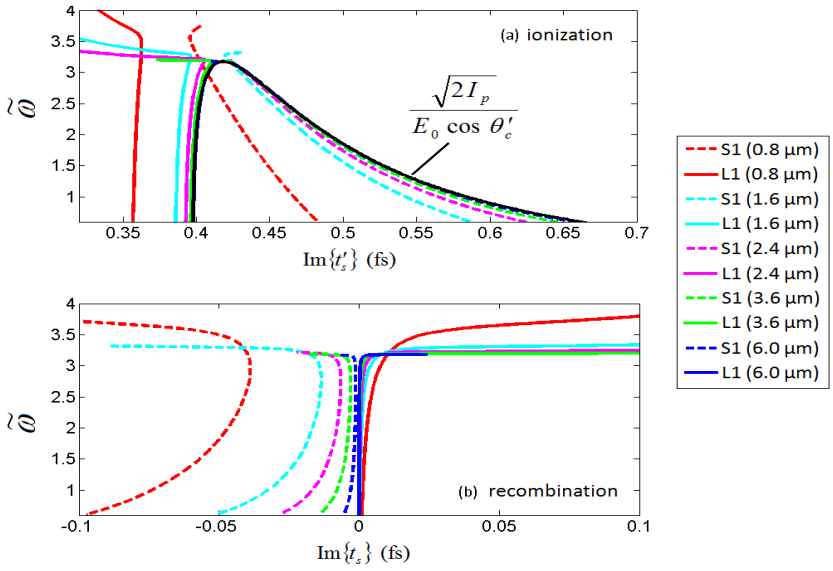

Figure 2.9: *(a)* $\mathrm{Im}\{t_s'\}$ *and (b)* $\mathrm{Im}\{t_s\}$ *for the long and short orbits of the first return as functions of* $\tilde{\omega}$ *obtained by solving Eqs. (2.53) and (2.54) for wavelengths* $[0.8 - 6.0]$ *μm. Other parameters are the same as in Fig. 2.8. The solid black curve in (a) shows the tunneling time given in Eq. (2.73) with* α_s *replaced by the classical born time* θ_c'.

be approximated as

$$
\begin{aligned}
\mathrm{Im}\{\Theta_s\} &\approx \frac{2U_p}{\omega_L}\left\{-\beta_s\left[\gamma^2+\frac{1}{2}-\sin^2\alpha_s\cosh^2\beta_s\right]+\frac{1}{2}\cos 2\alpha_s\sinh\beta_s\cosh\beta_s\right\}\\
&\approx \frac{2U_p}{\omega_L}\left\{-\left(\frac{\gamma}{\cos\alpha_s}-\frac{\gamma^3}{6\cos^3\alpha_s}\right)\left[\gamma^2+\frac{1}{2}-\sin^2\alpha_s\left(1+\frac{\gamma^2}{\cos^2\alpha_s}\right)\right]\right.\\
&\left.+\frac{1}{2}\cos 2\alpha_s\frac{\gamma}{\cos\alpha_s}\left(1+\frac{\gamma^2}{2\cos^2\alpha_s}\right)\right\}\\
&\approx -\frac{2U_p\gamma}{\omega_L\cos\alpha_s}\left\{\gamma^2+\frac{1}{2}-\sin^2\alpha_s-\frac{\gamma^2\sin^2\alpha_s}{\cos^2\alpha_s}-\frac{\gamma^2}{12\cos^2\alpha_s}\right.\\
&\left.+\frac{\gamma^2\sin^2\alpha_s}{6\cos^2\alpha_s}-\frac{1}{2}\cos 2\alpha_s-\frac{1}{4}\frac{\gamma^2\cos 2\alpha_s}{\cos^2\alpha_s}\right\}\\
&= -\frac{2U_p\gamma^3}{\omega_L\cos\alpha_s}\left\{1-\frac{5\sin^2\alpha_s}{6\cos^2\alpha_s}-\frac{1}{12\cos^2\alpha_s}-\frac{1}{4}\frac{\cos 2\alpha_s}{\cos^2\alpha_s}\right\}\\
&= -\frac{4U_p\gamma^3}{3\omega_L\cos\alpha_s}(1-\tan^2\alpha_s)\approx -\frac{(2I_p)^{3/2}}{3E_0\cos\alpha_s}.
\end{aligned}
\tag{2.74}
$$

From Eq. (2.44), contribution from this quantum orbit to HHG spectrum depends on an exponential factor

$$|D_{xs}(\omega)|^2 \propto e^{2\mathrm{Im}\{\Theta_s\}} \approx e^{-\frac{2(2I_p)^{3/2}}{3E_0\cos\alpha_s}} = e^{-\frac{2(2I_p)^{3/2}}{3E_s}}. \tag{2.75}$$

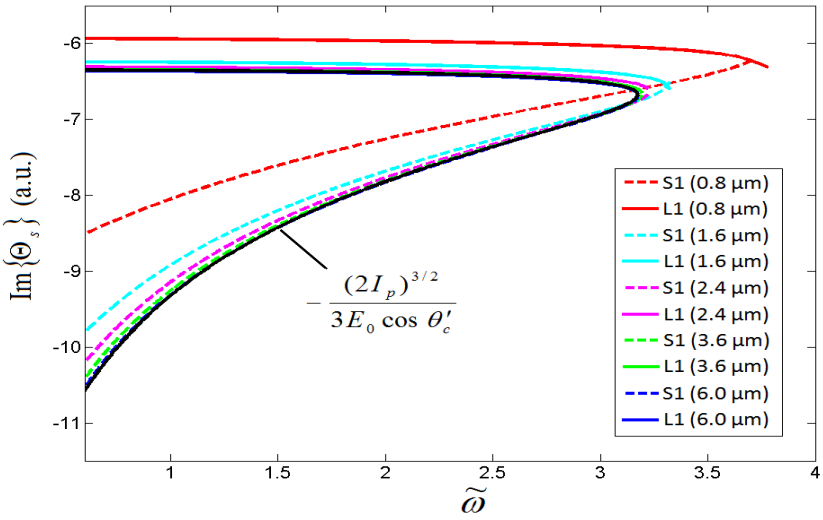

Figure 2.10: $\mathrm{Im}\{\Theta_s\}$ *for the long and short orbit of the first return as the function of* $\tilde{\omega}$ *given by Eq. (2.57) for wavelengths from 0.8 μm to 6.0 μm. Other parameters are the same as in Fig. 2.8. The solid black curve shows the factor given in Eq. (2.74) where* α_s *is replaced by the classical born time* θ_c'.

The exponential factor in Eq. (2.75) is similar to a Landau-Dykhne type of tunneling ionization for an atom in a static field E_s[13, 106]. Therefore the QO theory can account for the tunneling ionization rate in its electron wave packet. The derivation of $\mathrm{Im}\{\Theta_s\}$ for a short orbit is much more complicated than the derivation of Eq. (2.74). The former requires us to approximate the imaginary part of the recombination time $\mathrm{Im}\{\theta_s\}$ to the order of γ^3 rather than simply zero. Nevertheless for long wavelengths it is still reasonable to treat the electric field as quasi-static at the born time of the short orbit, thus the tunneling ionization rate Eq. (2.75) remains valid for the short orbits as well. This point has been verified in Fig. 2.10 which shows that, as the laser wavelength increases, $\mathrm{Im}\{\Theta_s\}$ converges to the

factor $-\frac{(2I_p)^{3/2}}{3E_0\cos\theta_c'}$ (solid black curve) for both long and short orbits.

2.2.2 Electron wave packet and scaling law at long wavelengths

Based on Eqs. (2.46)-(2.48), (2.49) and (2.50) one can derive

$$|\det(S'')| = \frac{E_0^4}{\omega_L^2}\frac{|G_{11}G_{22} - G_{12}G_{21}|}{|\theta_s - \theta_s'|^2}, \tag{2.76}$$

where

$$G_{11}(\theta_s', \theta_s) = -\left(g(\theta_s', \theta_s) + \sin\theta_s\right)^2 + (\theta_s - \theta_s')\cos\theta_s'[g(\theta_s', \theta_s) + \sin\theta_s], \tag{2.77}$$

$$G_{22}(\theta_s', \theta_s) = -\left(g(\theta_s', \theta_s) + \sin\theta_s'\right)^2 - (\theta_s - \theta_s')\cos\theta_s'[g(\theta_s', \theta_s) + \sin\theta_s'], \tag{2.78}$$

$$G_{12}(\theta_s', \theta_s) = G_{21}(\theta_s', \theta_s) = \left(g(\theta_s', \theta_s) + \sin\theta_s\right)\left(g(\theta_s', \theta_s) + \sin\theta_s'\right), \tag{2.79}$$

and

$$g(\theta_s', \theta_s) = \frac{\cos\theta_s - \cos\theta_s'}{\theta_s - \theta_s'}. \tag{2.80}$$

By combining Eqs. (2.53) and (2.54) we get

$$\begin{aligned} & G_{11}G_{22} - G_{12}G_{21} \\ = \; & (g(\theta_s', \theta_s) + \sin\theta_s')(g(\theta_s', \theta_s) + \sin\theta_s)(\theta_s - \theta_s')^2\cos\theta_s'\left(\frac{\sin\theta_s - \sin\theta_s'}{\theta_s - \theta_s'} - \cos\theta_s'\right) \\ = \; & \pm i\gamma\sqrt{\frac{\widetilde{\omega}}{2}}(\theta_s - \theta_s')^2\cos\theta_s'\left(\frac{\sin\theta_s - \sin\theta_s'}{\theta_s - \theta_s'} - \cos\theta_s'\right). \end{aligned} \tag{2.81}$$

Thus

$$|\det(S'')| = \frac{\gamma E_0^4}{\omega_L^2}\sqrt{\frac{\widetilde{\omega}}{2}}|\cos\theta_s'|\left|\frac{\sin\theta_s - \sin\theta_s'}{\theta_s - \theta_s'} - \cos\theta_s'\right|. \tag{2.82}$$

Additionally, we notice that from Eqs. (2.40) and (2.41),

$$|d_x(p_s + A(t'_s))| = |d_x(i\sqrt{2I_p})|, \tag{2.83}$$

$$|d^*_x(p_s + A(t_s))| = |d_x(\sqrt{2(\omega - I_p)})| = |d_x(\sqrt{2\tilde{\omega}U_p})|. \tag{2.84}$$

Substituting the above results into Eq. (2.44) one can rewrite the harmonic spectrum from a particular quantum orbit as

$$\begin{aligned} |D_{xs}(\omega)|^2 &\propto \frac{1}{|\det(S'')|}\left|\frac{\omega_L}{\theta_s - \theta'_s}\right|^3 |d_x(\sqrt{2\tilde{\omega}U_p})|^2 E_0^2 |\cos\theta'_s|^2 e^{-\frac{2(2I_p)^{3/2}}{3E_0\cos\alpha_s}} \\ &\propto \frac{\omega_L^5}{\gamma E_0^2\sqrt{\tilde{\omega}}}|d_x(\sqrt{2\tilde{\omega}U_p})|^2 f_s(\theta'_s, \theta_s) \\ &\propto \lambda^{-4}\tilde{\omega}^{-1/2}E_0^{-1}|d_x(\frac{E_0\sqrt{2\tilde{\omega}}}{4\pi c}\lambda)|^2 f_s(\theta'_s, \theta_s). \end{aligned} \tag{2.85}$$

Here $f_s(\theta'_s, \theta_s)$ is a function that depends on (θ'_s, θ_s). Note that here and in the following we omit the factor $|d_x(i\sqrt{2I_p})|^2$, which is a constant for a given target. Since saddle point solutions (θ'_s, θ_s) relies on $\tilde{\omega}$ and $\gamma \propto \lambda^{-1}$, $f_s(\theta'_s, \theta_s)$ can also be treated as a function of $\tilde{\omega}$ and λ which reads

$$F_s(\tilde{\omega}, \lambda) = f_s(\theta'_s, \theta_s) = \frac{|\cos\theta'_s| e^{-\frac{2(2I_p)^{3/2}}{3E_0\cos(\mathrm{Re}\{\theta'_s\})}}}{\left|\frac{\sin\theta_s - \sin\theta'_s}{\theta_s - \theta'_s} - \cos\theta'_s\right| |\theta_s - \theta'_s|^3}. \tag{2.86}$$

Equation (2.85) shows that the wavelength scaling of $|D_{xs}(\omega)|^2$ at a fixed scaled energy $\tilde{\omega}$ depends on the form of $d_x(p)$ and thus on the target, as discussed in[111]. Following the idea of QRS theory[101] we can get rid of the target-dependent transition dipole and only study the wavelength scaling of the returning electron wave packet. For convenience here we define the wave packet $W(\omega)$ as the HHG yield $P(\omega)$ divided by the photorecombination

cross section $\sigma(\omega)$

$$W(\omega) \propto \frac{P(\omega)}{\sigma(\omega)} = \frac{\omega^4 |D_x(\omega)|^2}{\frac{4\pi^2\omega^3}{cp}|d_x(p)|^2} = \frac{c}{4\pi^2}\frac{\omega\sqrt{2(\omega - I_p)}|D_x(\omega)|^2}{|d_x(\sqrt{2(\omega - I_p)})|^2}. \tag{2.87}$$

Then the electron wave packet of a particular quantum orbit follows (assuming $\omega \gg I_p$)

$$W_s(\tilde{\omega}) \propto \frac{\tilde{\omega}U_p\sqrt{2\tilde{\omega}U_p}|D_{xs}(\omega)|^2}{|d_x(\sqrt{2\tilde{\omega}U_p})|^2} \propto (\tilde{\omega}U_p)^{3/2}\lambda^{-4}\tilde{\omega}^{-1/2}E_0^{-1}F_s(\tilde{\omega},\lambda) \propto \lambda^{-1}\tilde{\omega}E_0^2F_s(\tilde{\omega},\lambda). \tag{2.88}$$

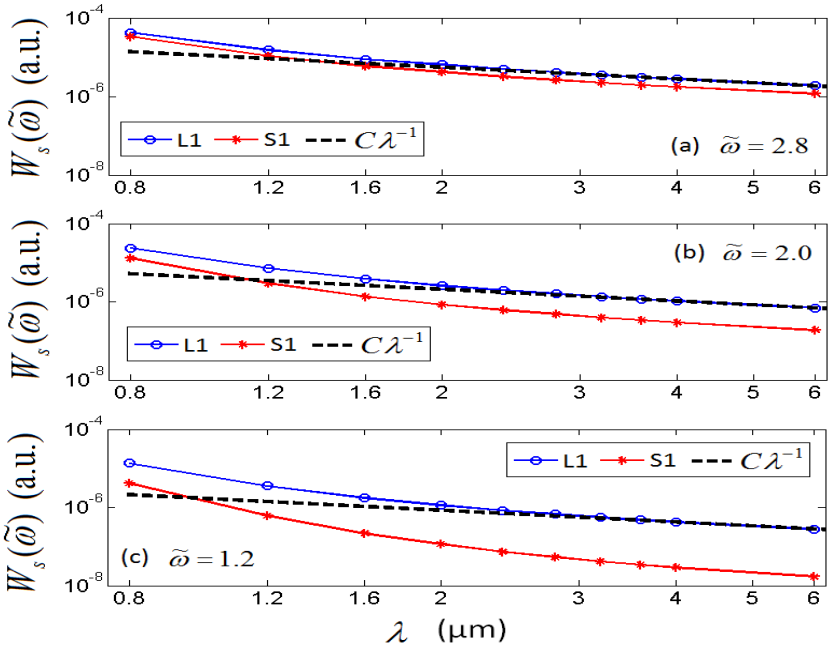

Figure 2.11: *Wavelength scaling of the electron wave packet of the long and short orbit in the first return, at (a) $\tilde{\omega} = 2.8$ (b) $\tilde{\omega} = 2.0$ (c) $\tilde{\omega} = 1.2$. Other parameters are the same as in Fig. 2.8.*

For very long wavelength we can expect that $\gamma \to 0$ and (θ_s', θ_s) converges to its classical counterpart (θ_c', θ_c), thus $F_s(\tilde{\omega}, \lambda)$ will reduce to a wavelength independent factor $\tilde{F}_s(\tilde{\omega})$

which reads

$$\tilde{F}_s(\tilde{\omega}) = f_s(\theta_c', \theta_c) = \frac{|\cos\theta_c'| e^{-\frac{2(2I_p)^{3/2}}{3E_0\cos\theta_c'}}}{\left|\frac{\sin\theta_c - \sin\theta_c'}{\theta_c - \theta_c'} - \cos\theta_c'\right| |\theta_c - \theta_c'|^3}. \tag{2.89}$$

Therefore in the region of sufficiently long wavelength the electron wave packet follows

$$W_s(\tilde{\omega}) \propto \lambda^{-1}\tilde{\omega}E_0^2\tilde{F}_s(\tilde{\omega}). \tag{2.90}$$

Figure 2.11 shows the λ scaling of the electron wave packet for both short and long quantum orbits at three $\tilde{\omega}$ values. From Eq. (2.88), at a fixed scaled energy $\tilde{\omega}$, $W_s \propto \lambda^{-1}F_s(\tilde{\omega}, \lambda)$. For $\lambda \lesssim 2.0$ μm, the scaling law deviates from λ^{-1}, indicating some dependence of $F_s(\tilde{\omega}, \lambda)$ on λ. From 0.8 μm to 2.0 μm the wave packet drops quickly, especially for the short orbits at energies $\tilde{\omega} = 1.2$. On the other hand, as the wavelength increases beyond about 2.4 μm, one can observe a rough λ^{-1} scaling law for both long and short orbits and for all $\tilde{\omega}$ values. This λ^{-1} dependence is predicted by Eq. (2.90). This general behavior has been confirmed by the TDSE calculations for different atoms[98].

Next we study the profile of electron wave packet as a function of $\tilde{\omega}$. For convenience, we define a scaled wave packet as $\tilde{W}_s = \lambda W_s$. According to Eq. (2.88), $\tilde{W}_s$ has a λ dependent profile $\tilde{\omega}F_s(\tilde{\omega}, \lambda)$. As λ increases, Eq. (2.90) predicts that this profile will converge to a universal form $\tilde{\omega}\tilde{F}_s(\tilde{\omega})$. The convergence of L1 and S1 wave packets is shown in Fig. 2.12. It can be shown that the wave packets of higher order quantum orbits also converge in a similar fashion. One can observe that S1 wave packet converges somewhat slower than L1, which is consistent with the behavior of ionization time for S1 and L1 orbits [see Fig. 2.8(a)]. The agreement with the "classical limit" (dot-dashed curve) gets worse near the cutoff. This is probably due to the influence of the artificial divergence imposed by the saddle-point approximation. A similar trend has been found in the TDSE results reported in Ref. [98], where the convergence to a universal limit was found as soon as above $\lambda \approx 3$ μm.

Figure 2.13 shows the factor $\tilde{F}_s(\tilde{\omega})$ for each quantum orbit up to the third return. $\tilde{F}_s(\tilde{\omega})$ for S1 orbit decreases rapidly from higher plateau to lower plateau, while $\tilde{F}_s(\tilde{\omega})$ for other

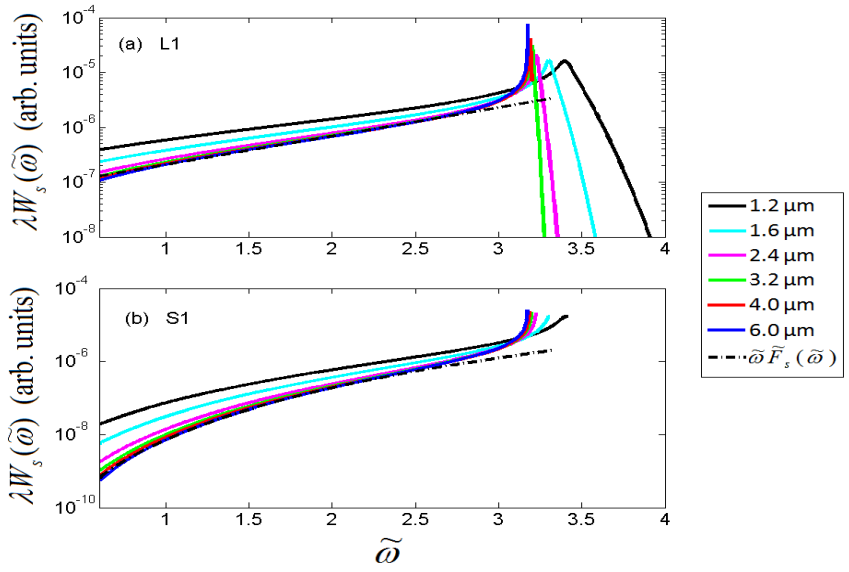

Figure 2.12: *The electron wave packet of (a) long orbit and (b) short orbit at different wavelengths. Other parameters are the same as in Fig. 2.8. Wave packets have been rescaled by a factor of λ in order to show the convergence. The dot-dashed black curve shows the factor $\tilde{\omega}\tilde{F}_s(\tilde{\omega})$.*

orbits are relatively more flat. We can deduce that for very long wavelengths L1 is the dominant orbit to the total wave packet, and higher order returns, especially the S2 orbit, also have considerable contribution. The role of higher order returns discussed here is in good agreement with the observation in Refs. [87, 112, 113].

We can also approximately derive the wavelength scaling law at a fixed absolute photon energy ω in the long wavelength region. For that purpose, we first approximately fit the factor $\tilde{F}_s(\tilde{\omega})$ as $\tilde{F}_{S1}(\tilde{\omega}) \propto \tilde{\omega}^{3.7}$ for the short orbit and $\tilde{F}_{L1}(\tilde{\omega}) \propto \tilde{\omega}^{0.8}$ for the long orbit, as we can see in Fig. 2.13. Using Eq. (2.90), we get for the long orbit

$$W_{L1}(\omega) \propto \lambda^{-1}\tilde{\omega}^{1.8} \propto \lambda^{-1}U_p^{-1.8} \propto \lambda^{-4.6}, \tag{2.91}$$

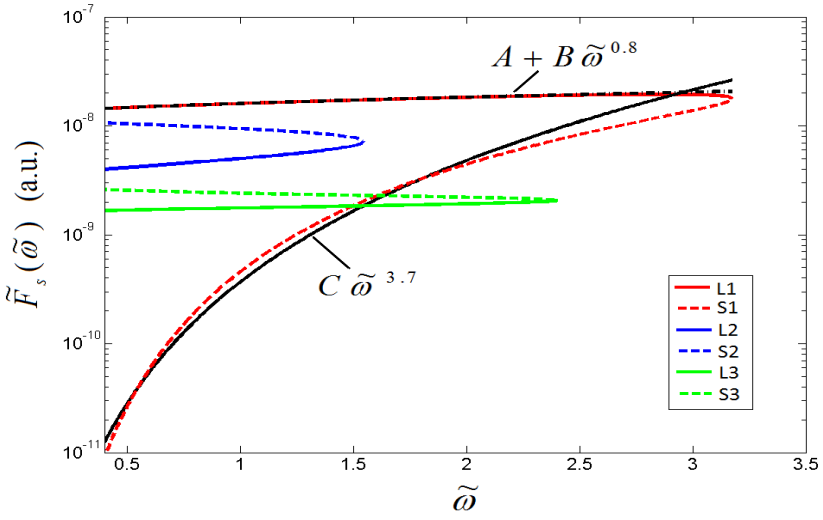

Figure 2.13: *The factor $\tilde{F}_s(\tilde{\omega})$ given in Eq. (2.89) for different quantum orbits up to the third return.*

and for the short orbit

$$W_{S1}(\omega) \propto \lambda^{-1}\tilde{\omega}^{4.7} \propto \lambda^{-1}U_p^{-4.7} \propto \lambda^{-10.4}. \tag{2.92}$$

Note that, by definition Eq. (2.87), at a fixed absolute photon energy ω, the wavelength scaling of HHG yield $P_s(\omega)$ is the same as the scaling of electron wave packet given in Eqs. (2.91) and (2.92). Since HHG at single atom level is mostly dominated by the long orbit L1 (see Fig. 2.13), the scaling law for the total HHG yield (from all quantum orbits) is only slightly different from Eq. (2.91). In fact, the scaling law $\lambda^{-4.2}$ was obtained in Ref. [98] for λ in $[3.0 - 6.0]$ μm. Note that the apparent discrepancy, as compared to the scaling law of $\lambda^{-(5-6)}$ reported earlier[87, 88, 111] has been mostly resolved as due to the different definitions for HHG yield used in these papers as compared to Ref. [98] and the present dissertation. Indeed, their definition, i.e., HHG yield per unit time, differs from ours by a factor of $T_L^{-1} \propto \lambda^{-1}$.

The universal wave packet in the long wavelength limit as given by Eqs. (2.89) and (2.90) and its approximate fitting shown in Fig. 2.13 can be used as simple estimates for realistic

HHG simulation with mid-infrared lasers. Although the analysis presented here is for a monochromatic driving laser, it can also be performed, in principle, for the case of short pulses.

2.3 Macroscopic propagation of long and short quantum orbits

The discussions so far are at single atom level, however to simulate experimental HHG measurements, propagation of the fundamental and high-harmonic fields in the medium needs to be considered. It is easy to understand that phase matching condition for different quantum orbits are quite different[17]. In Fig. 2.14 we separate the contributions from short orbit (S1), long orbit (L1) and higher return orbits (up to the third) to the macroscopic HHG yield. We used the induced dipole calculated from the QO method as the source term in the propagation equation. The HHG yield is defined as the integrated harmonic field intensity right at the rear face of the gas jet. The 0.8 μm case shown in Fig. 2.14 (a) is well understood: as the gas jet is placed after the laser focus, the short orbit (S1) is effectively selected, the long orbit only contributes near the cutoff. For longer wavelengths phase matching becomes more sensitive to experimental setup. Simulations for a typical setup using a tightly focused 1.6 μm laser beam are shown in Fig 2.14 (b) and (c), with the gas jet placed at $z = 1$ mm and 3.5 mm after the laser focus, respectively. For $z = 1$ mm the long orbit dominates the HHG yield. Higher order returns contribute mainly below about 50 eV ($1.5U_p + I_p$), which indicates that this contribution comes mostly from the second return. Good phase matching is achieved in the $z = 3.5$ mm case, which resembles the 0.8 μm, $z = 2$ mm case above. Here, the HHG spectrum shows clear harmonic peaks but the cutoff is somewhat reduced. The short orbit dominates the total yield and there is hardly any signature from long orbits and higher order returns. Although higher order return orbits have considerable contribution to single atom harmonics, because they accumulate a

relatively large phase in the continuum and they are more sensitive to laser intensity, their net contribution to the macroscopic harmonics becomes negligible after propagation.

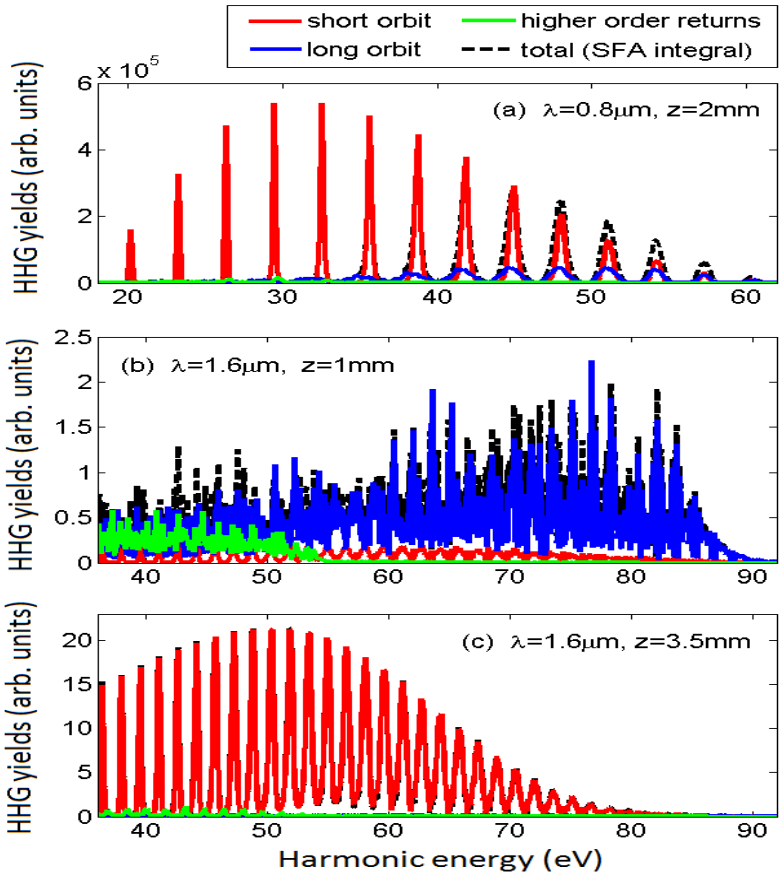

Figure 2.14: *Macroscopic HHG yield after propagating in an Ar gas jet of 1 mm thick placed after the laser focus. The laser pulse has a cosine-squared envelope with 30 cycles total duration, CEP=0. (a) 0.8 μm laser with beam waist 25 μm, the center of the gas jet is at $z = 2$ mm where the peak intensity is 2.0×10^{14} W/cm^2 ($U_p = 12$ eV). (b) 1.6 μm laser with beam waist 36 μm, the center of the gas jet is at $z = 1$ mm where the peak intensity is 1.0×10^{14} W/cm^2 ($U_p = 24$ eV). (c) the center of the gas jet is at $z = 3.5$ mm, other parameters are the same as in (b).*

2.4 Summary and outlook

In this chapter we examine the wavelength dependence of the HHG yield which serves as a basis of generating ultra-broadband attosecond pulses covering the water window or even keV region. The tool used in this chapter is the QO theory, which is derived from the SFA model with saddle-point approximations on the integral over t and t'. At single-atom level, the real part of the born and return time calculated from QO theory converge to the classical born and return time as the driving wavelength increases. At long wavelength limit, the Keldysh parameter $\gamma \ll 1$, ionization falls into deep tunneling regime, and the imaginary part of the QO born time is related to the tunneling time for the valence electron to be released. The returning wave packets as functions of the scaled photon energy corresponding to a particular quantum orbit also converge to a universal form. The short orbits are typically weaker than long orbits, especially at lower photon energies, for example, below $2U_p + I_p$, mainly because the electric field strength at the moment when the short orbit is ionized is weaker than that at the moment when the long orbit is ionized. At a fixed photon energy, the wavelength dependence of the HHG yield for the long orbit is $\lambda^{-4.6}$ and for the short orbit $\lambda^{-10.4}$. The HHG yield scales unfavorably with increased laser wavelength, and the situation gets even worse for short orbits.

Considering macroscopic propagation, good phase matching tends to select the short orbit. Therefore it is very challenging to obtain efficient macroscopic harmonic emission with long wavelength driving field. Recently it has been demonstrated[114] that by combining just two or three lasers of different colors, the HHG yields can be enhanced by two or more orders of magnitude, as compared to the single color one without the increase of the total pulse energy. The strategy there is to generate a synthesized laser waveform which would enhance the short orbit contribution at single-atom level.

Chapter 3

Characterization of isolated attosecond pulses with FROG-CRAB

The topic in this and the next chapter is retrieving IAPs from photoelectron spectrograms obtained by XUV plus IR two-color streaking measurements. This chapter focuses on the widely-used FROG-CRAB method[47] which stems from the FROG method[42]. The latter is an optical technique and has succeeded in characterizing picosecond or femtosecond laser pulses. However it is difficult to precisely model the two-color photoionization process when the IR intensity is strong. The application of FROG-CRAB on photoelectron spectrograms relies on a few approximations such as the strong field approximation (SFA) and the central momentum approximation. Therefore, it would be necessary to investigate the accuracy of the FROG-CRAB.

We start from Section 3.1 on how the IAP is described mathematically, which is definitely the fundamental of pulse characterization. Then in Section 3.2.1 to 3.2.3 we discuss the theoretical background of FROG-CRAB including the SFA and the central momentum approximation. Since the SFA model includes the bound-continuum dipole transition matrix element, in Section 3.2.2 we present how to calculate this dipole moment using one-electron model potential in more details. In Section 3.2.3 a photoelectron wave packet is introduced

which is an important concept and will be used in Chapter 5. Section 3.3.1 shows a few simulations where the SFA is used to generate spectrograms and the FROG-CRAB is applied to retrieve the input IAPs. In these simulations the IAPs are centered at a photon energy of 60 eV. On the other hand, it is known that SFA is not accurate in the low-energy region. Therefore we carry out another set of simulations using TDSE to generate spectrograms. In these simulations the input IAPs are centered at 40 eV and 22 eV in photon energy. The details of such TDSE simulations are shown in Section 3.3.2. The FROG-CRAB can not only retrieve the input XUV pulse but also the IR pulse. Section 3.3.3 discuss the accuracy of IR retrieval by FROG-CRAB and present an improved fitting method. In the end this chapter is summarized in Section 3.4.

3.1 Mathematical description of the IAP

Mathematically, an IAP can be described in the time domain

$$E_{XUV}(t) = \sqrt{I(t)}\cos[\Omega_0 t + \phi(t)], \tag{3.1}$$

or in the frequency domain

$$\tilde{E}_{XUV}(\Omega) = U(\Omega)e^{i\Phi(\Omega)}. \tag{3.2}$$

Equations (3.1) and (3.2) are related by Fourier transform

$$\tilde{E}_{XUV}(\Omega) = \int_{-\infty}^{\infty} E_{XUV}(t)e^{i\Omega t}dt, \tag{3.3}$$

$$E_{XUV}(t) = \frac{1}{2\pi}\int_{-\infty}^{\infty} \tilde{E}_{XUV}(\Omega)e^{-i\Omega t}d\Omega = \frac{1}{\pi}\int_{0}^{\infty} U(\Omega)\cos[\Omega t - \Phi(\Omega)]d\Omega. \tag{3.4}$$

In Eq. (3.1) $I(t)$ is the temporal intensity profile from which the pulse duration can be deduced, $\phi(t)$ is a temporal phase including attochirps, Ω_0 is the central frequency of the IAP. In Eq. (3.2) $U(\Omega)$ and $\Phi(\Omega)$ are the spectral amplitude and phase respectively. Since

$E_{XUV}(t)$ is real, it is obvious that $U(-\Omega) = U(\Omega)$ and $\Phi(-\Omega) = -\Phi(\Omega)$, thus in the following discussion we usually consider positive Ω only.

The temporal profile of the IAP does not only depend on the spectral amplitude $U(\Omega)$ but also on the spectral phase $\Phi(\Omega)$. Let us assume $U(\Omega)$ takes a simple Gaussian form

$$U(\Omega) = U_0 e^{-2\ln 2 \frac{(\Omega-\Omega_0)^2}{(\Delta\Omega)^2}}, \tag{3.5}$$

where its FWHM bandwidth is given by $\Delta\Omega$. Consider the simplest phase $\Phi(\Omega) = \Phi_0$ which is an energy-independent constant, by doing inverse Fourier transform we can obtain the pulse in time domain

$$E_{XUV}(t) = E_0 e^{-2\ln 2 \frac{t^2}{(\Delta t)^2}} \cos(\Omega_0 t - \Phi_0). \tag{3.6}$$

Here Δt is the FWHM duration of the pulse, which satisfies

$$\Delta\Omega\Delta t = 4\ln 2. \tag{3.7}$$

Then we add a linear term to the spectral phase, that is $\Phi(\Omega) = \Phi_0 + (\Omega - \Omega_0)\tau$. Easily one can find that in this case

$$E_{XUV}(t) = E_0 e^{-2\ln 2 \frac{(t-\tau)^2}{(\Delta t)^2}} \cos(\Omega_0 t - \Phi_0). \tag{3.8}$$

Compared to Eq. (3.6), the pulse envelope is delayed by an amount of τ with its shape kept the same.

Next we consider an important case that the spectral phase has a quadratic term $\Phi(\Omega) = \Phi_0 + (\Omega - \Omega_0)\tau + \frac{\beta}{2}(\Omega - \Omega_0)^2$. By taking the inverse Fourier transform, in time domain the pulse will be

$$E_{XUV}(t) = E_0 e^{-2\ln 2 \frac{(t-\tau)^2}{(\Delta t)^2}} \cos\left[\Omega_0 t + \xi \frac{2\ln 2}{(\Delta t)^2}(t-\tau)^2 - \Phi_0 - \frac{1}{2}\arctan\xi\right]. \tag{3.9}$$

Here the FWHM duration Δt satisfies

$$\Delta\Omega\Delta t = 4\ln 2\sqrt{1+\xi^2}, \tag{3.10}$$

and the parameter ξ is determined by

$$\xi = \frac{\beta(\Delta\Omega)^2}{4\ln 2}. \tag{3.11}$$

From Eq. (3.9) we can see the quadratic term in $\Phi(\Omega)$ leads to a linear chirp in the time domain. β or ξ is the evaluation of the amount of attochirp. From Eqs. (3.7) and (3.10) one can conclude that given the same spectral bandwidth $\Delta\Omega$, the transform-limited (TL) pulse (corresponding to $\beta = 0$) has the shortest temporal duration, whereas the duration of a chirped pulse will expand by a factor of $\sqrt{1+\xi^2}$ compared to the TL pulse.

In general, we can approximate the spectral phase $\Phi(\Omega)$ in the vicinity of Ω_0 by Taylor's expansion

$$\Phi(\Omega) \approx \Phi(\Omega_0) + \left.\frac{d\Phi}{d\Omega}\right|_{\Omega_0}(\Omega-\Omega_0) + \frac{1}{2}\left.\frac{d^2\Phi}{d\Omega^2}\right|_{\Omega_0}(\Omega-\Omega_0)^2 + ... \tag{3.12}$$

According to the above discussion, similar to femtosecond laser pulses we can define the group delay of this attosecond pulse

$$\tau_G = \frac{d}{d\Omega}\Phi(\Omega), \tag{3.13}$$

and the group delay dispersion (GDD)

$$\beta = \frac{d\tau_G}{d\Omega} = \frac{d^2}{d\Omega^2}\Phi(\Omega). \tag{3.14}$$

3.2 Theoretical background of FROG-CRAB

3.2.1 SFA model for XUV plus IR photoionization

To relate the phase information to the streaking spectrogram we need to consider a quantum mechanical model. The first assumption is that the photoelectron spectra can be calculated using the SFA model[115]:

$$S(p,\tau) = \left| \int_{-\infty}^{\infty} E_{XUV}(t-\tau) d(p+A(t)) e^{-i\varphi(p,t)} e^{i\left(\frac{p^2}{2}+I_p\right)t} dt \right|^2 . \tag{3.15}$$

Here the polarization of the XUV, the IR, and the photoelectrons are all taken along the $+z$ direction, so all quantities become scalars. $A(t)$ is the vector potential of the IR field. p is the asymptotic momentum of the photoelectron, and the energy of the electron $E = p^2/2$. τ is the relative temporal shift between the XUV and IR fields. A positive τ means the XUV comes after the peak of the IR field. The function $\varphi(p,t)$ is given by

$$\varphi(p,t) = \int_t^{\infty} \left[pA(t') + \frac{1}{2}A^2(t') \right] dt'. \tag{3.16}$$

As in the case of HHG, the SFA model does not take into account the interactions between the continuum electron and the ionic core. For high energy photoelectrons this interaction is not important such that the SFA is a good approximation. On the other hand, the SFA becomes less accurate when considering low energy photoelectrons.

3.2.2 Single photon transition dipole moment

Equation (3.15) includes the single photon transition dipole, $d(p) = \langle p\mathbf{e}_z|z|i\rangle$, where $|i\rangle$ is the initial bound state with the ionization potential I_p. In the standard SFA, the continuum state $|p\mathbf{e}_z\rangle$ is approximated by a plane wave state e^{ipz} in the coordinate space. A correct choice is to use the scattering wave function which is a continuum eigenstate of the field-free

Hamiltonian with asymptotic momentum $p\mathbf{e}_z$.

In the single-active-electron (SAE) approximation, consider the field free Hamiltonian

$$H_0 = -\frac{1}{2}\nabla^2 + V(r) \tag{3.17}$$

in which the effective potential of the ionic core is modeled by

$$V(r) = -\frac{Z_c + a_1 e^{-a_2 r} + a_3 r e^{-a_4 r} + a_5 e^{-a_6 r}}{r}. \tag{3.18}$$

Here $Z_c = 1$ is the asymptotic charge seen by the active electron. The coefficients a_i are obtained by fitting the numerical potential calculated from the self-interaction free density functional theory, which can be found in Ref.[116] for noble gas atoms.

The eigenstates of H_0 consist of both bound and continuum part. The ground state associated to an angular momentum quantum number l_i and a magnetic quantum number m_i can be written as

$$\langle \mathbf{r}|i\rangle = \frac{u_i(r)}{r} Y_{l_i m_i}(\theta, \varphi), \tag{3.19}$$

where $\mathbf{r} = (r, \theta, \varphi)$ is the position vector and Y_{lm} is a spherical harmonic. The continuum state with asymptotic energy $E = k^2/2$ and quantum numbers L, M reads

$$\langle \mathbf{r}|kLM\rangle = \frac{u_{kL}(r)}{r} Y_{LM}(\theta, \varphi). \tag{3.20}$$

The energy normalized radial wave function $u_{kL}(r)$ has the asymptotic form

$$\lim_{r\to\infty} u_{kL}(r) = \sqrt{\frac{2}{\pi k}} \sin\left(kr + \frac{Z_c}{k}\ln(2kr) + \eta_L(E)\right). \tag{3.21}$$

The partial wave phase shift

$$\eta_L(E) = -\frac{L\pi}{2} + \sigma_L(E) + \delta_L(E), \tag{3.22}$$

where $\sigma_L(E) = \arg[\Gamma(L+1-iZ_c/k)]$ is the Coulomb phase shift, while $\delta_L(E)$ is the phase shift due to the short-range part in $V(r)$.

The final photoelectron state with momentum $\mathbf{k} = (k, \theta_k, \varphi_k)$ can be expanded by partial waves

$$\langle \mathbf{r}|\mathbf{k}\rangle = \sum_{L,M} e^{-i\eta_L(E)} Y^*_{LM}(\theta_k, \varphi_k) Y_{LM}(\theta, \varphi) \frac{u_{kL}(r)}{r}. \tag{3.23}$$

This wavefunction behaves asymptotically as the superposition of a plane wave plus an incoming spherical wave. Specifically for the photoelectron emitted along the z axis, $\theta_k = 0$, only the $M = 0$ part exists,

$$\langle \mathbf{r}|k\mathbf{e}_z\rangle = \sum_{L} e^{-i\eta_L(E)} \sqrt{\frac{2L+1}{4\pi}} Y_{L0}(\theta, \varphi) \frac{u_{kL}(r)}{r}. \tag{3.24}$$

Then the single photon transition dipole can be calculated using Eqs. (3.19) and (3.24),

$$d(E) = \langle k\mathbf{e}_z|z|i\rangle = \sum_{L} \sqrt{\frac{2L+1}{4\pi}} e^{i\eta_L(E)} \langle u_{kL}|r|u_i\rangle \langle Y_{L0}|\cos\theta|Y_{l_i m_i}\rangle. \tag{3.25}$$

As a result of the dipole selection rule we can only include the $m_i = 0$ channel for forward photoelectrons. If the photoionization is from s states ($l_i = 0$), the transition dipole involves the continuum p-wave only

$$d(E) = \sqrt{\frac{1}{4\pi}} e^{i\eta_1(E)} \langle u_{k1}|r|u_i\rangle. \tag{3.26}$$

However if the photoionization is from p states ($l_i = 1$), the transition dipole involves both the continuum s-wave and d-wave

$$d(E) = \sqrt{\frac{1}{12\pi}} \left\{ e^{i\eta_0(E)} \langle u_{k0}|r|u_i\rangle + 2e^{i\eta_2(E)} \langle u_{k2}|r|u_i\rangle \right\}. \tag{3.27}$$

Figure 3.1 gives the single photon transition dipoles from the outermost subshells of Ar

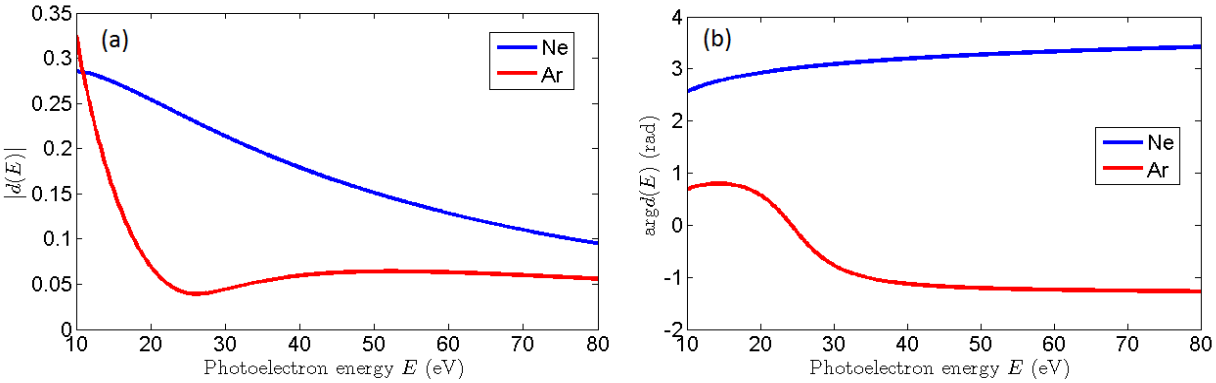

Figure 3.1: *(a) Amplitude and (b) Phase of the single photon transition dipole matrix element from Ar (3p subshell) and Ne (2p subshell).*

and Ne atoms, which are calculated according to Eq. (3.27). The dipole amplitude of Ne drops monotonically whereas the amplitude of Ar shows a Cooper minimum[117] at $E = 26$ eV (corresponding photon energy $\Omega = 42$ eV). The origin of this Cooper minimum can be related to the zero crossing of the d-wave component $\langle u_{k2}|r|u_i\rangle$. Across the Cooper minimum the dipole phase of Ar has a significant jump while the phase of Ne behaves smoothly.

3.2.3 Electron wave packet and central momentum approximation

Consider Eq. (3.15), if the exponential term $e^{-i\varphi(p,t)}$ oscillates as a function of t with a period much shorter than the optical cycle of the laser field, according to Yakovlev *et al.*[118], the streaking spectrogram can be approximated by

$$S(E,\tau) \approx \left| \int_{-\infty}^{\infty} \chi(t-\tau) e^{-i\varphi(p,t)} e^{iEt} dt \right|^2 . \tag{3.28}$$

The function $\chi(t)$ is called the "temporal electron wave packet" which describes the XUV photoionization process and is related to the energy domain wave packet $\tilde{\chi}(E)$ by an inverse

Fourier transform:

$$\chi(t) = \frac{1}{2\pi}\int_0^\infty \tilde{\chi}(E)e^{-iEt}dE. \tag{3.29}$$

First-order perturbation theory of the XUV photoionization predicts that

$$\tilde{\chi}(E) = \tilde{E}_{XUV}(\Omega)d(E), \tag{3.30}$$

in which $\Omega = E + I_p$ is the XUV photon energy. Furthermore, if one assumes $\varphi(p,t)$ depends on p weakly such that the momentum p in $\varphi(p,t)$ can be replaced by p_0, with p_0 being the center of the momentum of photoelectrons, then Eq. (3.28) takes the form

$$S(E,\tau) \approx \left|\int_{-\infty}^{\infty} \chi(t-\tau)G(t)e^{iEt}dt\right|^2, \tag{3.31}$$

with the "gate" function $G(t) = e^{-i\varphi(p_0,t)}$ depending on t only. After taking such "central momentum approximation", Eq. (3.31) fits the mathematical form of the standard FROG equation. Therefore iterative algorithms can be used to simultaneously extract $\chi(t)$ and $G(t)$ from $S(E,\tau)$, such as the principal component generalized projection algorithm (PCGPA)[119] and the least square generalized projection algorithm (LSGPA)[120]. The latter is used in the present work. From $G(t)$, a vector potential $A(t)$ of the IR field can be calculated from Eq. (3.16) provided p_0 is given, then the IR field can be retrieved. If the amplitude and phase of the atomic dipole $d(E)$ are well known, the XUV pulse $E_{XUV}(t)$ can be deduced from the extracted wave packet $\tilde{\chi}(E)$ according to Eq. (3.30). These methods are usually called FROG-CRAB[47] in general.

Moreover, note that the FROG-CRAB method cannot determine the absolute time t. In other words, the output of the FROG-CRAB could be $\chi(t-t_0)$ and $G(t-t_0)$ where t_0 is arbitrary. Equivalently, such uncertainty would add a linear term Ωt_0 to the spectral phase $\arg\tilde{\chi}(\Omega)$.

3.3 Simulations and results

3.3.1 SFA simulations for high energy photoelectrons

Figure 3.2 gives two examples of characterizing IAPs from Ne spectrograms that come from SFA simulation using Eq. (3.15). The two IAPs share the same $U(\Omega)$ with $\Omega_0 = 60$ eV and $\Delta\Omega = 23$ eV, but have different $\Phi(\Omega)$. The first IAP is TL which has a duration of 80 as while the second IAP has an attochirp such that its duration is increased to 130 as. The IR field in these simulations is 800 nm in wavelength, cosine-squared envelope, 8.8 fs in FWHM duration and 10^{13} W/cm^2 in peak intensity. Figures 3.2(a) and (b) demonstrate clearly that the streaking spectrogram is sensitive to the XUV spectral phase. Then by using the LSGPA FROG-CRAB we can retrieve the spectral amplitude and phase as well as the temporal profile of the two input IAPs successfully. The comparison between the input and retrieved pulses are given in Figs. 3.2(c),(d) and (e). In the IAP characterization we have divided the output of FROG-CRAB $\tilde{\chi}(E)$ by the known atomic dipole $d(E)$ of Ne. According to Eq.(3.30), $\tilde{E}_{XUV}(\Omega) = \tilde{\chi}(E)/d(E)$. Additionally, to get rid of the uncertainty of the absolute time in the FROG output, we have moved the peak of all IAPs to $t = 0$, and their $\Phi(\Omega)$ have been readjusted by adding a linear term consistently.

3.3.2 TDSE simulations for low energy photoelectrons

In Fig. 3.2, the electron spectrogram was obtained using the SFA theory, thus the retrieved results support that the FROG-CRAB method works accurately in spite of the central momentum approximation and the iterative method. The SFA is expected to work better for high-energy photoelectrons which was the case for Fig. 3.2. At lower photoelectron energies (or photon energies) the SFA model is known to be inaccurate for describing the electron spectra. As a test, FROG-CRAB is used to retrieve IAPs from streaking spectrograms obtained by solving SAE TDSE. The discrete variable representation (DVR) basis set is used in the computation[121, 122], and the one-electron model potential is given in Eq. (3.18).

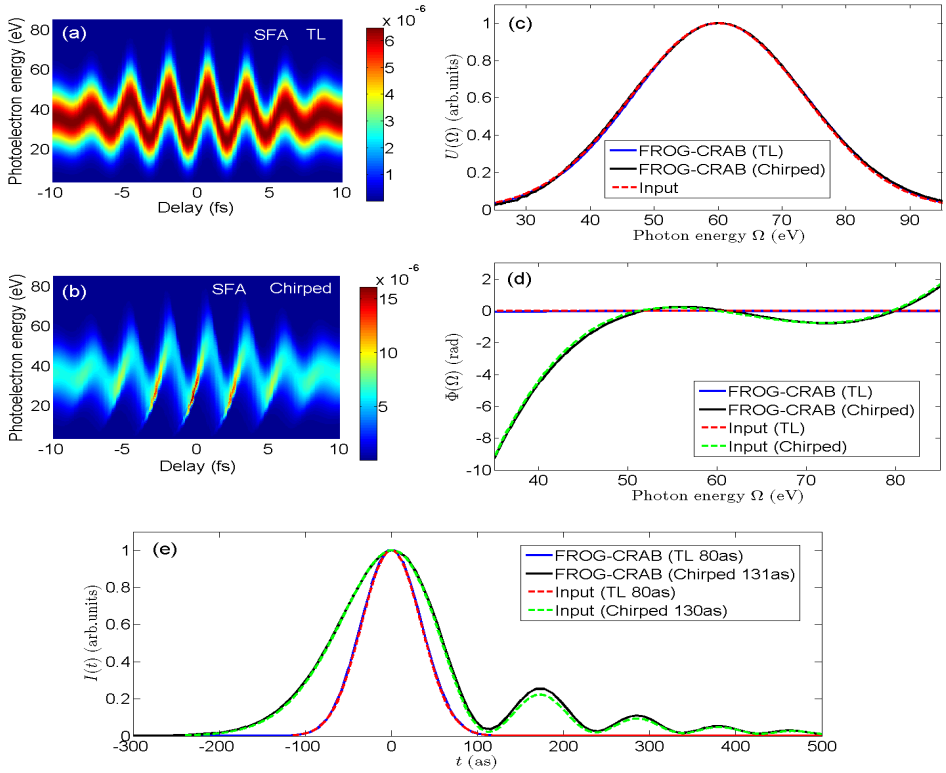

Figure 3.2: *Characterizing IAPs from Ne spectrograms generated using SFA model. The two input IAPs have* $\Omega_0 = 60$ *eV,* $\Delta\Omega = 23$ *eV, 80 as duration for the TL pulse and 130 as duration for the chirped pulse. The IR field is 800 nm in wavelength, 8.8 fs in FWHM duration and* 10^{13} W/cm^2 *in peak intensity. (a) SFA spectrogram for the TL pulse. (b) SFA spectrogram for the chirped pulse. Comparison of input XUV pulses with the retrieved ones: (c) Spectral amplitude (d) spectral phase (e) temporal profile of the input IAPs (dashed lines) and FROG-CRAB retrieved IAPs (solid lines).*

In Fig. 3.3 the IAPs have $\Omega_0 = 40$ eV, $\Delta\Omega = 11.5$ eV and the target is Ne. In Fig. 3.4 the IAPs have even lower photon energy $\Omega_0 = 22$ eV, $\Delta\Omega = 5.9$ eV and the target is Kr. Figures 3.3(a) and (b) give the comparison between TDSE and SFA spectrograms and therefore show the effect of electron-ion interaction for photoelectrons below 30 eV. Fig 3.3(c) shows $U(\Omega)$ can still be accurately retrieved by FROG-CRAB. However the retrieved spectral phase $\Phi(\Omega)$ has a greater chirp than the input one for both the TL and chirped IAPs, as shown in Fig 3.3(d). Due to the overestimation of attochirp, the retrieved pulse duration becomes 165 as compared to the input 160 as for the TL pulse, and 225 as compared to the input 210 as for the chirped pulse. Similarly, for the cases using $\Omega_0 = 22$ eV IAPs, the FROG-CRAB retrieved pulses have longer durations than the input ones. Figure 3.4 (b) shows the comparison between the input and retrieved spectral phase. The results about IAP temporal profile are given in Fig. 3.4 (c). In conclusion, due to the inaccuracy of the SFA model in the low energy region, errors become larger when FROG-CRAB is applied to low-energy electron spectrograms. Up to 10% errors in pulse duration will be introduced if one uses FROG-CRAB to characterize IAPs with photon energies below 40 eV. Since most of the errors occur at the wings of the pulse which have weaker intensity, the error may not be too severe.

3.3.3 Retrieval of IR field

The FROG-CRAB can also extract the IR field as mentioned before. For the TL spectrogram Fig. 3.2(a), we show the comparison between the input $E_{IR}(t)$ and the one coming from FROG-CRAB output in Fig. 3.5. Although the FROG-CRAB result appears to be in good agreement with the input IR in Fig. 3.5(a), the agreement on the attosecond time scale shows its deficiency, according to the zoom-in plot Fig. 3.5(b) where the IR peak position was off by more than 100 as. Here we can compare IR peak positions because $t = 0$ has been determined by the IAP. To improve the accuracy of IR retrieval, we applied a fitting approach based on the known $d(E)$ and the extracted $E_{XUV}(t)$. The IR field were modeled

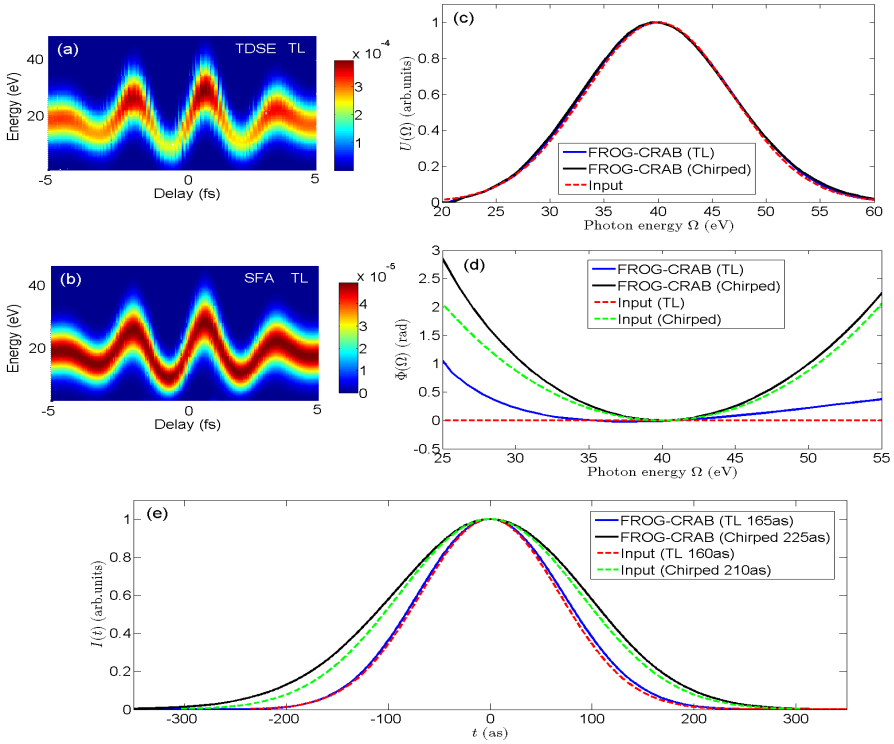

Figure 3.3: *Characterizing IAPs from Ne spectrograms obtained by solving TDSE. The two input IAPs have* $\Omega_0 = 40$ *eV,* $\Delta\Omega = 11.5$ *eV, 160 as duration for the TL pulse and 210 as duration for the chirped pulse. The IR field is 800 nm in wavelength, 4.4 fs in FWHM duration and* 10^{13} W/cm^2 *in peak intensity. (a) TDSE spectrogram for the TL pulse. (b) SFA spectrogram for the TL pulse in comparison. (c) Spectral amplitude (d) spectral phase (e) temporal profile of the input IAPs (dashed lines) and FROG-CRAB retrieved IAPs (solid lines).*

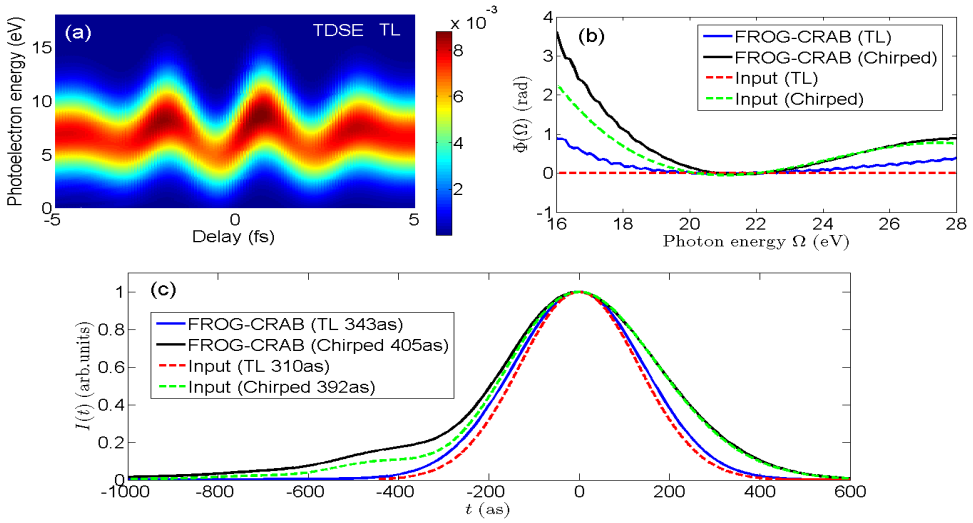

Figure 3.4: *Characterizing IAPs from Kr spectrograms obtained by solving TDSE. The two input IAPs have $\Omega_0 = 22$ eV, $\Delta\Omega = 5.9$ eV, 310 as duration for the TL pulse and 392 as duration for the chirped pulse. The IR field is 800 nm in wavelength, 4.4 fs in FWHM duration and 10^{12} W/cm^2 in peak intensity. (a) TDSE spectrogram for the TL pulse. (b) Spectral phase (c) temporal profile of the input IAPs (dashed lines) and FROG-CRAB retrieved IAPs (solid lines).*

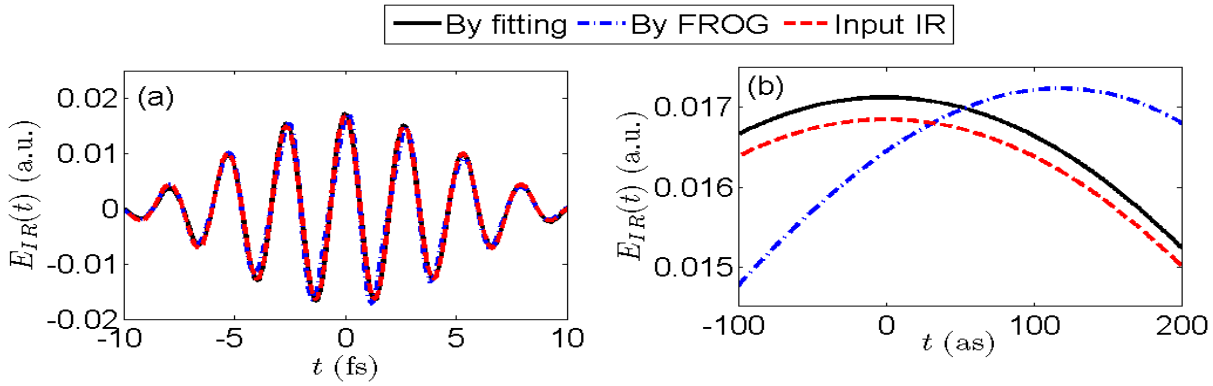

Figure 3.5: *Retrieved IR field from the Ne spectrogram Fig. 3.2(a) with a TL IAP. (a) (Solid black line): The retrieved IR through GA fitting. (Dot-dashed blue line): The output IR field from the FROG-CRAB by setting $p_0 = 1.68$. (Dashed red line): The input IR field. (b) A zoom-in plot of (a) near $t = 0$. From [123].*

by

$$E_{IR}(t) = f(t)\cos[\omega_L(t-\Delta)]. \tag{3.32}$$

The envelope $f(t)$ was constructed by a set of samples (t_i, f_i) through cubic-spline interpolation. The horizontal coordinates t_i were fixed while the vertical coordinates f_i as well as Δ were set as fitting parameters. Then we used Eq. (3.15) to generate trial spectrograms and applied the Genetic algorithm (GA) to find the optimal parameters by minimizing the error between the input and the trial spectrograms. In Fig. 3.5(b) the peak of the IR field extracted via fitting is off by only about 2 as, which is the benefit of including the additional fitting procedure. Note that the fitting approach is based on the SFA equation directly, therefore, it does not apply the central momentum approximation that limits the performance of FROG-CRAB.

3.4 Summary

In this chapter we check the accuracy of FROG-CRAB on pulse retrieval by simulating the spectrogram using known input XUV and IR pulses. For high-energy electrons where the photon energy of the IAP is centered at 60 eV, SFA is supposed to be accurate enough to describe the spectrogram. By applying FROG-CRAB to the SFA-simulated spectrograms, both the TL and chirped input IAP can be successfully retrieved. These examples show that FROG-CRAB works accurately in spite of the central momentum approximation and the iterative method. However, it was demonstrated that the central momentum approximation will break down when the IAP bandwidth is quite comparable to the central energy of photoelectrons[48]. For low-energy electrons, SFA is not accurate any more to calculate the spectrograms. TDSE is solved numerically instead of SFA to generate the spectrograms. The retrieved IAPs via FROG-CRAB contain up to 10% errors in pulse duration compared with the input pulses. These results show that the IAP extracted via FROG-CRAB is still acceptable although the spectrogram calculated from SFA does not reproduce the spectro-

gram calculated using TDSE. For the IR pulse retrieval, the IR extracted by FROG-CRAB is good in femtosecond time scale but not in attosecond time scale. The accuracy can be improved by a fitting method without the central momentum approximation.

Chapter 4

Characterization of isolated attosecond pulses with PROOF

The FROG-CRAB is limited by the SFA and the central momentum approximations on which this method is based. To overcome such limitations another pulse retrieve method called PROOF was proposed[48]. This method is actually based on second-order perturbation theory instead of SFA model, so it would be more accurate from theoretical point of view so long as the IR intensity is within the perturbative regime. However, the original derivation of PROOF in Ref. [48] is quite primitive such that it totally ignores the atomic transition dipoles in the photoionization process. In this chapter we give a systematic derivation of the PROOF method based on the second-order perturbation theory including the accurate two-photon transition matrix elements. We refer the PROOF method that derived from perturbation theory without any further approximations as the "scattering wave PROOF (swPROOF)" compared with the original PROOF given in Ref. [48]. Furthermore, we compare the accuracy of the swPROOF and the original PROOF in characterizing IAPs, which can serve as a benchmark of accurate spectral phase retrieval. The materials in this chapter are adapted from the publication [124].

Section 4.1.1 is the formulation of the streaking spectrogram based on second-order

perturbation theory. From the derivations we introduce the first-second-order interference (FSI) term which plays an important role in spectral phase retrieval. Second-order perturbation theory includes the two-photon transition dipole matrix element, so in Section 4.1.2 we mention how to accurately calculate this quantity. In Section 4.1.3 we introduce additional approximations and recover the original PROOF method. Then we solve TDSE numerically to calculate photoelectron spectrograms and use them as the input of pulse retrieval. In Section 4.2.1 we compare the FSI term extracted from the TDSE spectrogram with the one computed from analytical equations corresponding to swPROOF and PROOF. The difference between simulation and theory implies the accuracy of such phase retrieval method. The main results are presented in Section 4.2.2, where we compare the spectral phase and temporal intensity profile of the input IAP and the retrieved ones via swPROOF and PROOF. The effect of IR intensity on pulse retrieval is discussed in Section 4.2.3. Finally we conclude this chapter in Section 4.3.

4.1 Formulations of the PROOF method

4.1.1 First-second-order interference term in photoelectron spectra

Assume the IR intensity is weak so that we can neglect the ionization path that involves more than one IR photon. Therefore second-order perturbation theory can be applied to model the streaking spectrogram, as in the RABITT method for APT characterization. However in RABITT case the sideband cannot be directly reached by the XUV but results from interference between two XUV+IR paths, while the direct XUV ionization must be included in the characterization of IAP. Consider photoelectrons measured along the polarization axis of the XUV and IR (chosen to be the $+z$ direction), and we model the IR field as monochromatic which is an approximation of a multi-cycle field that has a slowly varying

envelope. The streaking spectrogram can be modeled by

$$S(E,\tau) = \left|\tilde{E}_{XUV}(\Omega)d(E) + \tilde{E}_{XUV}(\Omega-\omega)\frac{E_{IR}}{2}e^{-i\omega\tau}d^{(+)}(E) + \tilde{E}_{XUV}(\Omega+\omega)\frac{E_{IR}}{2}e^{i\omega\tau}d^{(-)}(E) + o(E_{IR}^2)\right|^2. \quad (4.1)$$

Here $E = k^2/2$ is the photoelectron energy, $\Omega = E + I_p$ is the XUV photon energy, ω is the IR frequency, E_{IR} is the IR field strength. $\tilde{E}_{XUV}(\Omega)$ is the XUV field in the frequency domain, as discussed in Section 3.1. τ is the temporal shift between the XUV and IR fields. A positive τ means the XUV comes after the peak of the IR field.

The first term in the right-hand-side of Eq. (4.1) describes the process that the electron initially at ground state absorbs one XUV photon Ω and transits to continuum state with energy E. The second term corresponds to the path that the electron first absorbs one XUV photon $\Omega - \omega$ and then absorbs one IR photon ω, while the third term corresponds to the path that the electron first absorbs one XUV photon $\Omega+\omega$ and then emits one IR photon ω. The term $o(E_{IR}^2)$ includes contributions from higher order paths involving two or more IR photons. The total spectrogram is the modulus square of the coherent superposition of all possible quantum paths that lead to a final state with energy E. Since $\omega \ll I_p$ for noble gas atoms, contribution from the path that the electron first absorbs (or emits) one IR photon and then one XUV photon is negligible[125]. Therefore in the present work we only include paths that the electron absorbs one XUV photon first.

The single photon transition dipole $d(E) = \langle k\mathbf{e}_z|z|i\rangle$ has been given in Eq. (3.25) if a one-electron model potential is used. The XUV+IR two-photon transition dipole matrix element $d^{(\pm)}(E)$ is given by

$$d^{(\pm)}(E) = \lim_{\epsilon\to 0}\sum_{\alpha\lambda m}\frac{\langle k\mathbf{e}_z|z|\alpha\lambda m\rangle\langle\alpha\lambda m|z|i\rangle}{E_{\mp} - E_\alpha + i\epsilon}. \quad (4.2)$$

Here $d^{(+)}$ corresponds to the path that absorbs one IR photon, and $d^{(-)}$ to the path that

emits one IR photon. $E_{\mp} = E \mp \omega$ are the energies of the virtual intermediate states. The summation in Eq. (4.2) includes all the eigenstates $|\alpha\lambda m\rangle$ of the field-free Hamiltonian in spherical coordinates, both bound and continuum. Since $E_{\mp}$ falls in the continuum spectrum additional treatments when E_α is close to $E_{\mp}$ are needed. We will show the details of evaluating the two-photon transition dipole in the next subsection.

Back to Eq. (4.1), we can expand it by the order of E_{IR}:

$$S(E,\tau) = S_{XUV}(E) + S_{FSI}(E,\tau) + o(E_{IR}^2). \tag{4.3}$$

Here, $S_{XUV}(E) = |U(\Omega)|^2|d(E)|^2$ is the IR-free XUV-only photoelectron spectrum which contains no phase information. What we are interested in is the FSI term which is proportional to E_{IR}:

$$\begin{aligned} S_{FSI}(E,\tau) &= E_{IR}\mathrm{Re}\Big\{\tilde{E}_{XUV}(\Omega)\tilde{E}^*_{XUV}(\Omega-\omega)e^{i\omega\tau}d(E)d^{(+)*}(E) \\ &\quad +\tilde{E}_{XUV}(\Omega)\tilde{E}^*_{XUV}(\Omega+\omega)e^{-i\omega\tau}d(E)d^{(-)*}(E)\Big\} \\ &= E_{IR}U(\Omega)|d(E)|\left\{U(\Omega-\omega)|d^{(+)}(E)|\cos(\omega\tau+\Delta_+(E))\right. \\ &\quad \left.+U(\Omega+\omega)|d^{(-)}(E)|\cos(\omega\tau+\Delta_-(E))\right\} \end{aligned} \tag{4.4}$$

The phases Δ_+ and Δ_- depend on the spectral phase $\Phi(\Omega)$ and the phase of dipole matrix elements:

$$\Delta_+(E) = \Phi(\Omega) - \Phi(\Omega-\omega) + \arg[d(E)] - \arg[d^{(+)}(E)], \tag{4.5}$$

$$\Delta_-(E) = \Phi(\Omega+\omega) - \Phi(\Omega) - \arg[d(E)] + \arg[d^{(-)}(E)]. \tag{4.6}$$

Equation (4.4) implies that the FSI term is a superposition of two oscillating terms: one comes from the interference between the direct and the IR-absorption path, the other comes from the interference between the direct and the IR-emission path. For a given electron energy E the FSI term oscillates as a function of τ at the IR frequency ω. Equation (4.4)

can be rewritten as

$$S_{FSI}(E,\tau) = A(E)\cos(\omega\tau + \Psi(E)), \tag{4.7}$$

with the amplitude $A(E)$ and phase $\Psi(E)$ given by

$$\begin{aligned} A(E) = E_{IR}U(\Omega)|d(E)| \big\{ &|U(\Omega-\omega)|^2|d^{(+)}(E)|^2 + |U(\Omega+\omega)|^2|d^{(-)}(E)|^2 \\ &+2U(\Omega-\omega)U(\Omega+\omega)|d^{(+)}(E)||d^{(-)}(E)|\cos(\Delta_+(E)-\Delta_-(E))\big\}^{1/2}, \end{aligned} \tag{4.8}$$

$$\Psi(E) = \tan^{-1}\left(\frac{U(\Omega-\omega)|d^{(+)}(E)|\sin\Delta_+(E) + U(\Omega+\omega)|d^{(-)}(E)|\sin\Delta_-(E)}{U(\Omega-\omega)|d^{(+)}(E)|\cos\Delta_+(E) + U(\Omega+\omega)|d^{(-)}(E)|\cos\Delta_-(E)}\right). \tag{4.9}$$

In practice, one cannot decompose the experimental spectrogram into perturbation series by the order of E_{IR}. Instead, one can apply Fourier analysis to separate different oscillating frequency components

$$S(E,\tau) = S_0(E) + S_\omega(E,\tau) + S_{2\omega}(E,\tau) + \dots. \tag{4.10}$$

Here $S_0(E) = S_{XUV} + o(E_{IR}^2)$ is a D.C. term that is independent of τ, $S_\omega(E,\tau) = S_{FSI}(E,\tau) + o(E_{IR}^3)$ oscillates with τ at the frequency ω, and $S_{2\omega}(E,\tau) \sim o(E_{IR}^2)$ oscillates with τ at the frequency 2ω. When the IR intensity is weak, $S_0 \approx S_{XUV}$, $S_\omega \approx S_{FSI}$, and high frequency components are negligible. Therefore the FSI term can be obtained by applying a filter on the measured spectrogram and then selecting its omega component. Suppose the spectral magnitude $U(\Omega)$ and the transition matrix elements $d(E)$, $d^{(+)}(E)$ and $d^{(-)}(E)$ are already known, the spectral phase can be retrieved by fitting the FSI amplitude $A(E)$ and phase $\Psi(E)$ according to Eqs. (4.8) and (4.9). This procedure forms the basis of the PROOF (phase retrieval by omega oscillation filtering) method[48]. Note that in the case of IAP, $S_{2\omega}$ is due to the interference not only between the two XUV+IR paths (absorbing or emitting one IR photon respectively) as in the RABITT case, but also between the direct (XUV-only) path and the XUV+IR+IR path (absorbing or emitting two IR photons). In either case there is a contribution proportional to E_{IR}^2.

4.1.2 Two-photon transition dipole matrix elements

To evaluate the two photon transition dipole $d^{(\pm)}(E)$, one needs to expand the final continuum state into partial waves according to Eq. (3.24), then separate Eq. (4.2) by radial and angular parts, that is

$$d^{(\pm)}(E) = \sum_{L,\lambda} \sqrt{\frac{2L+1}{4\pi}} e^{i\eta_L(E)} \langle Y_{L0}| \cos\theta |Y_{\lambda 0}\rangle \langle Y_{\lambda 0}| \cos\theta |Y_{l_i 0}\rangle W_{L,\lambda}(E, E_{\mp}). \tag{4.11}$$

Here the initial state has a well-defined angular momentum number l_i, λ and L are the angular momentum quantum numbers of the intermediate and the final partial wave of the photoelectron, respectively. According to the dipole selection rule, $\lambda = l_i \pm 1$, $L = \lambda \pm 1$. The term $W_{L,\lambda}$ is a two-photon radial matrix element:

$$W_{L,\lambda}(E, E_{\mp}) = \lim_{\epsilon \to 0} \sum_{E_\alpha} \frac{\langle u_{kL}|r|u_{E_\alpha \lambda}\rangle \langle u_{E_\alpha \lambda}|r|u_i\rangle}{E_{\mp} - E_\alpha + i\epsilon}. \tag{4.12}$$

$u_{kL}(r)$ is the energy normalized radial wave function with angular momentum quantum number L and $\eta_L(E)$ is the corresponding phase shift, see Eqs. (3.21) and (3.22).

For example, if the ground state has s-symmetry ($l_i = 0$), the two-photon dipole consists of two paths $s \to p \to s$ and $s \to p \to d$:

$$d^{(\pm)}(E) = \sqrt{\frac{1}{36\pi}} \{e^{i\eta_0(E)} W_{0,1}(E, E_{\mp}) + 2e^{i\eta_2(E)} W_{2,1}(E, E_{\mp})\}. \tag{4.13}$$

On the other hand, if the ground state has p-symmetry ($l_i = 1$), the two-photon dipole consists of three paths $p \to s \to p$, $p \to d \to p$ and $p \to d \to f$:

$$d^{(\pm)}(E) = \sqrt{\frac{1}{12\pi}} \{e^{i\eta_1(E)} W_{1,0}(E, E_{\mp}) + \frac{4}{5} e^{i\eta_1(E)} W_{1,2}(E, E_{\mp}) + \frac{6}{5} e^{i\eta_3(E)} W_{3,2}(E, E_{\mp})\}. \tag{4.14}$$

The radial matrix element $W_{L,\lambda}$ in Eq. (4.12) is an infinite sum which is hard to evaluate

directly. Instead, we introduce the radial Hamiltonian

$$H_\lambda = -\frac{1}{2}\frac{d^2}{dr^2} + V(r) + \frac{\lambda(\lambda+1)}{2r^2}, \tag{4.15}$$

and the intermediate radial wave function $\rho_{\kappa_\mp\lambda}(r)$ such that

$$W_{L,\lambda}(E, E_\mp) = \langle u_{kL}|r|\rho_{\kappa_\mp\lambda}\rangle, \tag{4.16}$$

where $\kappa_\mp = \sqrt{2E_\mp}$. $\rho_{\kappa_\mp\lambda}$ describes the photoelectron after absorbing one XUV photon, and can be found in the following way:

$$\begin{aligned}\rho_{\kappa_\mp\lambda}(r) &= (\lim_{\epsilon\to 0}\sum_{E_\alpha}\frac{|u_{E_\alpha\lambda}\rangle\langle u_{E_\alpha\lambda}|}{E_\mp - E_\alpha + i\epsilon})ru_i(r) = (\lim_{\epsilon\to 0}\frac{1}{E_\mp - H_\lambda + i\epsilon})ru_i(r) \\ &= (\wp\frac{1}{E_\mp - H_\lambda} - i\pi\delta(E_\mp - H_\lambda))ru_i(r) = \rho^{(R)}_{\kappa_\mp\lambda} - i\pi\langle u_{\kappa_\mp\lambda}|r|u_i\rangle u_{\kappa_\mp\lambda}(r). \end{aligned}\tag{4.17}$$

The term with $\wp$ prescribes the principal value integration that contributes to the real part of $\rho_{\kappa_\mp\lambda}$ (off-shell part). The δ term represents the Dirac delta function that contributes to the imaginary part of $\rho_{\kappa_\mp\lambda}$ (on-shell part). The function $\rho^{(R)}_{\kappa_\mp\lambda}(r)$ is the solution of the Dalgarno-Lewis differential equation:

$$(E_\mp - H_\lambda)\rho^{(R)}_{\kappa_\mp\lambda}(r) = ru_i(r), \tag{4.18}$$

with the boundary condition $\rho^{(R)}_{\kappa_\mp\lambda}(r) = 0$ at $r = 0$. Physical solution of $\rho_{\kappa_\mp\lambda}(r)$ requires the asymptotic behavior[126, 127]

$$\lim_{r\to\infty}\rho_{\kappa_\mp\lambda}(r) = -\pi\sqrt{\frac{2}{\pi\kappa_\mp}}e^{i\left(\kappa_\mp r + \frac{Z_c}{\kappa_\mp}\ln(2\kappa_\mp r) + \eta_\lambda(E_\mp)\right)}\langle u_{\kappa_\mp\lambda}|r|u_i\rangle. \tag{4.19}$$

In order to fulfill the asymptotic form Eq. (4.19), the physical solution of Eq. (4.18) should have the smallest asymptotic amplitude[128]. This way to evaluate $W_{L,\lambda}$ is called Dalgarno-

Lewis method.

4.1.3 Approximations used in the original PROOF method

If $W_{L,\lambda}$ is calculated exactly with the Dalgarno-Lewis method, one can obtain the exact two-photon transition dipoles. Alternatively, if one uses the asymptotic form of $\rho_{\kappa_\mp\lambda}$ and u_{kL}, Eqs. (4.19) and (3.21), to evaluate $W_{L,\lambda}$, the approximate result takes the form

$$W_{L,\lambda}(E, E_\mp) \approx ie^{i\{\eta_\lambda(E_\mp)-\eta_L(E)\}}\langle u_{\kappa_\mp\lambda}|r|u_i\rangle T^{cc}(E, E_\mp). \tag{4.20}$$

The term T^{cc} has an analytical form

$$T^{cc}(E, E_\mp) = -\frac{1}{\sqrt{k\kappa_\mp}}\frac{(2\kappa_\mp)^{iZ_c/\kappa_\mp}}{(2k)^{iZ_c/k}}\left(\frac{i}{\kappa_\mp - k}\right)^{2+i(Z_c/\kappa_\mp - Z_c/k)}\Gamma[2 + i(Z_c/\kappa_\mp - Z_c/k)]. \tag{4.21}$$

Note that this expression does not depend on the target except for the asymptotic charge Z_c but it does depend on the photoelectron energy. Plugging Eq. (4.20) into Eq. (4.11) we can obtain the approximate two-photon dipole

$$d^{(\pm)}(E) \approx iT^{cc}(E, E_\mp)\sum_{L,\lambda}\sqrt{\frac{2L+1}{4\pi}}e^{i\eta_\lambda(E_\mp)}\langle u_{\kappa_\mp\lambda}|r|u_i\rangle\langle Y_{L0}|\cos\theta|Y_{\lambda 0}\rangle\langle Y_{\lambda 0}|\cos\theta|Y_{l_i 0}\rangle. \tag{4.22}$$

By applying dipole selection rules and working out the angular part, one can prove that

$$d^{(\pm)}(E) \approx iT^{cc}(E, E_\mp)d(E_\mp). \tag{4.23}$$

Here $d(E_\mp)$ is the single photon transition dipole matrix element to the continuum state with energy $E_\mp$. Equation (4.23) implies that the two-photon dipole can be approximately separated into two parts: the single photon transition dipole to the intermediate state and a term T^{cc} accounting for the IR induced continuum-continuum (C-C) transition.

Furthermore, if we set $Z_c = 0$ in Eq. (4.21) to turn off the long-range Coulomb potential

which is consistent with the SFA, then

$$T^{cc}(E, E_{\mp}) \approx \frac{1}{\sqrt{k\kappa_{\mp}}} \frac{1}{(\kappa_{\mp} - k)^2}. \tag{4.24}$$

Next we take the soft photon approximation[129, 130], that is to assume $\omega << E$, then

$$\kappa_{\mp} = \sqrt{2(E \mp \omega)} = k\sqrt{1 \mp \frac{\omega}{E}} \approx k(1 \mp \frac{\omega}{2E}) = k \mp \frac{\omega}{k}, \tag{4.25}$$

and therefore

$$T^{cc}(E, E_{\mp}) \approx \frac{1}{\sqrt{k^2 \mp \omega}} \frac{1}{(\mp\frac{\omega}{k})^2} \approx \frac{k}{\omega^2}. \tag{4.26}$$

Moreover, we may neglect the atomic term $d(E)$ in the photoionization process since the goal here is to characterize IAPs. The transition dipoles are approximated by:

$$d(E) \approx D, \tag{4.27}$$

$$d^{(\pm)}(E) \approx i\frac{k}{\omega^2} D, \tag{4.28}$$

where D is a real constant independent of energy. Using approximations Eqs. (4.27) and (4.28), we can rewrite Eqs. (4.8) and (4.9) as

$$\begin{aligned} A(E) &= E_{IR}\frac{kD^2}{\omega^2} U(\Omega) \left\{ |U(\Omega - \omega)|^2 + |U(\Omega + \omega)|^2 \right. \\ &\quad \left. + 2U(\Omega - \omega)U(\Omega + \omega)\cos(\Delta_+(E) - \Delta_-(E)) \right\}^{1/2}, \end{aligned} \tag{4.29}$$

$$\Psi(E) = \tan^{-1}\left(\frac{U(\Omega - \omega)\sin\Delta_+(E) + U(\Omega + \omega)\sin\Delta_-(E)}{U(\Omega - \omega)\cos\Delta_+(E) + U(\Omega + \omega)\cos\Delta_-(E)} \right), \tag{4.30}$$

and the phase $\Delta_{\pm}$ now becomes

$$\Delta_+(E) = \Phi(\Omega) - \Phi(\Omega - \omega) - \frac{\pi}{2}, \tag{4.31}$$

$$\Delta_-(E) = \Phi(\Omega+\omega) - \Phi(\Omega) + \frac{\pi}{2}. \tag{4.32}$$

Equations (4.29) to (4.32) form the basis of the original PROOF method proposed by Chini *et al.*[48]. If one uses the approximation Eq. (4.23) but without Eqs. (4.27) and (4.28), the method is named by "iPROOF"[131]. Consequently, we refer the method using the accurate transition dipole matrix elements as the swPROOF[124]. For simplicity, we only consider the swPROOF and the original PROOF methods in the following discussion.

Comparing Eqs. (4.5), (4.6) and (4.31), (4.32), we can define the atomic phase $\psi_\pm(E)$ such that

$$\Delta_+(E) = \Phi(\Omega) - \Phi(\Omega-\omega) + \psi_+(E) - \frac{\pi}{2}, \tag{4.33}$$

$$\Delta_-(E) = \Phi(\Omega+\omega) - \Phi(\Omega) + \psi_-(E) + \frac{\pi}{2}. \tag{4.34}$$

Obviously $\psi_\pm(E) = 0$ in the case of original PROOF. For swPROOF, the exact atomic phase is given by

$$\psi_+(E) = \arg[d(E)] - \arg[d^{(+)}(E)] + \frac{\pi}{2}, \tag{4.35}$$

$$\psi_-(E) = \arg[d^{(-)}(E)] - \arg[d(E)] - \frac{\pi}{2}. \tag{4.36}$$

We have calculated the exact dipole matrix elements for Ar target at $\omega = 1.55$ eV. Figure 4.1 plots the amplitude of the exact single and two photon transition dipoles, as well as the approximated values corresponding to original PROOF. Here we choose $D = 0.06$ to minimize the difference between swPROOF and PROOF. Clearly the error of the PROOF method mainly lies in low energy regions of $E < 40$ eV.

Figure 4.2 shows the exact atomic phase $\psi_+(E)$ and $\psi_-(E)$ for the swPROOF method. They are all negative and quite close to each other. Each phase has a sharp valley near the Cooper minimum. For the energy region $E > 40$ eV, $|\psi_\pm(E)| < 0.02\pi$ so it would be reasonable to neglect the atomic phase as PROOF does. From Eqs. (4.33) and (4.34) one can deduce that as long as ω is small and the spectral phase $\Phi(\Omega)$ changes smoothly over a broad frequency range, Δ_+ and Δ_- roughly differ by π. Then the two interference terms in

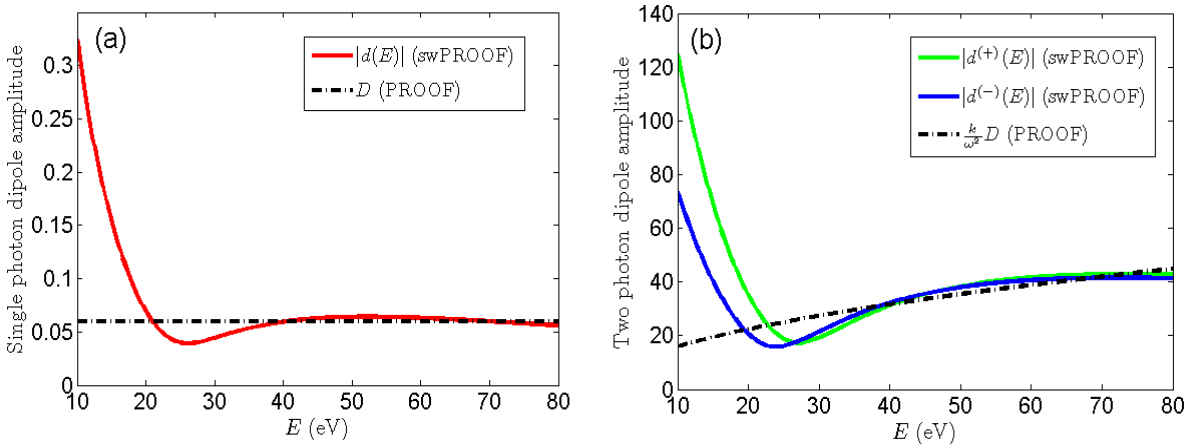

Figure 4.1: *Amplitude of the (a) Single photon and (b) two photon transition dipole matrix elements for Ar target. Solid lines are the exact quantities used in swPROOF, while dash-dotted lines are the approximated quantities in PROOF. The IR photon energy* $\omega = 1.55$ *eV.*

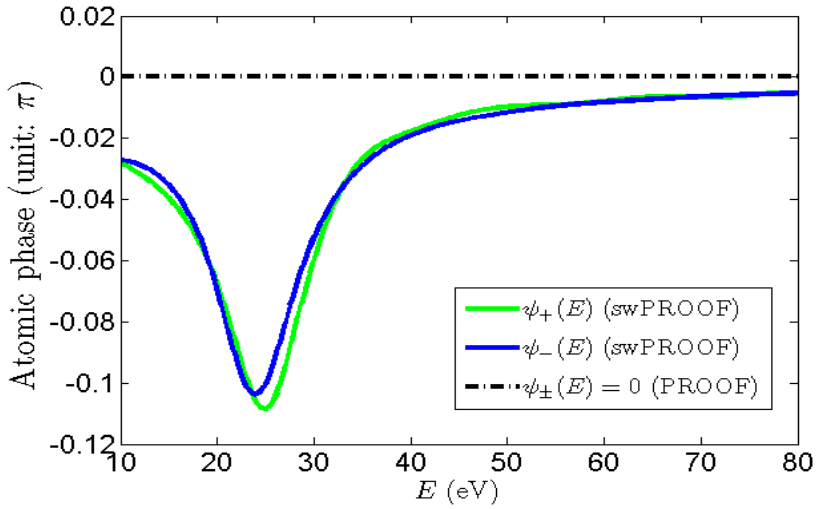

Figure 4.2: *The atomic phase* $\psi_\pm$ *for both swPROOF and PROOF methods.*

Eq. (4.4) tend to be out of phase, and the FSI term is actually a result of strong cancelation between these two oscillating terms.

4.2 Simulations and results

4.2.1 Comparison of FSI terms between TDSE and the theory

We simulate the XUV+IR spectra for argon by solving the single active electron TDSE numerically. An 800 nm IR pulse with peak intensity 10^{11} W/cm^2 is used in this simulation which mimics the typical experimental condition. To reduce the computational load we limit ourselves to a relative short IR pulse (8.8 fs in FWHM) with a cosine-squared envelope. The box size and number of grid points were chosen to ensure convergence. Figure 4.3(a),(b) and (c) shows the spectral amplitude, phase and temporal intensity profile of an XUV pulse used in the simulation. The pulse has a Gaussian amplitude with a central frequency of $\Omega_0 = 60$ eV and a bandwidth of $\Delta\Omega = 22$ eV, which would correspond to a FWHM duration of 83 as for a TL pulse. However this pulse has a chirped phase such that in the time domain its real duration is 130 as and its shape is not Gaussian any more. Figure 4.3(d) is the spectrogram generated by this XUV pulse. A positive τ means the XUV comes after the IR pulse.

Figure 4.4 shows the magnitude of the three Fourier components filtered from the spectrogram Fig. 4.3(d). Clearly the D.C. component S_0 is almost identical to the IR-free XUV-only spectra S_{XUV}. Our interest lies in the ω-component S_ω which can be treated as the FSI term. This part varies as the XUV phase changes, however it is about one order of magnitude smaller than the D.C. part. The 2ω-component $S_{2\omega}$ is one order smaller than the FSI term therefore can be neglected.

The FSI amplitude $A(E)$ and phase $\Psi(E)$ (see Eq. (4.7)) can be either extracted from the TDSE spectrogram or calculated from the known $U(\Omega)$, $\Phi(\Omega)$ and relevant matrix elements for the PROOF and swPROOF methods via Eqs. (4.8) and(4.9). Figure 4.5(a) and (b) shows the comparison of such results. $A(E)$ shows a valley and $\Psi(E)$ shows a large phase jump

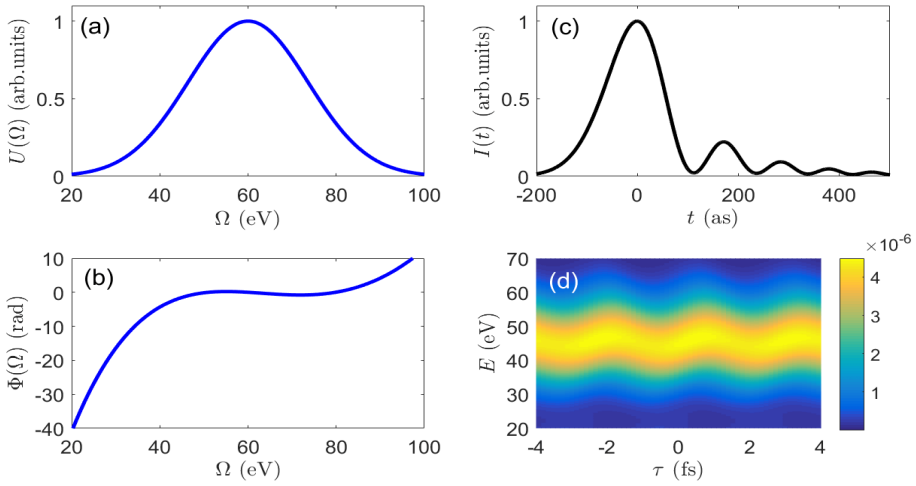

Figure 4.3: *(a) Spectral amplitude (b) spectral phase and (c) intensity profile of the XUV pulse used in the TDSE simulation. (d) the computed spectrogram.*

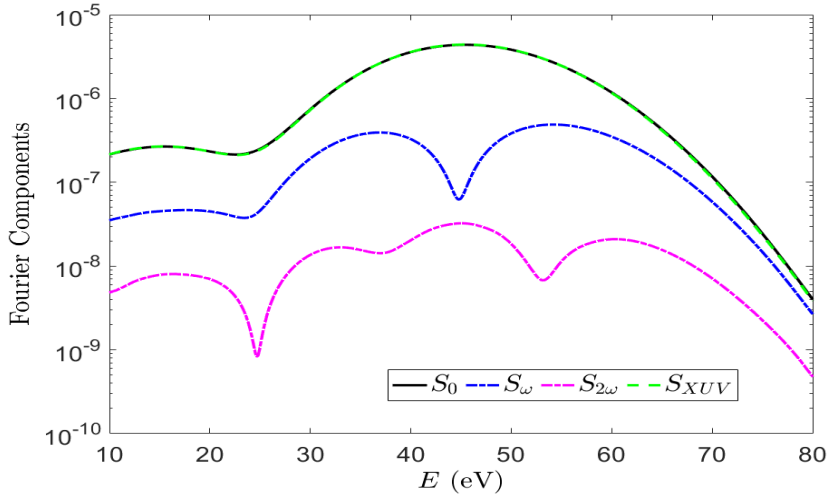

Figure 4.4: *Magnitude of the Fourier component S_0 (top solid line), S_ω (middle dot-dashed line) and $S_{2\omega}$ (bottom dot-dashed line) filtered from Fig. 4.3(d), the TDSE result of the IR-free spectra S_{XUV} (top dashed line) is also plotted.*

around the central energy $E_0 = \Omega_0 - I_p \approx 44$ eV. The overall agreement in $\Psi(E)$ is better than in $A(E)$, and the TDSE result is well reproduced by the swPROOF method where the atomic matrix elements are calculated using the Dalgarno-Lewis method. The remaining discrepancies between swPROOF and TDSE might result from the finite duration of the IR pulse used in the TDSE simulation, as opposed to a monochromatic wave assumed in the theoretical model. On the other hand, $A(E)$ and $\Psi(E)$ given by the PROOF method shows noticeable error, especially in the low energy region, which demonstrates the limitation of the approximation Eqs. (4.27) and (4.28). The quantities $A(E)\cos\Psi(E)$ and $A(E)\sin\Psi(E)$ are also given in Fig. 4.5(c) and (d) respectively. One can see that $A(E)\cos\Psi(E)$ is roughly one fifth of $A(E)\sin\Psi(E)$ in magnitude. Note that $A(E)$ and $\Psi(E)$ are not affected by the CEP of the XUV pulse.

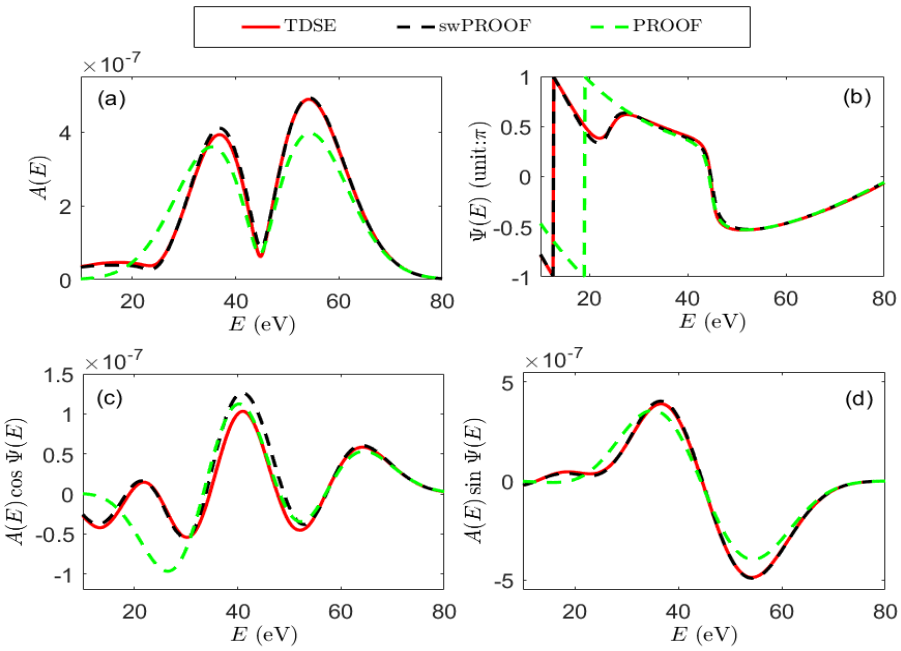

Figure 4.5: *(a) $A(E)$ (b) $\Psi(E)$ (c) $A(E)\cos\Psi(E)$ (d) $A(E)\sin\Psi(E)$ extracted from the TDSE spectrogram Fig. 4.3(d) (red solid line) and calculated from the actual XUV pulse and the atomic matrix elements in swPROOF (black dashed line) and PROOF (green dashed line).*

4.2.2 Accuracy of spectral phase retrieval for IAPs

Except for the XUV pulse shown in Fig. 4.3, three extra pulses were used to generate TDSE spectrograms. All the four pulses (in cases 1-4) have the same spectral amplitude but different phase, resulting in different temporal profiles. The swPROOF and PROOF were applied on these spectrograms to characterize the input IAPs. In order to retrieve $\Phi(\Omega)$ we parametrize it into

$$\Phi_{\text{guess}}(\Omega) = \sum_{n=1}^{4} a_n(\Omega - \Omega_0)^n. \tag{4.37}$$

Here we always set $\Phi_{\text{guess}}(\Omega_0) = 0$ at the central frequency, because the absolute phase cannot be retrieved. From $\Phi_{\text{guess}}(\Omega)$ as well as the known $U(\Omega)$ and atomic matrix elements one can calculate $A_{\text{guess}}(E)$ and $\Psi_{\text{guess}}(E)$ using Eqs. (4.8) and (4.9). The optimal solution is the one which minimizes the error

$$\begin{aligned} Q \;=\; & \int \big\{[A_{\text{TDSE}}(E)\cos\,\Psi_{\text{TDSE}}(E) - A_{\text{guess}}(E)\cos\,\Psi_{\text{guess}}(E)]^2 \\ & +[A_{\text{TDSE}}(E)\sin\,\Psi_{\text{TDSE}}(E) - A_{\text{guess}}(E)\sin\,\Psi_{\text{guess}}(E)]^2\big\}\,dE. \end{aligned} \tag{4.38}$$

This optimization can be done via the genetic algorithm (GA). In the simulation the IR intensity is 10^{11} W/cm^2, but in the retrieval we assume this intensity is unknown. Therefore the coefficients a_n in Eq. (4.37) as well as E_{IR} are chosen as fitting parameters.

The comparison between the input and retrieved spectral phase for the four IAPs is given in Fig. 4.6. The corresponding results for the temporal profile are given in Fig. 4.7 and Table 4.1. We can conclude that the swPROOF is more accurate and robust than PROOF, as expected. Although the pulse duration retrieved by PROOF is acceptable in case 2 and case 4, it has relatively large error for case 1 and case 3. These results provide the benchmark on how accurately the IAP can be characterized in a given experiment for such a highly idealized "experimental" situation. In our simulation even the pulse retrieved by swPROOF may have a small error compared to the actual XUV pulse. This error mainly

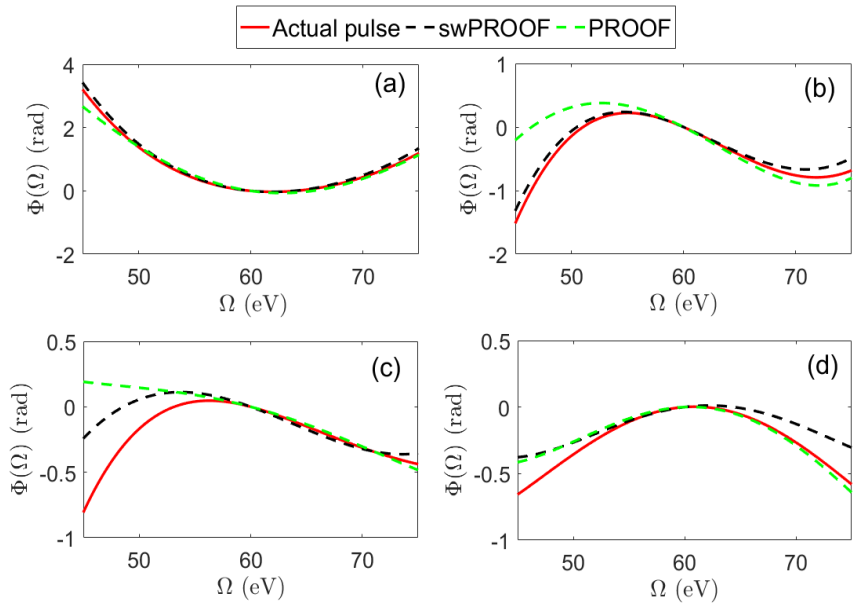

Figure 4.6: *The input and retrieved spectral phase for the four IAPs (case 1-4), shown in (a)-(d) respectively. The IR field used in these simulations is 800 nm in wavelength, 8.8 fs in FWHM duration and* 10^{11} W/cm^2 *in peak intensity.*

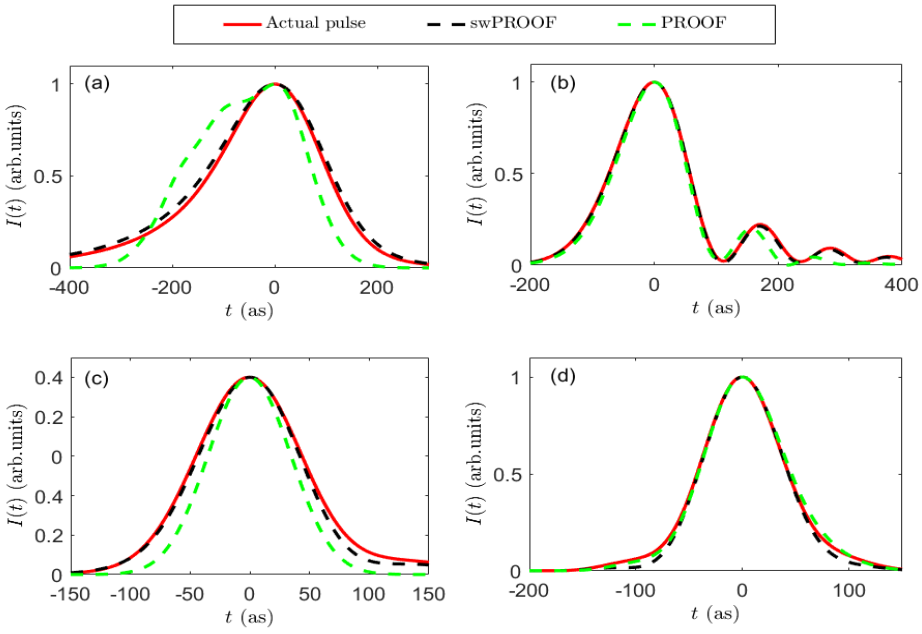

Figure 4.7: *The input and retrieved normalized temporal intensity profile for the four IAPs (case 1-4), shown in (a)-(d) respectively.*

results from the finite-duration IR pulse used in the simulation, and it is believed that this error can be reduced if a longer IR pulse (for example over 20 fs) is used.

Pulse duration (as)	Actual	swPROOF	PROOF
case 1	235	254	270
case 2	130	129	122
case 3	103	100	83
case 4	87	84	88

Table 4.1: *The input and retrieved pulse durations for* 10^{11} W/cm^2 *IR intensity, read from Fig 4.7.*

4.2.3 Effect of the IR intensity on pulse retrieval

As the dressing IR intensity increases, quantum paths involving two or more IR photons will have more contribution to the total spectrogram. Therefore the omega oscillating component S_ω extracted from the spectrogram starts to deviate from the first-second-order interference term S_{FSI} as we discussed in Section 4.1.1. Such deviation will impose larger error on the pulse characterization process. Figure 4.8 and Table 4.2 show the result when the IR intensity used in the simulation was increased to 10^{12} W/cm^2. At this IR intensity the swPROOF method can still retrieve the XUV pulse duration successfully with the error less than 10%. However, Fig. 4.9 and Table 4.3 demonstrate that the swPROOF and PROOF method break down when the dressing IR intensity increases to 10^{13} W/cm^2.

Pulse duration (as)	Actual	swPROOF	PROOF
case 1	235	227	217
case 2	130	122	121

Table 4.2: *The input and retrieved pulse durations for* 10^{12} W/cm^2 *IR intensity, read from Fig 4.8.*

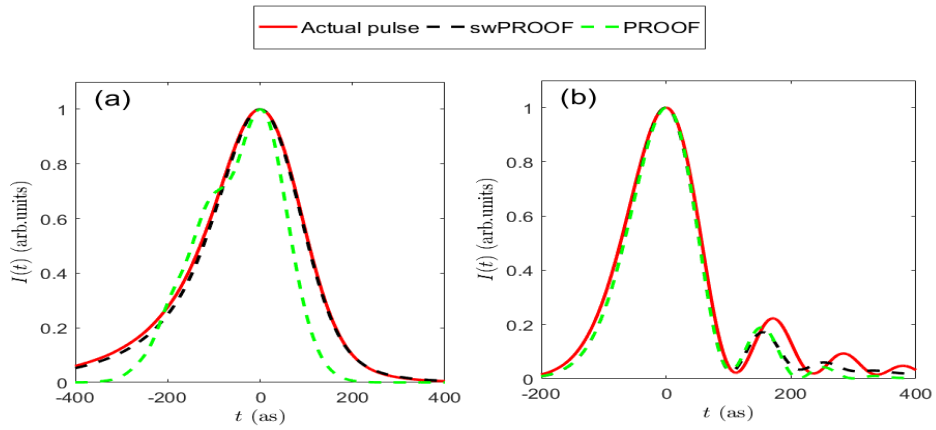

Figure 4.8: *The input and retrieved intensity profile for (a) case 1 and (b) case 2. The IR peak intensity in these simulations is* 10^{12} W/cm^2.

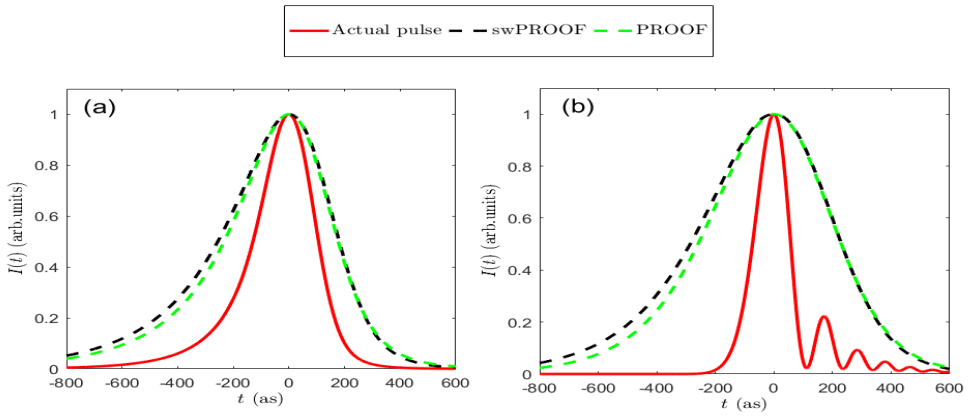

Figure 4.9: *The input and retrieved intensity profile for (a) case 1 and (b) case 2. The IR peak intensity in these simulations is* 10^{13} W/cm^2.

Pulse duration (as)	Actual	swPROOF	PROOF
case 1	235	437	410
case 2	130	516	505

Table 4.3: *The input and retrieved pulse durations for* 10^{13} W/cm^2 *IR intensity, read from Fig 4.9.*

4.3 Conclusion and outlook

In this chapter we examine the accuracy of the original PROOF method and its extension — swPROOF. When the dressing IR field is below 10^{12} W/cm^2, the XUV plus IR photoelectron spectrogram is adequately described by the second-order perturbation theory. To calibrate the intrinsic accuracy of the retrieval methods, we generated "experimental" spectrograms with the known IAPs in the known IR dressing field. Adopting the original PROOF method to retrieve the spectral phases, we established the lack of accuracy of the spectral phases retrieved, which are then reflected in the errors of pulse duration and shape in the time domain. In the PROOF method, both first and second-order dipole transition elements are calculated approximately. These approximations are undesirable and unnecessary since theoretical tools are available for their accurate evaluations. We obtained accurate two-photon dipole matrix elements using the so-called Dalgarno-Lewis method. The modified retrieval method, which we called swPROOF, is based on an accurate theory so long as the IR intensity is below 10^{12} W/cm^2. Our simulation has proven that the swPROOF method is more universal and robust than the original PROOF method.

Using real experimental data instead of TDSE simulated data, the accuracy of swPROOF will be compromised. The accuracy reported in this chapter is to be taken as the best scenario, as additional "noises" from real experimental data will be added. One drawback of the (sw)PROOF method is that it is derived for a monochromatic IR field as opposed to the short IR pulse used in real experiments. Moreover, in the weak IR field, features of the photoelectron spectra are dominated by the XUV spectral intensity. The spectral phase enters in the FSI terms which is only a small effect. The main advantage of the swPROOF is that there is no limitation on the bandwidth of the IAP. On the contrary, due to the central momentum approximation, FROG-CRAB is not suitable for characterizing IAPs with very broad bandwidths. However, the spectral phase is expected to show more pronounced effect at higher IR intensities. Therefore it is still worthwhile to develop new characterization method that depends on the SFA model but not on the central momentum approximation.

Two improved version of FROG-CRAB have been reported recently[132, 133].

High-order harmonic spectra in the water-window region and beyond have been generated with mid-infrared lasers[39, 40]. However there has not been a desirable way to characterize these pulses so far. The swPROOF method seems to be a possible choice. Unfortunately, at higher photon energies, electrons from multiple inner shells are generated. Helium is the only target that does not have this complication, but its photoionization cross section is notoriously small. The low signal-to-noise ratio may result in large error in the retrieved pulses. Clearly, characterization of water window IAPs in the time domain is an important issue that has to be faced in both theory and experiment.

Chapter 5

Retrieving atomic dipole phase and photoionization time delay

The topic of photoionization time delay has generated a great deal of controversy since the first experiment by Schultze *et al.*[6] in 2010, where a "time delay" of 21 as was reported between the ionization from the $2p$ and $2s$ shells of Ne. This delay was retrieved from streaking spectrograms using an IAP which was centered at 106 eV with a FWHM bandwidth of 14 eV, and the reconstruction was based on the FROG-CRAB method. A flurry of theoretical works have been devoted to "get" this number. The retrieved time delay was first assumed to be the "Wigner delay"[134] as the photoionization process can be regarded as a half-scattering process. Single-active-electron calculation predicts a Wigner delay difference between $2p$ and $2s$ channels of 4 to 5 attoseconds at 105 eV photon energy[6, 135]. Compared with the measured time delay, it has the same sign but a smaller magnitude. Electron correlation is then considered in terms of the random phase approximation with exchange (RPAE) method[136, 137], many-body perturbation theory (MBPT)[138], time-dependent R-matrix theory[139] and B-spline R-matrix method[140, 141]. Up to now most of the many-electron calculations that approximately account for electron correlation effects agree reasonably well with each other, but all the calculated Wigner delay differences are less

than 10 as. The effects of the strong IR field on the measured time delay was then taken into account. The contribution from Coulomb-laser-coupling (CLC), which is the interaction of the IR field with the outgoing electronic wave packet in the long-range Coulomb potential, was scrutinized[61, 127, 135, 142]. However in the considered energy range, the CLC delay was only 3 as. Although one can combine the CLC delay and the Wigner delay together, the theoretical predictions still cannot reproduce the measured value. The influence of unresolved shake-up channels was also studied[141]. The potentially strong influence of shake-up channels could result from the prevalence of near-degenerate states in excited-state manifold of the residual ion. Consequently the ionic shake-up final state can be strongly polarized by the probe IR pulse. Therefore an additional time delay due to the dipole-laser coupling (DLC) may contribute[143]. However, the DLC delay calculated so far tends to increase rather than decrease the discrepancy to experiment. In a word, what information is actually encoded in the spectrogram and how it can be retrieved is still a wide open question[61].

To address this question, in this chapter we take a fresh look at the main method of extracting temporal information from the streaking spectrogram, namely FROG-CRAB. In Section 3.2.3 we have learned that an electron wave packet can be extracted by FROG-CRAB. This wave packet is assumed to depend on the XUV pulse as well as the transition dipole moment. It looks possible to use FROG-CRAB to extract the phase (difference) of the transition dipole from which the time delay can be derived. Section 5.1 is a brief introduction to the issue of photoionization time delay, including the Wigner delay, the CLC delay and a short detour to the time delay measured using RABITT. In Section 5.2 we use the SFA model to generate photoelectron spectrograms and apply the FROG-CRAB algorithm to retrieve the time delay between the photoionization from Ne $2p$ and that from Ne $2s$ subshells or the time delay between the ionization from Ar and from Ne. We use different XUV pulses to generate the spectrogram and check the performance of the FROG-CRAB method against the XUV chirp or bandwidth. Due to the limitation of FROG-CRAB, in Section 5.3 we propose a fitting approach to extract the dipole phase and Wigner delay of Ar

by using Ne as the reference target. In Section 5.4 we investigate the error of the SFA-based FROG-CRAB method in dipole phase or time delay retrieval when using low-energy TDSE spectrograms as the input. Finally, in Section 5.5 we summarize and discuss the general issues of extracting atomic dipole phases using laser-assisted photoionization with IAPs. The materials in this chapter are adapted from the publication [123].

5.1 Introduction of photoionization time delay

5.1.1 Dipole phase and Wigner delay

Time is a classical parameter, but it is neither a dynamic variable nor an operator in quantum mechanics. For a wave packet, time normally appears in the phase factor e^{-iEt}. This implies that time can be related to the phase, or more accurately, to the derivative of phase with respect to energy. For the problem of short-range potential scattering, Eisenbud, Wigner and Smith had introduced a time delay (we call it Wigner delay)[134, 144, 145] for a given partial wave with angular momentum l:

$$\tau^W(E) = 2\frac{d}{dE}\delta_l(E), \tag{5.1}$$

in which δ_l is the phase shift of partial wave l due to the short range potential. The interpretation of this Wigner delay is classical; it can be viewed as the time delay of this particle after moving through the scattering potential compared to the classical free motion when the potential is absent. This concept is quite abstract and one cannot measure the Wigner delay directly.

Now consider photoionization, in which case a photoelectron is released and moves in the potential of the atomic core. Usually the core is charged so the potential has an asymptotic Coulomb component. For simplicity let us first assume a neutral core, i.e. photo-detachment from negative ions, so that we can consider short-range potential only, but we still call this

process "ionization". This photoemission is equivalent to a "half-scattering" process. In the entrance channel the wave function is a bound state instead of a continuum wave. Therefore the Wigner delay for photoionization becomes

$$\tau^W(E) = \frac{d}{dE}\delta_l(E). \tag{5.2}$$

To see this more clearly, let us look at the l-component of the continuum photoelectron[146]. The asymptotic form of the outgoing wave packet is

$$\Psi(\mathbf{r}, t) \propto \int_0^\infty A(E) Y_{lm}(\hat{r}) \frac{e^{i[kr+\delta_l(E)-Et]}}{r} dE. \tag{5.3}$$

Assuming that a short XUV pulse is applied to ionize this target at $t = 0$, according to first-order perturbation theory, $A(E) \propto d_{li}(E)\tilde{E}_{XUV}(\Omega)$, where $\Omega = E + I_p$ is the XUV photon energy and d_{li} is a real transition dipole matrix element between the initial bound state and the final continuum l-wave. Here we take the XUV a transform-limited pulse so that we can choose $A(E)$ a real quantity. The relation between classical and quantum descriptions can be established by introducing the "stationary phase condition". The major contribution to the integral Eq. (5.3) comes from the "trajectory" that satisfies

$$\frac{d}{dE}[kr + \delta_l(E) - Et] = 0. \tag{5.4}$$

Because $k = \sqrt{2E} = v$, the above equation leads to

$$r = v[t - \frac{d}{dE}\delta_l(E)] = v(t - \tau^W). \tag{5.5}$$

Therefore from the classical point of view, the photoemission is delayed by an amount of τ^W after the pump pulse.

When we measure the photoelectron emission in a particular direction $\mathbf{e}_k$ relative to the

light polarization (set to be z direction), the definition of Wigner delay can be generalized to

$$\tau^W(E, \mathbf{e}_k) = \frac{d}{dE}\arg d(E, \mathbf{e}_k), \tag{5.6}$$

where $d(E, \mathbf{e}_k) = \langle k\mathbf{e}_k|z|i\rangle$ is the single-photon dipole transition matrix element from the initial state to a final continuum state with asymptotic momentum $k\mathbf{e}_k$. In general $d(E, \mathbf{e}_k)$ contains the contribution from both $l = l_i - 1$ and $l = l_i + 1$ continuum waves, where l_i is the angular momentum of the initial state. Only when the initial bound state has s-symmetry ($l_i = 0$), there is a single p-component in the continuum wave, then the Wigner delay returns to its original definition $\tau^W(E) = \frac{d}{dE}\delta_1(E)$. In the following discussion we always consider the forward photoelectron, i.e. $\mathbf{e}_k = \mathbf{e}_z$, then we simply denote the transition dipole by $d(E)$.

Next we consider the XUV-photo-detachment in the presence of a synchronized IR field in which both fields have the same polarization. The vector potential of the IR is $A(t)$. Classically the photoelectron is released with kinetic momentum p_0 by the XUV-photo-detachment. If the XUV pulse is shifted by a time delay τ compared to the IR peak field, the detected momentum will be $p(\tau) = p_0 - A(\tau)$ if the XUV-photo-detachment happens instantaneously. However, because of the Wigner delay discussed above, the photoelectron is released after the XUV pulse, therefore the detected momentum becomes $p(\tau) = p_0 - A(\tau + \tau^W)$. This has been verified by TDSE simulations using short-range model potentials and transform-limited XUV pulses[61, 147]. In their simulation, a time delay can be extracted by comparing the first moment $\langle p\rangle(\tau)$ of the streaking spectrogram with the IR vector potential $-A(\tau)$. This time delay agrees with the Wigner delay calculated from the transition dipole phase theoretically.

5.1.2 Effects of the Coulomb-laser-coupling

Let us take the long-range Coulomb potential into account. For a general neutral atom, the core potential is comprised of a short-range part and a long-range Coulomb part. The transition dipole matrix element includes both the Coulomb phase shift σ_l and the short-range phase shift δ_l, as discussed in Section 3.2.2. The Wigner delay can be generalized to include the Coulomb phase shift:

$$\tau^W(E) = \frac{d}{dE}\arg d(E) \tag{5.7}$$

where $d(E)$ is given by Eqs. (3.25)-(3.27). Moreover, those equations for $d(E)$ are valid only for treating atoms in the single-electron model. In many-electron formulations with the inclusion of electron correlation, the expressions for the transition dipole are more complicated, especially when the so-called interchannel couplings are included[148]. Even with the additional complexity, however, the transition dipole for a well-defined continuum photoelectron in a given direction can always be expressed by its dipole amplitude and dipole phase, and one can still relate the Wigner delay to the energy derivative of the dipole phase.

For XUV+IR streaking measurements, in a classical view, the long-range Coulomb interaction between the continuum electron and the ionic core will modify the electron trajectory and then the final momentum. The asymptotic momentum can be written as $p(\tau) = p_0 - A(\tau + \tau^S)$ with τ^S being different from the Wigner delay τ^W. The difference is often referred to as the Coulomb-laser-coupling (CLC) delay such that:

$$\tau^S(E) = \tau^W(E) + \tau^{CLC}(E). \tag{5.8}$$

Classically one can derive an approximate formula for the CLC delay[61]:

$$\tau^{CLC}(E) \approx \frac{Z_c}{(2E)^{3/2}}\left[2 - \ln\left(\frac{2\pi E}{\omega}\right)\right]. \tag{5.9}$$

Here ω is the frequency of the IR field, and $Z_c = 1$ is the asymptotic charge seen by the photoelectron. Figure 5.1 plots the CLC delay for $\omega = 1.55$ eV. From Eq. (5.9), one can see that $\tau^{CLC}(E)$ is independent of target or IR intensity. In practice, the IR intensity should be weak enough in order to prevent field ionization and depletion of the system by the IR field but it should be strong enough to cause easily detectable energy modulations of the emitted electron. TDSE simulations using transform-limited XUV pulses for different targets have been done and from the first moment of those spectrograms the streaking time delays τ^S have been extracted, which are in good agreement with theoretical calculations based on Eq. (5.8)[135].

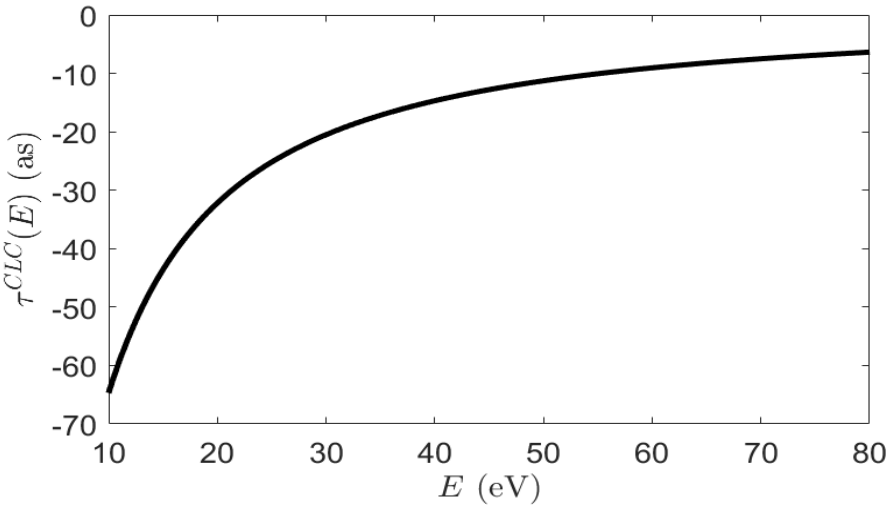

Figure 5.1: *The CLC delay according to Eq. (5.9),* $\omega = 1.55$ *eV,* $Z_c = 1$.

Equation (5.8) can be generalized to many-electron atoms with the inclusion of electron correlation, where the CLC delay is the same as in the single-electron case. Moreover, if the initial state before photoionization or the final core state after ionization has a permanent dipole moment, the dipole-laser-coupling mechanism will lead to an additional time delay τ^{dLC}, therefore Eq. (5.8) should be modified into $\tau^S = \tau^W + \tau^{CLC} + \tau^{dLC}$[143].

5.1.3 Time delay in RABITT measurements

In the RABITT measurement one uses XUV harmonics together with a delayed multi-cycle IR field to ionize target atoms. Usually the same IR field is used as the fundamental field in high harmonic generation and the dressing field in streaking. The intensities of the XUV harmonics are too weak to cause nonlinear effects, and thus only cause single photon ionization processes. Without the dressing IR field the photoelectron spectrum will show peaks at $E = (2q+1)\omega_{IR} - I_p$ from the odd harmonics. The intensity of the dressing IR is very low (typically less than 1 TW/cm^2). Thus the electron can only absorb or emit one IR photon, and the whole problem can be treated by second-order perturbation theory. Due to the existence of the IR field, sidebands at $E = 2q\omega - I_p$ appear in the photoelectron spectrum. The sideband electron S_{2q} can be simply explained by two-path interference: it comes from the electron ionized by $(2q-1)\omega$ harmonic followed by absorbing one IR photon, or ionized by $(2q+1)\omega$ harmonic followed by emitting one IR photon. Mathematically the sideband can be modeled by

$$S_{2q} = A_{2q} + B_{2q}\cos[2\omega\tau + (\varphi_{2q+1} - \varphi_{2q-1}) + \Delta\varphi_{2q}^{atomic}]. \tag{5.10}$$

Here $\varphi_{2q\pm1}$ is the phase of the $(2q\pm1)\omega$ harmonic. $\Delta\varphi_{2q}^{atomic}$ is the atomic phase. For forward electrons it can be calculated by

$$\Delta\varphi_{2q}^{atomic} = \arg[d^{(-)}(E)] - \arg[d^{(+)}(E)], \tag{5.11}$$

where $d^{(\pm)}(E)$ is the XUV+IR two-photon transition matrix elements discussed in Section 4.1.2, and $E = 2q\omega - I_p$ is the photoelectron energy of the sideband S_{2q}. In terms of time delay, Eq. (5.10) can be rewritten as

$$S_{2q} = A_{2q} + B_{2q}\cos[2\omega(\tau + t_{2q}^{e} + \tau^{(2)}(E))]. \tag{5.12}$$

Here

$$t_{2q}^{e} = \frac{\varphi_{2q+1} - \varphi_{2q-1}}{2\omega} \tag{5.13}$$

is the group delay of the XUV harmonics.

$$\tau^{(2)}(E) = \frac{\arg[d^{(-)}(E)] - \arg[d^{(+)}(E)]}{2\omega} \tag{5.14}$$

is an intrinsic atomic delay which can be directly measured from the spectrogram so long as the XUV harmonics is transform-limited.

To relate the two-photon atomic delay $\tau^{(2)}(E)$ to the Wigner delay, one should rely on the approximation Eq. (4.23). By applying this equation $\tau^{(2)}(E)$ can be separated into

$$\tau^{(2)}(E) \approx \tau^{(1)}(E) + \tau^{cc}(E), \tag{5.15}$$

in which

$$\tau^{(1)}(E) = \frac{\arg[d(E+\omega)] - \arg[d(E-\omega)]}{2\omega} \tag{5.16}$$

is a finite difference approximation to the Wigner delay $\tau^{W}(E)$, and

$$\tau^{cc}(E) = \frac{\arg[T^{cc}(E, E+\omega)] - \arg[T^{cc}(E, E-\omega)]}{2\omega} \tag{5.17}$$

is an IR-induced C-C delay which is target independent. The term T^{cc} has been given in Eq. (4.21). All the RABITT-type time delay measurements are based on the separation Eq. (5.15), which takes a similar form to Eq. (5.8).

Although the C-C delay $\tau^{cc}(E)$ in the RABITT case is derived from second-order perturbation theory, it is in excellent agreement over a wide range of electron energy with the CLC delay $\tau^{CLC}(E)$ introduced in the case of streaking[61]. One key in understanding this remarkable agreement is the intensity independence of τ^{CLC} [see Eq. (5.9)] indicating that the Coulomb-laser coupling contribution to the time shift is present in both the single-

photon and multiphoton regimes for the IR field. The IR intensities used in the numerical simulations of streaking spectrograms in Ref. [61] are within $10^{11} \sim 10^{12}$ W/cm^2 (which is somewhat too low to get a good streaking spectra) in order to achieve good convergence. In this IR intensity range the second-order perturbation theory is valid as well.

The limitation of the RABITT-type time delay measurement is that the measured delay $\tau^{(1)}(E)$ is not the real Wigner delay which is defined as the energy derivative of the dipole phase, but a finite difference of the dipole phase as shown in Eq. (5.16). Therefore if the dipole phase varies rapidly within 2ω energy range, the measured $\tau^{(1)}$ will deviate from the Wigner delay τ^W. This may be one of the reasons why the measured time delays do not agree with the values calculated by theory in the recent reports[62, 63].

5.2 Retrieving time delays using FROG-CRAB

5.2.1 Time delay between the ionization from $2p$ and $2s$ subshells of Ne

The Ne atom has two ionization channels from $2p$ and $2s$ subshells with the ionization potentials 21.56 eV and 48.47 eV respectively. The $2p$ and $2s$ photoelectrons are generated simultaneously in an XUV and a delayed IR field. Following the idea in Eq. (3.28), the total electron spectrogram can be expressed by

$$\begin{aligned} S(E,\tau) &\approx \left| \int_{-\infty}^{\infty} [\chi_{2p}(t-\tau) + \chi_{2s}(t-\tau)] e^{-i\varphi(p,t)} e^{iEt} dt \right|^2 \\ &\approx \left| \int_{-\infty}^{\infty} \chi(t-\tau) e^{-i\varphi(p_0,t)} e^{iEt} dt \right|^2 . \end{aligned} \tag{5.18}$$

Here we introduce the total wave packet $\chi(t) = \chi_{2p}(t) + \chi_{2s}(t)$ as the sum of the $2p$ and $2s$ wave packets. By applying the FROG-CRAB on the total spectrogram $S(E,\tau)$, $\chi(t)$ can be retrieved. If $S_{2p}(E,\tau)$ and $S_{2s}(E,\tau)$ are well separated in energy, it is possible to distinguish

$\tilde{\chi}_{2p}(E)$ and $\tilde{\chi}_{2s}(E)$ from $\tilde{\chi}(E)$. Then one can take the difference between the phases of these two wave packets at the same XUV photon energy Ω, according to Eq. (3.30),

$$\arg\tilde{\chi}_{2p}(\Omega) - \arg\tilde{\chi}_{2s}(\Omega) = \arg d_{2p}(\Omega) - \arg d_{2s}(\Omega). \tag{5.19}$$

In this way the dipole phase difference between $2p$ and $2s$ channels can be obtained by canceling the XUV spectral phase. The Wigner time delay between $2p$ and $2s$ ionization $\Delta\tau^{W}_{2p(2s)}$ is then calculated by taking the energy derivative of this phase difference. Note that if one applies the FROG algorithm on the $2p$ and $2s$ spectrograms individually, the same temporal axis for the two extracted wave packets cannot be guaranteed, then the obtained time delay is uncertain.

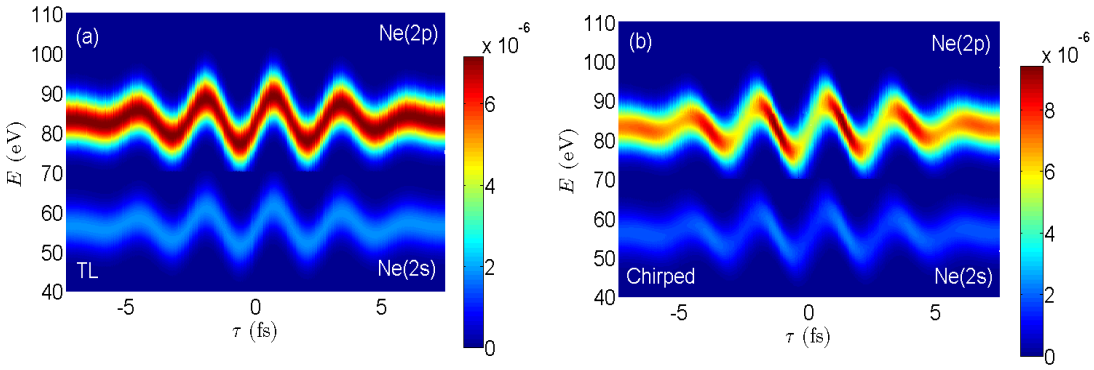

Figure 5.2: *(a) SFA-simulated Ne spectrogram for an 190 as TL XUV pulse. (b) Spectrogram for a 280 as chirped XUV. In these simulations the peak of XUV envelope and the peak of IR field overlap at τ=0. A negative τ means the XUV comes before the IR.*

To test how accurately the atomic dipole phase or Wigner delay can be retrieved from the FROG-CRAB method, we start with the most favorable conditions. We use the SFA model Eq. (3.15) to simulate spectrograms of Ne atom. We first use an 190 as transform-limited (TL) XUV pulse. In the energy domain it is centered at $\Omega_0 = 105$ eV with a FWHM (full width at half maximum) bandwidth $\Delta\Omega = 9$ eV. Its peak intensity is 8×10^{11} W/cm^2. The IR field is 800 nm in wavelength, cosine-squared envelope, 6.2 fs in FWHM duration,

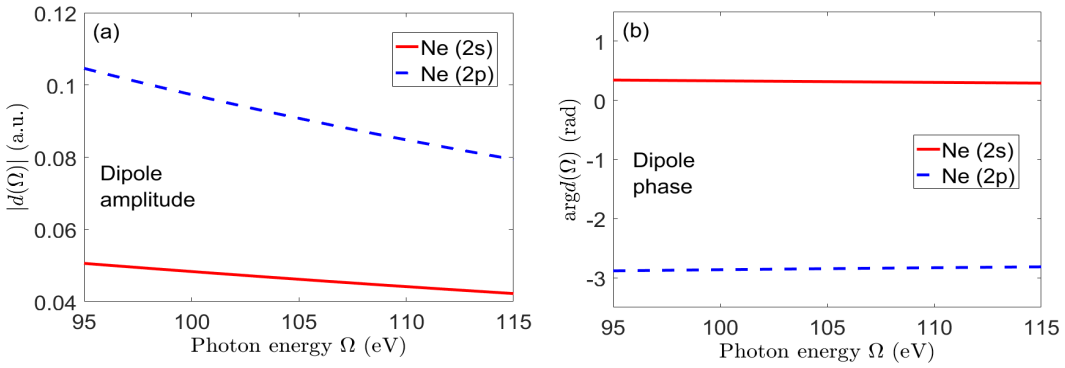

Figure 5.3: *(a) Input dipole amplitude and (b) dipole phase for Ne 2p and 2s ionization channels.*

10^{12} W/cm^2 in peak intensity and 0 degree in CEP. The simulated spectrogram is shown in Fig. 5.2(a). We also use a 280 as chirped XUV pulse which has the same spectral amplitude as the TL pulse but a quadratic spectral phase. Figure 5.2(b) is the spectrogram generated by this chirped XUV. The input amplitude and phase of the transition dipole matrix elements from $2s$ and $2p$ are plotted in Figs. 5.3(a) and (b). They are calculated via Eqs. (3.26) and (3.27) using the one-electron model potential given in Eq. (3.18).

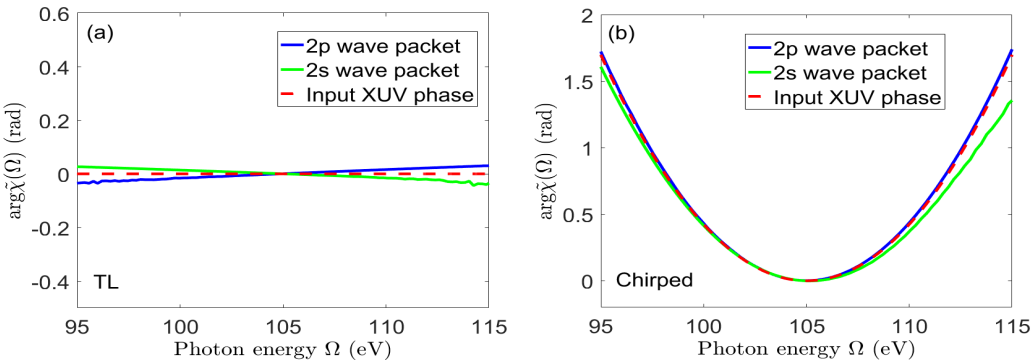

Figure 5.4: *(a) FROG-CRAB retrieved spectral phases of the 2p and 2s wave packets for the case of TL XUV. (b) Retrieved wave packet phases for the case of chirped XUV.*

The phase of the retrieved $2p$ and $2s$ photoelectron wave packets as functions of photon energy Ω are plotted in Fig. 5.4(a) for the cases of TL XUV and Fig. 5.4(b) for chirped XUV.

The retrieved results come from the FROG-CRAB using LSGPA after 100,000 iterations, where the RMS (root mean square) deviation between the input and retrieved spectrograms as well as the retrieved wave packet are observed to converge. For the TL case the retrieved wave packet phases slightly differ from the input XUV phase, which indicates the effect of the transition dipoles. For the chirped case the XUV phase is much larger than the dipole phase. We can see that the retrieved phase of the $2s$ wave packet has prominent error such that it does not follow Eq. (3.30) accurately.

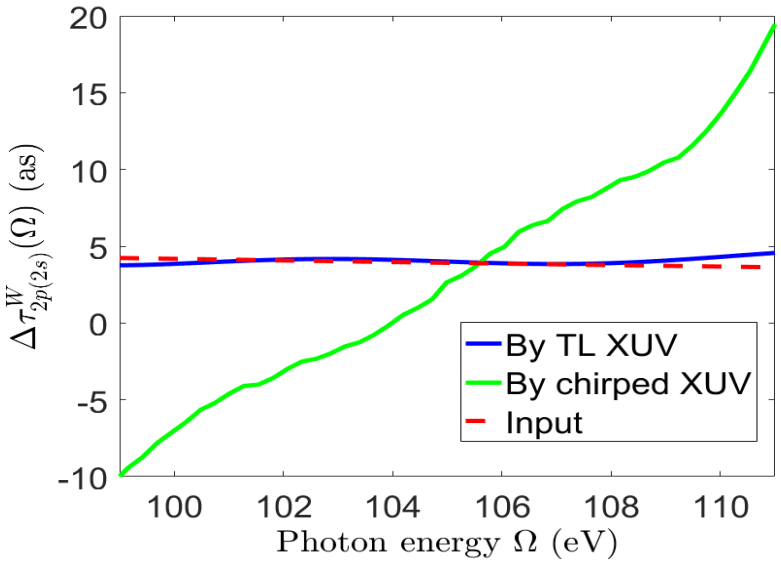

Figure 5.5: *Retrieved Wigner delay difference $\Delta\tau^W_{2p(2s)}$ from both cases compared with the input data. In frequency domain both XUV pulses are centered at 105 eV with a FWHM bandwidth of 9 eV.*

The Wigner time delay between $2p$ and $2s$ ionization $\Delta\tau^W_{2p(2s)}$ obtained in both cases are shown in Fig. 5.5 compared with the input value. The retrieved time delay agree very well with the input value for the transform-limited XUV pulse. However, for the chirped pulse, the retrieved time delay varies with photon energy significantly, from -8 as to +18 as within the spectral range of the XUV pulse, as compared to the expected constant from the input over this spectral range. The large variation of the retrieved time delays over the

spectral region also makes a single averaged time delay meaningless. In Eq. (5.19) it was assumed that the retrieved wave packets follow Eq. (3.30) exactly. Otherwise, the error will be added to the retrieved dipole phase difference and time delay, as demonstrated by the example here using chirped XUV. This example shows the measured time delay may depend on the XUV chirp, due to the limited accuracy of the retrieval method. The XUV chirp will lead to errors of several attoseconds in the retrieved time delay, which is detrimental to the accurate time delay studies. Therefore nearly transform-limited XUV pulse is required in time delay measurements. It is also worth noting that a time delay error of 10 as amounts to a phase error of 0.07 radians within an energy interval of 5 eV. To obtain sub-ten attoseconds time delay, the retrieved atomic dipole phase from experimental data has to be extremely accurate. In view of such complications an error of about 10 as from the data of Ref. [6] is probably not a cause for alarm. The XUV pulse obtained from HHG process always contains a certain degrees of attochirp. We notice that the spectrogram in Schultze *et al.*[6] [Fig. 2A of the cited reference] appears to be generated from a chirped XUV pulse, since it compares closer to the spectrogram in Fig. 5.2(b) than in Fig. 5.2(a).

5.2.2 Time delay between the ionization from Ar and Ne

In a recent experiment, Sabbar *et al.*[66] carried out streaking experiments on mixed Ar and Ne under the same XUV and IR fields. The photoelectrons are obtained in coincidence with the target ions, thus two spectrograms $S_{Ar}(E,\tau)$ and $S_{Ne}(E,\tau)$ ionized from Ar($3p$) and Ne($2p$) respectively can be separated. Since running the FROG-CRAB individually cannot guarantee the same temporal axis for the two extracted wave packets, they patched the two spectrograms together by shifting one of them upward along the energy axis. Then similar to the Ne $2p(2s)$ case the FROG was used to analyze the combined spectrogram. Since ionized by the same XUV, $S_{Ne}(E,\tau)$ and $S_{Ar}(E,\tau)$ are in the similar energy region. We then shift S_{Ar} by an energy E_{shift} so that the two spectrograms become energetically

separate. The combined spectrogram can be modeled by

$$\begin{aligned} S(E,\tau) &= S_{Ne}(E,\tau) + S_{Ar}(E-E_{shift},\tau) \\ &\approx \left|\int_{-\infty}^{\infty} \chi_{Ne}(t-\tau)e^{-i\varphi(p,t)}e^{iEt}dt\right|^2 + \left|\int_{-\infty}^{\infty} \chi_{Ar}(t-\tau)e^{-i\varphi(\sqrt{p^2-2E_{shift}},t)}e^{i(E-E_{shift})t}dt\right|^2. \end{aligned} \tag{5.20}$$

In the low energy part $S_{Ne}(E,\tau)$, p is the momentum of the photoelectrons coming from Ne targets so we can denote $p_{Ne} = p$. In the high energy part $S_{Ar}(E-E_{shift},\tau)$, $p = \sqrt{2E}$ corresponds to the energy after shifting upward, while $p_{Ar} = \sqrt{p^2-2E_{shift}}$ is the right momentum of the photoelectrons coming from Ar targets. The ranges of the momentum distributions for p_{Ne} and p_{Ar} are similar, then we can approximate the two terms $e^{-i\varphi(p_{Ne},t)}$ and $e^{-i\varphi(p_{Ar},t)}$ in Eq. (5.20) by a single term $e^{-i\varphi(p_0,t)}$ with p_0 being the central momentum. Suppose $S_{Ne}(E,\tau)$ and $S_{Ar}(E-E_{shift},\tau)$ do not overlap, then we have

$$S(E,\tau) \approx \left|\int_{-\infty}^{\infty} \chi(t-\tau)e^{-i\varphi(p_0,t)}e^{iEt}dt\right|^2. \tag{5.21}$$

The total wave packet $\chi(t) = \chi_{Ne}(t) + \chi_{Ar}(t)e^{-iE_{shift}t}$ can be extracted by applying the FROG-CRAB to this combined spectrogram. Therefore one can distinguish $\tilde{\chi}_{Ne}(E)$ and $\tilde{\chi}_{Ar}(E-E_{shift})$ so long as E_{shift} is big enough to make them separate. By comparing the Ar and Ne wave packets at the same photon energy Ω, one can then obtain the dipole phase difference and time delay between the ionization of Ar and Ne. The error of the time delay retrieved in this way is due to the central momentum approximation. The accuracy of such approximation depends on the range of p_{Ne} or p_{Ar} in which the electron flux is significantly intense. We can roughly estimate the range of momentum $\Delta p \approx \frac{\Delta\Omega}{p_0} + 2A_{max}$ where $\Delta\Omega$ is the bandwidth of the XUV pulse, A_{max} is the maximum value of the vector potential of the laser field, and the central momentum p_0 is determined by the central frequency Ω_0 of the XUV. As $\Delta\Omega$ increases while Ω_0 is fixed, the central momentum approximation will get worse. One the other hand, given the same $\Delta\Omega$, the central momentum approximation will

work better if Ω_0 increases.

To test the accuracy of time delay retrieval by patching two spectrograms together, we simulate Ar and Ne spectrograms using Eq. (3.15), combine them by shifting the Ar spectrogram and then use the FROG-CRAB to analyze the entire spectrogram. Figure 5.6(a) is the spectrogram generated using a TL XUV pulse of 160 as duration (FWHM bandwidth $\Delta\Omega = 11.5$ eV), and Fig. 5.6(b) is generated with a TL XUV of 80 as duration ($\Delta\Omega = 23$ eV). Both XUV pulses are centered at 60 eV and have the peak intensity of 10^{12} W/cm^2. The IR field is 800 nm in wavelength, cosine-squared envelope, 8.8 fs in FWHM duration, and 10^{12} W/cm^2 in peak intensity. In Figs. 5.6(a) and (b) the Ar spectrogram has been multiplied by a factor of 10 and then shifted upward by 60 eV.

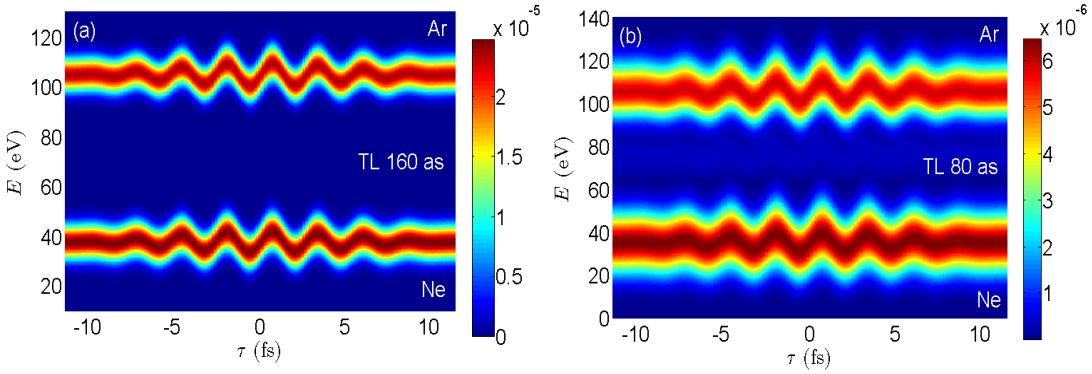

Figure 5.6: *(a) SFA simulated spectrogram of Ar and Ne using a TL 160 as XUV pulse. (b) Simulated spectrogram using a TL 80 as XUV pulse. In both cases the Ar spectrogram has been multiplied by a factor of 10 and shifted upward by 60 eV.*

We apply the LSGPA FROG-CRAB to these spectrograms. After 100,000 iterations the FROG algorithm is verified to achieve converged results. Furthermore we change the energy shift E_{shift} to generate new input spectrograms and repeat the FROG-CRAB. Figure 5.7(a) shows the retrieved time delay $\Delta\tau^W_{Ar(Ne)}$ using the 160 as XUV compared with the input value. Since the XUV has a relatively narrow bandwidth, for $E_{shift} \geq 50$ eV the Ne and Ar spectrograms can be well separated, and the central momentum approximation works quite well. The retrieved time delay is not sensitive to E_{shift} and the error is less than 10 as within

the FWHM bandwidth of the XUV. However, for the case of the 80 as broadband XUV, the retrieved results strongly depend on E_{shift}, as shown in Fig. 5.7(b). When E_{shift} takes the value of 50 or 60 eV, it is not big enough to totally separate the Ar and Ne spectrograms, and the retrieved time delay has an error of more than 20 as. When E_{shift} = 80 eV, the two spectrograms are well separated, then the retrieved time delay becomes closer to the input value. The remnant error comes from the central momentum approximation since here we use an XUV pulse with a larger $\Delta\Omega$. In summary, the FROG-CRAB based time delay retrieval by patching two spectrograms together is reliable only for narrow band XUV pulses.

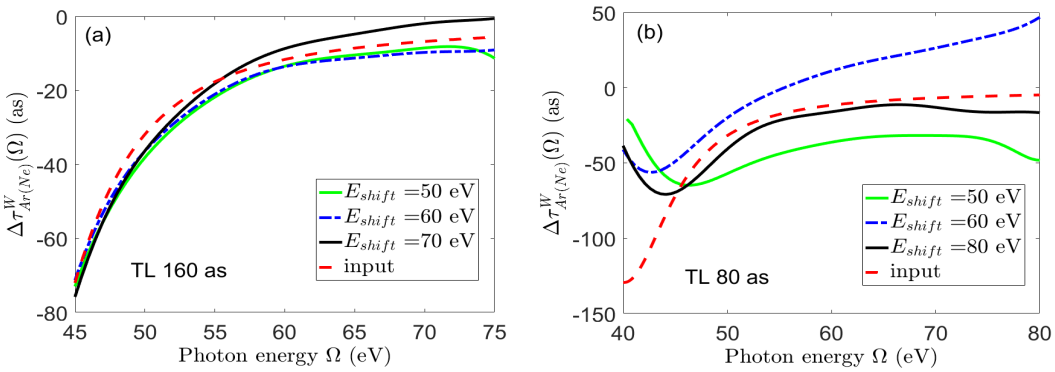

Figure 5.7: *FROG-CRAB retrieved Wigner time delay between the ionization of Ar and Ne $\Delta\tau^{W}_{Ar(Ne)}$ for various energy shift E_{shift}, compared with the input value. (a) Using an 160 as TL XUV, centered at 60 eV with a FWHM bandwidth of 11.5 eV. (b) Using an 80 as TL XUV, centered at 60 eV with a FWHM bandwidth of 23 eV.*

5.3 Time delay retrieval through a fitting procedure for broadband IAPs

We have shown that in order to retrieve the dipole phase difference or time delay successfully using the FROG-CRAB method, the XUV pulse has to have small attochirp and narrow bandwidth. The accuracy of the FROG-CRAB is limited by the central momentum ap-

proximation. Here we propose a different approach to improve the accuracy of time delay retrieval when using broadband XUV pulses or more intense IR fields. To be more specific, suppose we have Ar and Ne spectrograms generated under the same XUV and IR field, and we assume that the dipole amplitude and phase of Ne are known and the dipole amplitude of Ar is also known (from XUV ionization alone), our goal is to retrieve the Ar dipole phase. This can be done in three steps. First, the FROG algorithm is used to extract the XUV pulse from the Ne spectrogram, as demonstrated in Section 3.3.1. Second, we set time zero at the peak of the XUV envelope and retrieve the IR field by fitting this Ne spectrogram directly using Eq. (3.15), i.e., without the central momentum approximation, as presented in Section 3.3.3. Third, since both XUV and IR have been extracted, we then retrieve the dipole phase of Ar by fitting the Ar spectrogram, again based on Eq. (3.15).

We use the SFA model to simulate both Ar and Ne spectrograms under the same XUV and IR field. The IR field is 800 nm in wavelength, cosine-squared envelope, 8.8 fs in FWHM duration, and we increase its peak intensity to 10^{13} W/cm^2. Two XUV pulses are used which have the same spectral amplitude with a center frequency $\Omega_0 = 60$ eV and a bandwidth $\Delta\Omega = 23$ eV. The first pulse is transform-limited so that its FWHM duration is 80 as, while the second pulse is chirped with a duration of 130 as. The input and retrieved XUV pulses have been given in Figs. 3.2(c)-(e). The next step is the retrieval of the IR field by fitting the Ne spectrogram using the known Ne dipole and the extracted XUV. For the case of TL XUV the retrieved IR field has been shown in Fig. 3.5. For the case of chirped XUV, the IR field was accurately retrieved by this fitting process too.

Now we focus on the third step — using fitting to extract the dipole phase or Wigner delay of Ar from the Ar spectrogram without the central momentum approximation. Here we choose to use the micro-GA[149] (genetic algorithm) with the fitness function given by

$$Q = \int\int \left(\sqrt{S_{\text{input}}(E,\tau)} - \beta\sqrt{S_{\text{fitting}}(E,\tau)}\right)^2 dE d\tau, \tag{5.22}$$

where β is an overall renormalizing factor treated as a fitting parameter. The dipole phase

arg$d(E)$ is constructed by samples $(E_i, \arg d_i)$ through cubic-spline interpolation. In this case 12 samples are used and the optimal vertical coordinates argd_i are obtained by micro-GA. During this optimization the horizontal coordinates E_i are fixed, but they are not evenly distributed. We put more samples on the low energy side while fewer on the high energy side since the dipole phase should change slowly in high energy region. There are 8 individuals in each generation and the results are obtained after 2000 generations. The retrieved Wigner delay of Ar by fitting for both TL and chirped XUV cases are plotted in Fig. 5.8. The input τ^W_{Ar} within the FWHM bandwidth of the XUV pulse is accurately retrieved by this fitting method for the case of transform limited XUV, while errors up to 10 as are observed if the chirped XUV is used. In Section 5.2.2 we have retrieved the delay difference $\Delta\tau^W_{Ar(Ne)} = \tau^W_{Ar} - \tau^W_{Ne}$ by using FROG-CRAB for the case of 80 as TL XUV pulse, see Fig. 5.7(b). We choose the $\Delta\tau^W_{Ar(Ne)}$ obtained by setting $E_{shift} = 80$ eV and add the τ^W_{Ne} which is calculated from the input Ne dipole to it, then we can get a τ^W_{Ar} retrieved from FROG-CRAB method. This result is also plotted in Fig. 5.8 in dot-dashed line to be compared with the fitting result in solid blue line. Clearly the fitting approach is more accurate because it gets rid of the central momentum approximation in its second and third steps. However since the central momentum approximation is still included in the first step of our new procedure, the errors in the extracted XUV pulses will affect the accuracy of the retrieved time delay. This effect becomes more prominent when chirped XUV pulses are used.

From Fig. 3.2(a) and (b) we can see the XUV phase has a strong effect on the spectrogram. However the spectrogram is not very sensitive to the dipole phase of the target. To demonstrate this point, we use two artificial targets which have different dipole phases from the input Ar target, and generate spectrograms under the same 80 as TL XUV and the same IR field. Figure 5.9(a) shows the corresponding Wigner delays of the two artificial targets as well as that of the input Ar. Figures 5.9(b) and (c) are their electron spectra at two particular delays between the XUV and the IR. Although the Wigner delays can

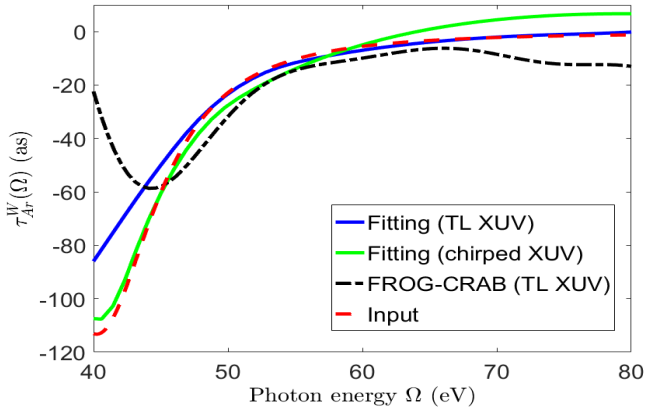

Figure 5.8: *Wigner delay of Ar. (Solid blue line): Retrieved by fitting for the case of 80 as TL XUV. (Solid green line): Retrieved by fitting for the case of 130 as chirped XUV. (Dot-dashed black line): Retrieved from FROG-CRAB for the case of 80 as TL XUV, by choosing $E_{shift} = 80$ eV and using the input Ne dipole. (Dashed red line): Input data. In energy domain the XUV pulses are centered at 60 eV with FWHM bandwidth of 23 eV.*

differ by more than 20 as, the electron spectrograms or their sectional plots at fixed delays are not visually different. This insensitivity of the streaked electron spectra with respect to the dipole phase makes it challenging to retrieve accurate dipole phase, especially when the XUV phase has large attochirp so that the effect of the dipole phase becomes more insignificant.

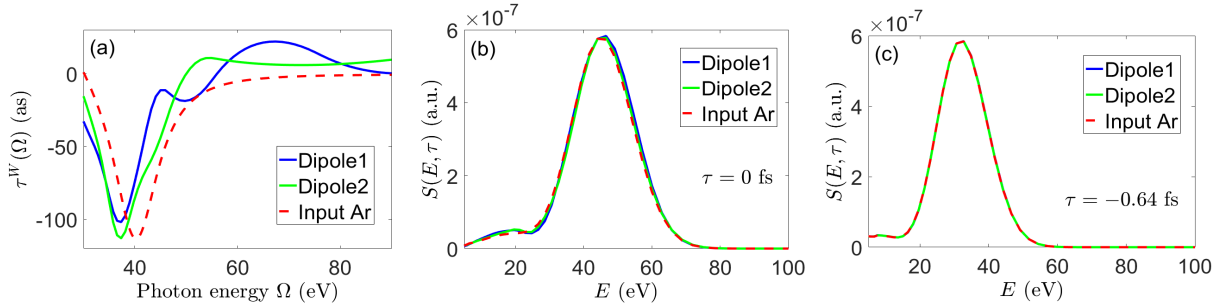

Figure 5.9: *(a) Wigner delays for the two artificial targets compared with the Wigner delay of the input Ar target. (b) Photoelectron spectra for these targets at $\tau = 0$ fs. (c) Photoelectron spectra at $\tau = -0.64$ fs.*

To test the robustness of our new approach with respect to noise, we repeat the procedure above for spectrograms contaminated by random errors. Starting from the Ne and Ar spectrograms simulated by SFA, we add random noise and treat the new spectrograms as the input of our retrieval. Here the noise at each data point has a mean-zero normal distribution with a standard deviation of 5% or 10% of the original value. Figure 5.10 demonstrates that this modified FROG-CRAB fitting method is stable for random errors up to 10%, therefore it can actually be applied to real experimental data.

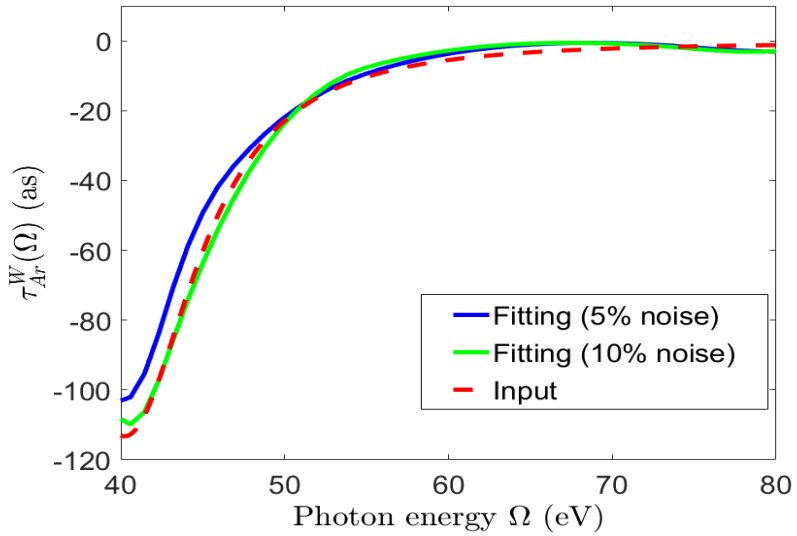

Figure 5.10: *Wigner delay of Ar retrieved by the fitting approach compared with the input value. We have added 5% or 10% random errors to the original Ne and Ar spectrograms as the new input data.*

5.4 Time delay retrieval from low-energy photoelectron spectra

The retrieval methods presented in section 5.2 and 5.3 assume that the spectrograms can be accurately modeled by SFA. However, the SFA equation (3.15) does not take into account the

interaction between the continuum electron and the ionic core. It is a good approximation only for high energy photoelectrons with energies higher than 30 or 40 eV. In Fig. 5.11 we compare low energy spectrograms for Ar calculated by solving SAE TDSE and by using SFA. The TDSE and SFA spectrograms for Ne have been given in Figs. 3.3(a) and (b). These spectrograms are generated by a TL XUV pulse which is 160 as in FWHM duration and 10^{12} W/cm^2 in peak intensity. In the frequency domain the amplitude of this pulse has a Gaussian shape centered at 40 eV with 11.5 eV FWHM bandwidth. The IR field is 800 nm in wavelength, cosine-squared envelope, 4.4 fs in FWHM duration, and 10^{13} W/cm^2 in peak intensity. Clearly one can see the error of the SFA model as compared to TDSE results from these spectrograms.

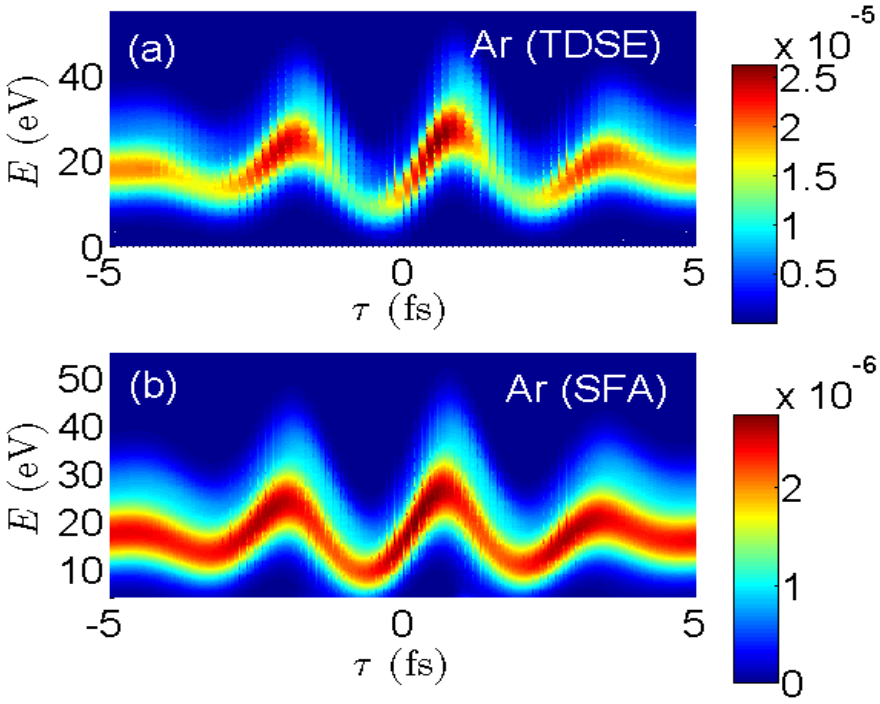

Figure 5.11: *(a) TDSE and (b) SFA simulated low energy electron spectrograms for Ar.*

From Section 3.3.2 we know that relatively accurate XUV pulses can be retrieved using the FROG-CRAB although the SFA model used in the method does not describe the

spectrogram very accurately. However, the limitation of the SFA model for low energy photoelectrons has a more significant effect on the dipole phase or time delay retrieval. Here we patch the TDSE simulated Ne and Ar spectrograms Figs. 3.3(a) and 5.11(a) together. The Ar spectrogram has been multiplied by a factor of 16 and then shifted upward by 60 eV. FROG-CRAB is then applied to the whole spectrogram and a total electron wave packet is extracted, from which we separate the Ar and Ne wave packets and compare them at the same photon energy. Figures 5.12(a) and (b) shows the amplitude and phase of the two extracted wave packets after 100,000 iterations compared with that of the input XUV pulse. One can see that the amplitude of the Ar or Ne photoelectron wave packet differs from the XUV amplitude, which demonstrates the role of the transition dipole amplitude.

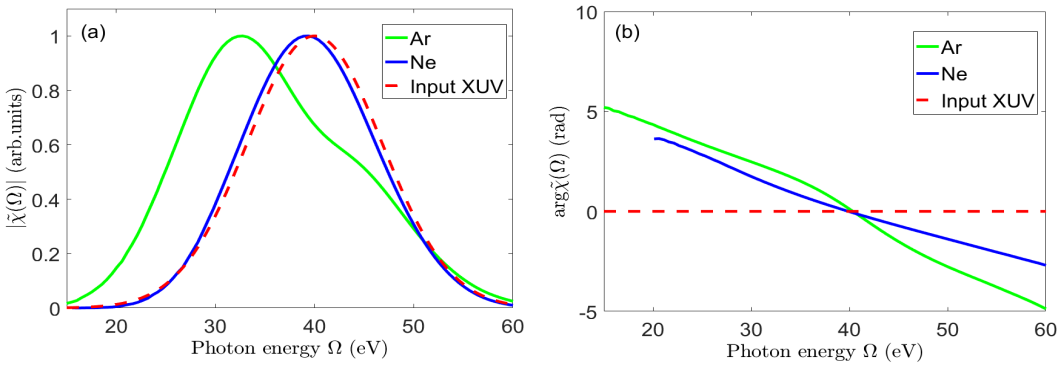

Figure 5.12: *(a) Amplitude and (b) phase of the retrieved photoelectron wave packets of Ar and Ne as functions of photon energy Ω, compared with the amplitude and phase of the input XUV pulse. The wave packets are retrieved using FROG-CRAB from combined Ar and Ne spectrograms simulated by TDSE.*

We then calculate the phase difference between the two electron wave packets and take derivative of this difference with respect to energy to obtain the photoionization time delay between Ar and Ne, shown in the solid blue line in Fig. 5.13. The retrieved time delay can only qualitatively reproduce the input Wigner time delay. Within the XUV FWHM bandwidth the error can be up to 50 as, and the minimum in the retrieved result shifts by 2 eV compared with that in the input value. According to the assumption Eq. (5.8), we can

subtract the CLC delay difference $\tau^{CLC}_{Ar(Ne)}(\Omega) = \tau^{CLC}_{Ar}(\Omega) - \tau^{CLC}_{Ne}(\Omega)$ from the FROG-CRAB retrieved time delay between Ar and Ne, as plotted in the solid green line in Fig. 5.13. Note that $\tau^{CLC}_{Ar(Ne)}$ is a positive quantity. Even after subtracting the CLC part, the errors between the retrieved time delay and the input Wigner delay calculated from the dipole phase corresponding to the model potential cannot be eliminated. On the contrary, if we combine the two SFA simulated spectrograms Figs. 3.3(b) and 5.11(b) in the same way as the input of FROG-CRAB, the retrieved time delay agrees with the input value quite well. Therefore the error in the retrieved time delay from TDSE simulated spectrograms reflects the deficiency of the SFA model on which the FROG-CRAB method is based.

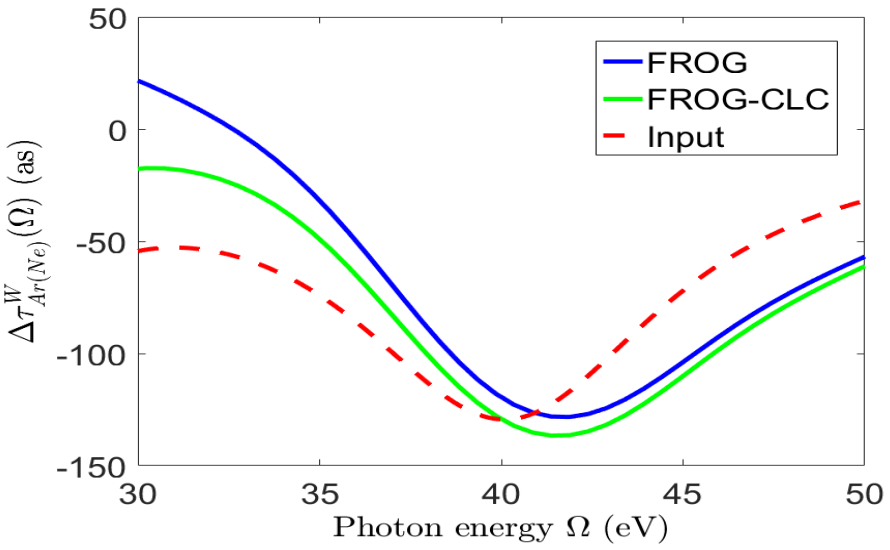

Figure 5.13: *The time delay between the ionization from Ar and Ne. (Solid blue line): By taking energy derivative of the phase difference between the two retrieved wave packets in Fig5.12(b). (Solid green line): After subtracting the positive CLC part $\Delta\tau^{CLC}_{Ar(Ne)}(\Omega)$. (Dashed red line): Input Wigner delay between Ar and Ne. The input XUV pulse is TL with a FWHM duration of 160 as. In energy domain it is centered at 40 eV with a FWHM bandwidth of 11.5 eV.*

Additionally, we repeat the micro-GA fitting method presented in section 5.3 for the TDSE simulated Ne and Ar spectrograms Figs. 3.3(a) and 5.11(a). The XUV pulse retrieved

from the Ne spectrogram via FROG-CRAB has been shown in Figs. 3.3(c)-(e). The IR field can also be accurately retrieved from the Ne spectrogram by fitting, although the fitting method is based on SFA Eq. (3.15). In Fig. 5.14 we plot the photoionization time delay of Ar retrieved from the Ar spectrogram by GA-fitting in the solid blue line. In this fitting approach we use the known dipole amplitude of Ar as well as the extracted XUV and IR field, and the dipole phase was discretized into 10 samples. There are 8 individuals in each generation and the converged result comes after 2000 generations. We then subtract the negative CLC delay $\tau_{Ar}^{CLC}(\Omega)$ from the fitting result, as plotted in the solid green line in Fig. 5.14. As a comparison, we also plot the Wigner delay of Ar retrieved by FROG-CRAB in the dot-dashed black line. This value is obtained by adding the Wigner delay of Ne calculated from the input Ne dipole on the retrieved $\Delta\tau_{Ar(Ne)}^{W}$ given in the solid green line in Fig. 5.13. One can see in this case the fitting approach is even less reliable than the FROG-CRAB method. These results again demonstrate the inaccuracy of the SFA model in the low energy region for the purpose of retrieving the dipole phase or time delay.

5.5 Conclusion

In this chapter, we have examined the controversial time delay issue in recent attosecond XUV photoionization streaking experiments. We have identified the conditions and demonstrated how the FROG-CRAB can be used to retrieve the phase of the transition dipole in such experiment. Due to the insensitivity of the spectrogram to the atomic dipole phase and due to the central momentum approximation, accurate retrieval of the dipole phase is difficult unless the XUV is nearly transform-limited and the spectral bandwidth of the XUV is relatively narrow. Under the most favorable conditions, FROG-CRAB can give the phase difference between two transition dipoles as a function of the photon energy.

The examples reported in this chapter illustrate that for low-energy photoelectrons ($E <$ 30 eV), due to the inaccuracy of the SFA model, the FROG-CRAB can only retrieve the

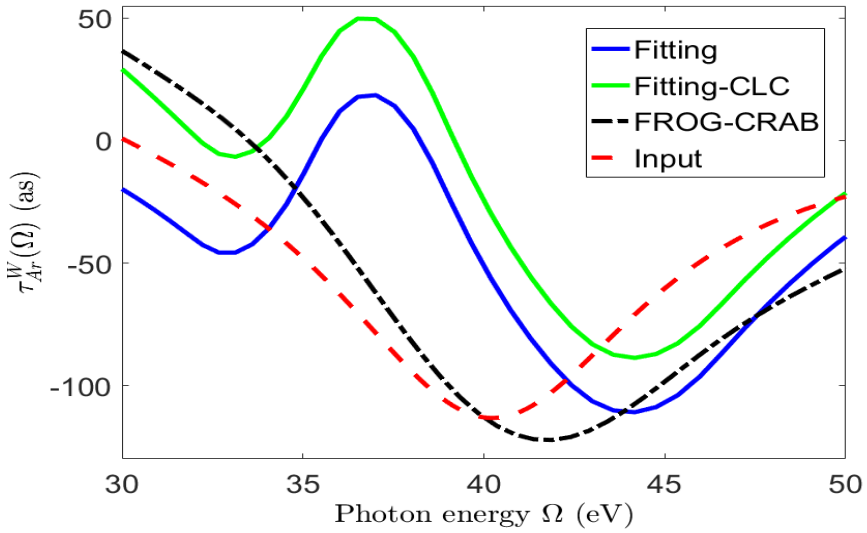

Figure 5.14: *Photoionization time delay of Ar (Solid blue line): Retrieved from the Ar spectrogram simulated by TDSE through GA-fitting. (Solid green line): After subtracting the negative CLC term $\tau_{Ar}^{CLC}(\Omega)$. (Dot-dashed black line) Retrieved by FROG-CRAB, using the input Ne dipole. (Dashed red line): Input Wigner delay of Ar.*

photoionization time delay qualitatively. On the other hand, for high-energy photoelectrons such as in the experiment by Schultze *et al.*, where an XUV pulse centered at 106 eV was used, the SFA is quite adequate. In this circumstance, the dipole phase (time delay) retrieved using FROG-CRAB can be treated as the dipole phase (time delay) of the XUV photoionization alone. Ideally the retrieved results should be independent of the IR and the XUV used. However, at high photoelectron energies, the dipole phase is relatively flat with respect to the energy, thus the retrieved dipole phase will be sensitive to any inaccuracy resulting from the FROG retrieval algorithm, especially if the XUV has some degree of attochirp. Underlying this difficulty is the fact that the spectrogram is much less sensitive to the dipole phase of the target than to the phase of the XUV pulse. In view of this difficulty, the time delay of 21 as reported by Schultze *et al.* may contain intrinsic errors in the retrieval process. Moreover, the FROG-CRAB method imposes a limitation on the XUV bandwidth. For broadband XUV pulses the central momentum approximation used in the FROG-CRAB method would fail. As an alternative we have proposed a procedure based on fitting to retrieve the dipole phase of an unknown target using a well-known reference target, which is applicable for XUV pulses with a broad bandwidth.

The Wigner time delay is defined as the first-order energy derivative of the dipole phase. This time delay is actually remotely related to the original time delay defined by Wigner for a stationary system. The transition dipoles are for photoelectrons emerging in the direction of the polarization axis, rather than in a particular partial wave. Only by analyzing the whole electron wave packet that is generated in XUV photoionization one can draw a conclusion about the time information of the photoelectrons. The Wigner delay taken at the peak energy of the wave packet can be understood as the group delay of the electron wave packet only when the XUV pulse is transform-limited. The time delay thus defined does not convey the notion of the delay of a photoelectron reaching the detector directly. While a large Wigner time delay may imply a slowdown of the electron wave packet after it leaves the atom, such a slowdown cannot be measured experimentally, especially on the attosecond

time scale with conventional detectors. In fact, a similar "slowdown" occurs when light travels through a dispersive medium. A group velocity (or an index of refraction) can be defined if the dispersion is small. When the medium is highly dispersive, the group velocity alone cannot describe the motion of the wave packet. In this case, a full characterization of the spectral phase is needed. In the same vein, for the streaking experiment, it is the spectral phase of the electron wave packet generated by the XUV pulse that is retrieved. This information will enable the full characterization of the complex electron wave packet including its time dependence in the coordinate space. But using a single time delay to represent the whole electron wave packet is an oversimplification. This oversimplification is one of the main reasons for the existing debates, especially when the "delay" is of the order of a few tens of attoseconds or less.

Chapter 6

Observing the ultrafast buildup of a Fano resonance with ATAS

Fano resonance plays a fundamental role in nuclear, atomic, molecular, and condensed-matter physics. It generally occurs in the situation of photo-excitation of discrete quantum states embedded in and coupled to a continuum. The discrete bound state decays through electron-electron correlation by ejection of one electron and relaxation of the ion to a lower-energy configuration. The energy of the photoelectron emitted through this autoionization mechanism (referred to as the "closed channel") coincides with that emitted by direct photoionization (the "open channel"). The two ionization pathways are indistinguishable and thus interfere, leading to a characteristic shape in the photo-absorption spectrum, that is, the Fano shape[150]. In the prominent example of helium, a series of doubly excited states ($sp_{2,n+}$) between the $N = 1$ and $N = 2$ ionization threshold exists. These states can be coupled to the continuum of He^+ ($1s$) ionic states due to the Coulomb interaction among the two electrons. Therefore a series of asymmetric Fano lines in the XUV absorption spectrum can be observed. Each Fano line serves as a signature of the corresponding autoionizing state. It has been demonstrated that the Fano line shapes can be converted to Lorentzian shapes and vise versa by applying an intense IR pulse to the XUV excitation[56].

When an IAP is used to excite the sample then followed by an IR pulse, changing the relative delay between these two pulses one can measure a series of XUV absorption profiles. The measured 2-dimensional signal may encode ultrafast dynamics of the sample and this technique is often referred to as the attosecond transient absorption spectroscopy (ATAS). ATAS has been performed on noble gas atoms such as Kr[55], Ar[151], Ne[152] and Xe[153]. A lot of theoretical work has been carried out to interpret the absorption spectra where the IR pulse overlaps with the XUV pulse. The mechanisms which result in such complicated structures may include light-induced states[154], the Autler-Townes splitting[155], and the Stark shift[156]. The physics behind these mechanisms lies in the coupling to dark states by IR photons[157–159]. The subcycle interference fringes[152, 160] can be attributed to the interference between two pathways that both result in the same final state[161]. Quantum beating between multiple electronic states was also observed by ATAS, both for Ne[162] and He[58]. For molecules, recently a vibrational wave packet within the excited electronic state of H_2 was reconstructed via ATAS[163].

This chapter is adapted from a recent publication [164], where the time-dependent buildup of Fano line shape in photoabsorption spectrum has been observed by using ATAS technique. Section 6.1 gives a general derivation of the photoabsorption cross section, which can be calculated from the imaginary part of the induced dipole moment. Section 6.2 presents the ultrafast dynamics of Fano resonance. Considering one bound state embedded in a continuum, we derived the time-dependent evolution of the two-electron wave packet based on Fano's theory[150]. From the wave packet we can easily get the time-dependent induced dipole moment. Then by approximating the IR pulse as a temporal gate to terminate the induced dipole, an analytical model for the delay-dependent photoabsorption spectra can be achieved. In Section 6.3 we compare the experimental result and the analytical model. The agreement confirms that we have observed the dynamics of two-electron correlation in the form of the time-dependent buildup of Fano resonance. Section 6.4 is a brief summary of this chapter.

6.1 Formulation of light absorption at the single atom level

In absorption spectroscopy there is an exchange of energy between the light and the atom. We first formulate a generalized cross section for the nonlinear interaction between the light field and an atom[155]. The Hamiltonian of an atom in the light field can be written as

$$H = H_A + E(t)z. \tag{6.1}$$

Here $E(t)$ is the light field. It can be an XUV pulse only or a two-color field consisting of an IAP and a delayed IR field. We consider the light field is linearly polarized along the z-direction. The electron in the atom is described by H_A. The time dependent Schrödinger equation is

$$i\frac{\partial}{\partial t}|\Psi(t)\rangle = H|\Psi(t)\rangle. \tag{6.2}$$

The rate of change of the energy ε of the atom is calculated as

$$\begin{aligned} \frac{d\varepsilon}{dt} &= \frac{d}{dt}\langle\Psi(t)|H|\Psi(t)\rangle = \langle\Psi(t)|\frac{\partial H}{\partial t}|\Psi(t)\rangle \\ &= \langle\Psi(t)|z|\Psi(t)\rangle\frac{\partial}{\partial t}E(t) = d(t)\frac{\partial}{\partial t}E(t) \end{aligned} \tag{6.3}$$

where the induced dipole in the time domain is expressed by $d(t) = \langle\Psi(t)|z|\Psi(t)\rangle$. Using the relation $\tilde{E}^*(\Omega) = \tilde{E}(-\Omega)$ one can write

$$\Delta\varepsilon = \int_{-\infty}^{\infty} d(t)\frac{\partial E}{\partial t}dt = \int_{-\infty}^{\infty} i\Omega\tilde{d}(\Omega)\tilde{E}^*(\Omega)d\Omega = \int_0^{\infty} \Omega S(\Omega)d\Omega, \tag{6.4}$$

where the absorption spectra

$$S(\Omega) = 2\mathrm{Im}\left[\tilde{d}(\Omega)\tilde{E}^*(\Omega)\right]. \tag{6.5}$$

A generalized absorption cross section $\sigma(\Omega)$ can be defined as the ratio of energy absorbed per unit time per unit frequency divided by the incident intensity at a given frequency

$$\sigma(\Omega) = \frac{\Omega S(\Omega)}{I_0(\Omega)} = \frac{\Omega S(\Omega)}{c|\tilde{E}(\Omega)|^2/4\pi} = 4\pi\alpha \frac{\Omega S(\Omega)}{|\tilde{E}(\Omega)|^2}. \tag{6.6}$$

where c is given by the inverse of the fine structure constant α. If we are interested in the light absorption in a narrow frequency range in the vicinity of resonance, and the bandwidth of the IAP XUV pulse is much greater than this range, then $\tilde{E}(\Omega)$ and Ω can be treated as constant. Approximately we have

$$\sigma(\Omega) \propto \mathrm{Im}[\tilde{d}(\Omega)]. \tag{6.7}$$

6.2 Ultrafast autoionization dynamics of Fano resonances

Fano resonance was treated in 1961 by U.Fano[150] in terms of the interaction between a discrete bound state and its embedded continuum. Take the the $2s2p\ ^1P$ doubly excited state of He atom as an example and denote this state by $|\alpha\rangle$. It is degenerate with the $1sEp\ ^1P$ continuum states which will be denoted by $|\beta_E\rangle$. The Hilbert space consists of two channels. For the closed channel, it has one eigenstate, $|\alpha\rangle$. For the open channel, there are continuum states, $|\beta_E\rangle$. Between the two channels, there is a coupling term V_E. The Hamiltonian can be written as

$$\langle\alpha|H|\alpha\rangle = E_r, \tag{6.8}$$

$$\langle\beta_E|H|\beta_{E'}\rangle = E\delta(E - E'), \tag{6.9}$$

$$\langle\beta_E|H|\alpha\rangle = V_E. \tag{6.10}$$

In the vicinity of resonance energy E_r, one can assume that $V_E = V$ is a constant. We use a very short XUV to excite He atom and assume that at $t > 0$ the pulse is over. The time evolution of the wave packet near the resonance for $t > 0$ can be expressed in terms of the ground state $|g\rangle$, the bound state $|\alpha\rangle$ and the continuum $|\beta_E\rangle$:

$$|\Psi(t)\rangle \approx e^{-iE_g t}|g\rangle + C_\alpha(t)|\alpha\rangle + \int C_E(t)|\beta_E\rangle dE, \tag{6.11}$$

in which E_g is the ground state energy. The field-free evolution of the coefficients $C_\alpha(t)$ and $C_E(t)$ is governed by time-dependent Schrödinger equation $i\frac{\partial}{\partial t}|\Psi(t)\rangle = H|\Psi(t)\rangle$, which turns into the coupled equations:

$$\dot{C}_E(t) = -iVC_\alpha(t) - iEC_E(t), \tag{6.12}$$

$$\dot{C}_\alpha(t) = -iE_r C_\alpha(t) - iV\int C_E(t)dE. \tag{6.13}$$

Then we can solve Eqs. (6.12) and (6.13) given the energy-independent initial values $C_\alpha^{(0)}$ and $C_E^{(0)}$. The results are[165]:

$$C_\alpha(t) = C_\alpha^{(0)}\left(1 - \frac{i}{q}\right)e^{-iE_r t}e^{-\frac{\Gamma}{2}t}, \tag{6.14}$$

$$C_E(t) = \frac{C_E^{(0)}}{\epsilon + i}e^{-iE_r t}\left\{(q+\epsilon)e^{-i\frac{\Gamma}{2}\epsilon t} - (q-i)e^{-\frac{\Gamma}{2}t}\right\}. \tag{6.15}$$

Here we introduce the parameters Γ, q and ϵ. $\Gamma = 2\pi V^2$ is the width of resonance. The scaled energy $\epsilon = \frac{E-E_r}{\Gamma/2}$. q is the shape parameter in Fano's theory:

$$q = \frac{C_\alpha^{(0)}}{\pi V C_E^{(0)}} = \frac{\langle\alpha|z|g\rangle}{\pi V\langle\beta_E|z|g\rangle}. \tag{6.16}$$

Equation (6.14) shows the bound state decays exponentially. In Eq. (6.15), the continuum amplitude exhibits the interference between the direct ionization part and the decay part.

To calculate the absorption spectra we need the induced dipole $d(t)$ for $t \geq 0$. Assuming that the electric field is polarized along the z-axis,

$$\begin{aligned} d(t) &= \langle \Psi(t)|z|\Psi(t)\rangle = C_\alpha(t)e^{iE_g t}\langle\alpha|z|g\rangle^* + \int C_E(t)e^{iE_g t}\langle\beta_E|z|g\rangle^* dE + c.c. \\ &= C_\alpha^{(0)}\langle\alpha|z|g\rangle^* e^{-i\Omega_r t}\left\{(1-\frac{i}{q})e^{-\frac{\Gamma}{2}t} + \frac{1}{(\pi V q)^2}\int \frac{(q+\epsilon)e^{-i\frac{\Gamma}{2}\epsilon t} - (q-i)e^{-\frac{\Gamma}{2}t}}{\epsilon+i}dE\right\} + c.c. \end{aligned} \tag{6.17}$$

Here $\Omega_r = E_r - E_g$ is the resonance frequency. We can apply the rotating wave approximation to drop the complex conjugate part for XUV absorption. With the help of $\int_{-\infty}^{\infty}\frac{1}{\epsilon+i}d\epsilon = -i\pi$, Equation (6.17) can be simplified to

$$d(t) \propto i\left[2\delta(t) + \frac{\Gamma}{2}(q-i)^2 e^{-\frac{\Gamma}{2}t}e^{-i\Omega_r t}\right]. \tag{6.18}$$

Then according to Eq. (6.7), the photoabsorption cross section or the optical density (OD) takes the following form:

$$\begin{aligned} \sigma(\Omega) &\propto \mathrm{Im}\left[\int_0^\infty d(t)e^{i\Omega t}dt\right] \\ &\propto \mathrm{Re}\left[1 + \frac{\Gamma}{2}(q-i)^2\int_0^\infty e^{-\frac{\Gamma}{2}t}e^{i\Delta\Omega t}dt\right] \qquad (6.19) \\ &\propto \mathrm{Re}\left[1 + \frac{(q-i)^2}{1-i\epsilon}\right] = \frac{(q+\epsilon)^2}{1+\epsilon^2}. \qquad (6.20) \end{aligned}$$

In the above equations $\Delta\Omega = \Omega - \Omega_r$ is the frequency detuning and $\epsilon = \frac{\Delta\Omega}{\Gamma/2}$ is the scaled energy. Equation (6.20) is the typical form in Fano's theory to characterize the XUV absorption cross section in the vicinity of resonance. However, such XUV absorption spectrum is obtained when t goes to infinity and it does not contain any temporal information about the buildup of Fano resonance.

If we can terminate the autoionization process at $t = \tau > 0$, the induced dipole in

Eq. (6.18) becomes

$$d(t) \propto \begin{cases} i\left[2\delta(t) + \frac{\Gamma}{2}(q-i)^2 e^{-\frac{\Gamma}{2}t} e^{-i\Omega_r t}\right] & 0 \le t < \tau \\ 0 & t \ge \tau \end{cases} \tag{6.21}$$

Then the upper integration in Eq. (6.19) is limited to τ instead of infinity, the absorption cross section becomes

$$\begin{aligned} \sigma(\Omega,\tau) &\propto \mathrm{Re}\left[1 + \frac{(q-i)^2}{1-i\epsilon}\left(1 - e^{-\frac{\Gamma}{2}\tau} e^{i\Delta\Omega\tau}\right)\right] \\ &= \frac{(q+\epsilon)^2}{1+\epsilon^2} - e^{-\frac{\Gamma}{2}\tau}\frac{(1+q^2)}{\sqrt{1+\epsilon^2}}\cos[\Delta\Omega\tau + \varphi(\epsilon)], \end{aligned} \tag{6.22}$$

in which

$$\tan\varphi(\epsilon) = \frac{q^2\epsilon - \epsilon - 2q}{q^2 - 1 + 2q\epsilon}. \tag{6.23}$$

Equation (6.22) shows that photoabsorption cross section depends on when the autoionization is terminated and can be used to probe the time evolution of the buildup of a Fano resonance. To remove the decaying part of the resonance one can use an intense delta pulse to fully ionize the bound state. Conditions very similar to this limit has been used in the experiment reported by Kaldun *et al.*[164].

6.3 Experimental observation versus theoretical calculation

In Kaldun's experiment, the transient buildup of the $2s2p\ ^1P$ resonance of helium was observed. The $2s2p\ ^1P$ resonance has the parameters $\Omega_r = 60.15$ eV, $\Gamma = 37$ meV which corresponds to a lifetime of 17 fs, and $q = -2.75$. An 150 as IAP is used to excite the helium from the ground state with photon range from 50-72 eV and thus triggers the buildup of $2s2p$ resonance at $t = 0$. Then at a delayed time $t = \tau > 0$ a 7 fs, 740 nm near-infrared

laser with intensity of about 10^{13} W/cm^2 was used to ionize the system, depleting the $2s2p$ autoionizing state and terminating the buildup process. Since the IR intensity is high enough and the IR duration is much smaller than the lifetime of the bound state, we can assume the doubly excited state is ionized instantaneously and completely. By changing the time delay between the near-IR with respect to the XUV, the absorption spectrum from each time delay are put together to show the buildup of the $2s2p$ resonance. Figure 6.1 shows the experimental result. For the unperturbed case, that is, in the absence of the near-IR pulse, the original Fano line shape is also depicted in the gray line. When τ is small as compared with the 17 fs lifetime, the short duration in which radiation is emitted by the XUV-triggered dipole oscillation is insufficient to form a well-defined Fano line, as can be seen in Fig. 6.1 for τ less than 10 fs. At $\tau \approx 6$ fs, the effect of the near-IR is the strongest, and the spectral line is smeared out completely. By increasing the time delay τ, the doubly excited state has more time to decay, and the interference with the open channel builds up. This gives rise to a narrower spectral line. After approximately one lifetime, the Fano profile is already more pronounced and continuously narrows down as the time delay is increased. For time delays substantially longer than the lifetime, the original Fano absorption profile is recovered. However, this comparison is limited by the finite experimental resolution (50 meV FWHM), which has a noticeable effect on the narrow unperturbed line.

To ensure that the transient photoabsorption spectrogram shown in Fig. 6.1 indeed can be interpreted as a "movie" of the buildup of the Fano resonance even though it is actually from a photoabsorption experiment by XUV plus IR pulses. In Fig. 6.2 we display the lineout of the resonance profiles at a few time delays from the experiment, the *ab initio* TDSE calculation of the absorption spectra, and the analytical theory predicted by Eq. (6.22). The good agreement of the analytical theory with the other two results confirms that this interpretation is correct in spite of the expected small discrepancies when the near-IR pulse is overlapping with the XUV pulse.

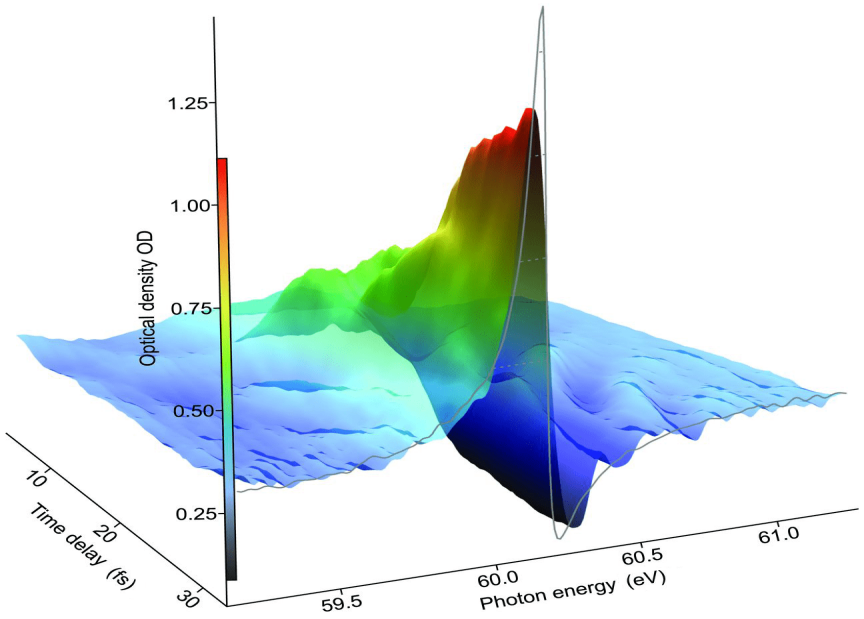

Figure 6.1: *Transient absorption spectrogram of the helium 2s2p resonance as a function of photon energy and time delay $\tau > 0$ after the resonance is excited by a 150 as XUV pulse. At $t = \tau$, an intense 7 fs near-infrared laser pulse was used to completely ionize the bound part of the resonance within the first few femtoseconds of the near-IR pulse. From Ref. [164].*

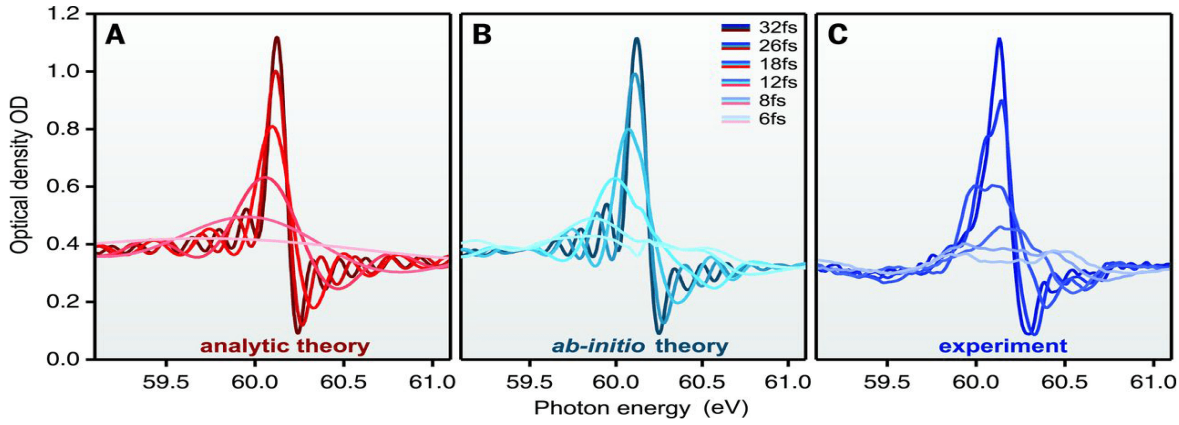

Figure 6.2: *Comparison between analytic theory, ab initio calculation and experimental results for the helium 2s2p Fano line formation. (A) Absorption spectra calculated for a series of time delays between XUV and near-IR according to the analytic expression of Eq. (6.22). (B) Numerically simulated absorption spectra for a 7 fs FWHM near-IR pulse with peak intensity of 20 TW/cm^2. (C) Experimentally recorded spectra. From Ref. [164].*

6.4 Summary and outlook

In this chapter we report the experimental observation of the ultrafast formation of the helium $2s2p$ Fano resonance via high-resolution ATAS. An IAP is applied first to excite the helium atom, then an intense few-cycle near-IR laser pulse is applied which rapidly depletes the excited state via strong-field ionization. The IR pulse in turn terminates the optical response of the atom. In this way we can monitor the buildup of the absorption line. In this experiment the duration of the IR pulse is much shorter than the lifetime of the autoionizing state, and the time delay between the XUV and the IR pulses is controlled with sub-femtosecond precision. An analytical model is derived by us to explain the measured ATAS spectra. The agreement between the experiment and theory demonstrates that the physical mechanism of the time-resolved buildup of the Fano resonance is captured by the measurement. Note that a complementary study by an independent team of researchers[166] observed the formation of the photoelectron spectrum of the very same transition.

The general method of terminating the coherent dipole response by means of laser-driven saturated ionization could be used to temporally resolve the buildup of a wide range of processes that can be tracked via their absorption spectra, for example, the creation of quasi-particles in solids and the emergence of electron-electron or electron-internuclear correlations in molecules, or even more generally, the correlation dynamics in open quantum systems.

Chapter 7

Summary

Isolated attosecond pulses (IAPs) have been applied to ultrafast pump-probe experiments in the past decade in order to detect the attosecond electron dynamics in atoms, molecules and solid-state materials. IAPs are generated by HHG processes taking advantage of various temporal or spatial gating methods. The frequency spectra of IAPs lie in the XUV region and can be extended to soft X-ray covering the water window. Up to now most of the pump-probe experiments are in the XUV plus IR two-color photo-excitation framework, and either the photoelectron distribution or the XUV absorption spectrum is measured. With the help of attosecond pulses, the field of ultrafast physics is moving forward to make real-time electron movies with attosecond temporal resolution, and to control electron wave packets on the attosecond time scale.

Although attosecond experiments are growing rapidly, some basic techniques used to measure the attosecond pulse or electron dynamics such as the FROG-CRAB method have not been carefully calibrated. These methods rely on different models and approximations to describe the experimental data and therefore have their limitations. In this dissertation we checked the accuracy of the FROG-CRAB and the PROOF method in IAP characterization. Photoionization time delay is an attractive topic in attosecond physics and causes a lot of controversy between theory and experiment. To address this issue we investigated the

performance of the widely-used FROG-CRAB in the time delay retrieval process.

Moreover, in this dissertation we include our earlier work on wavelength scaling of the HHG yield using quantum orbit analysis. This work serves as the fundamental of generating attosecond pulses toward the water window or keV region by mid-IR driving laser pulses. At last, we mention our recent work on monitoring the buildup of Fano resonance in helium by attosecond transient absorption spectra, which is another important type of the applications of IAPs. In the following we will summarize the main conclusions in this thesis.

1. **HHG using long-wavelength driving IR**

   At single-atom level, the real part of the born and return time calculated from QO theory converge to the classical born and return time as the driving wavelength increases. The returning wave packets as functions of the scaled photon energy corresponding to a particular quantum orbit also converge to a universal form. At a fixed photon energy, the wavelength dependence of the HHG yield for the long orbit is $\lambda^{-4.6}$ and for the short orbit $\lambda^{-10.4}$. Considering macroscopic propagation, good phase matching tends to select the short orbit. Therefore it is very challenging to obtain efficient macroscopic harmonic emission with long wavelength driving field. The possible solution is to generate a synthesized laser waveform which enhances the short orbit contribution.

2. **Accuracy of FROG-CRAB in IAP characterization**

   For high-energy electrons the FROG-CRAB works accurately in spite of the central momentum approximation and the iterative method so long as the bandwidth is not too broad compared with the central frequency. For low-energy electrons the retrieved IAPs via FROG-CRAB contain up to 10% errors in pulse duration compared with the input pulses. The results show that the IAP extracted via FROG-CRAB is still acceptable although the spectrogram calculated from SFA does not reproduce the spectrogram calculated using TDSE.

3. **Comparison between swPROOF and PROOF**

The original PROOF method is less accurate in retrieving the spectral phases than the modified swPROOF method, which is then reflected in the errors of pulse duration and shape in the time domain. The PROOF method uses approximated dipole transition matrix elements, while the swPROOF is based on an accurate theory so long as the IR intensity is below 10^{12} W/cm^2. Our simulation has proven that the swPROOF method is more universal and robust than the original PROOF method. The main drawback of swPROOF is that in the weak IR field, features of the photoelectron spectra are dominated by the XUV spectral intensity. The spectral phase enters in the FSI terms which is only a small effect. On the other hand, the main advantage of swPROOF that there is no limitation on the bandwidth of the IAP.

4. **Accuracy of time delay retrieval from streaking measurements**

   Due to the insensitivity of the spectrogram to the atomic dipole phase and due to the central momentum approximation in FROG-CRAB, accurate retrieval of the dipole phase is difficult unless the XUV is nearly transform-limited and the spectral bandwidth of the XUV is relatively narrow. Under the most favorable conditions, FROG-CRAB can give the phase difference between two transition dipoles as a function of the photon energy. For low-energy photoelectrons ($E < 30$ eV), due to the inaccuracy of the SFA model, the FROG-CRAB can only retrieve the photoionization time delay qualitatively. At high photoelectron energies, the dipole phase is relatively flat with respect to the energy, thus the retrieved dipole phase will be sensitive to any inaccuracy resulting from the FROG retrieval algorithm, especially if the XUV has some degree of attochirp. In view of this difficulty, the time delay of 21 as reported by Schultze *et al.* may contain intrinsic errors in the retrieval process. We have proposed a procedure based on fitting to retrieve the dipole phase of an unknown target using a well-known reference target, which is applicable for XUV pulses with a broad bandwidth.

5. **Probing the buildup of Fano line shape by ATAS**

By using a short intense IR pulse to deplete the autoionizing state via strong-field ionization, we terminate the induced dipole response of helium atom at time delay τ and thus monitor the buildup of Fano line shape in the ATAS spectra by sweeping the time delay. An analytical model is derived to explain the measured ATAS spectra. The agreement between the experiment and theory demonstrates that the physical mechanism of the time-resolved buildup of the Fano resonance is captured by the measurement.

In the end, a few critical and interesting issues in attosecond physics have been touched in this dissertation. All these studies extend the knowledge about the generation, characterization and the application of attosecond pulses, and they are helpful for experimentalists in the future.

Bibliography

[1] N. F. Scherer, J. L. Knee, D. D. Smith, and A. H. Zewail. Femtosecond photofragment spectroscopy: The reaction ICN $\rightarrow$ CN + I. *J. Chem. Phys.*, 89:5141–5143, 1985.

[2] J. J. Macklin, J. D. Kmetec, and C. L. Gordon III. High-order harmonic generation using intense femtosecond pulses. *Phys. Rev. Lett.*, 70:766–769, 1993.

[3] P. M. Paul, E. S. Toma, P. Breger, G. Mullot, F. Augé, Ph. Balcou, H. G. Muller, and P. Agostini. Observation of a train of attosecond pulses from high harmonic generation. *Science*, 292:1689–1692, 2001.

[4] E. Goulielmakis, M. Schultze, M. Hofstetter, V. S. Yakovlev, J. Gagnon, M. Uiberacker, A. L. Aquila, E. M. Gullikson, D. T. Attwood, R. Kienberger, F. Krausz, and U. Kleineberg. Single-cycle nonlinear optics. *Science*, 320:1614–1617, 2008.

[5] M. Drescher, M. Hentschel, R. Kienberger, M. Uiberacker, V. Yakovlev, A. Scrinzi, Th. Westerwalbesloh, U. Kleineberg, U. Heinzmann, and F. Krausz. Time-resolved atomic inner-shell spectroscopy. *Nature*, 419:803–807, 2002.

[6] M. Schultze, M. Fieß, N. Karpowicz, J. Gagnon, M. Korbman, M. Hofstetter, S. Neppl, A. L. Cavalieri, Y. Komninos, Th. Mercouris, C. A. Nicolaides, R. Pazourek, S. Nagele, J. Feist, J. Burgdörfer, A. M. Azzeer, R. Ernstorfer, R. Kienberger, U. Kleineberg, E. Goulielmakis, F. Krausz, and V. S. Yakovlev. Delay in photoemission. *Science*, 328:1658–1662, 2010.

[7] F. Calegari, D. Ayuso, A. Trabattoni, L. Belshaw, S. De Camillis, S. Anumula, F. Frassetto, L. Poletto, A. Palacios, P. Decleva, J. B. Greenwood, F. Martn, and M. Nisoli.

Ultrafast electron dynamics in phenylalanine initiated by attosecond pulses. *Science*, 346:336–339, 2014.

[8] A. McPherson, G. Gibson, H. Jara, U. Johann, T. S. Luk, I. A. McIntyre, K. Boyer, and C. K. Rhodes. Studies of multiphoton production of vacuum-ultraviolet radiation in the rare gases. *J. Opt. Soc. Am. B*, 4:595–601, 1987.

[9] M. Ferray, A. LHuillier, X. F. Li, L. A. Lompré, G. Mainfray, and C. Manus. Multipleharmonic conversion of 1064 nm radiation in rare gases. *J. Phys. B*, 21:L31–L35, 1988.

[10] A. Rundquist, C. Durfee, Z. Chang, G. Taft, E. Zeek, S. Backus, M.M. Murnane, H.C. Kapteyn, I. Christov, and V. Stoev. Ultrafast laser and amplifier sources. *Appl. Phys. B*, 65:161–174, 1997.

[11] H. Mashiko, C. M. Nakamura, C. Li, E. Moon, H. Wang, J. Tackett, and Z. Chang. Carrier-envelope phase stabilized 5.6 fs, 1.2 mj pulses. *Appl. Phys. Lett.*, 90:161114, 2007.

[12] D. J. Jones, S. A. Diddams, J. K. Ranka, A. Stentz, R. S. Windeler, J. L. Hall, and S. T. Cundiff. Carrier-envelope phase control of femtosecond mode-locked lasers and direct optical frequency synthesis. *Science*, 288:635–639, 2000.

[13] L. V. Keldysh. Ionization in the field of a strong electromagnetic wave (multiphonon absorption processes and ionization probability for atoms and solids in strong electromagnetic field). *Sov. Phys – JETP*, 20:1307–1314, 1965.

[14] J. L. Krause, K. J. Schafer, and K. C. Kulander. High-order harmonic generation from atoms and ions in the high intensity regime. *Phys. Rev. Lett.*, 68:3535–3538, 1992.

[15] P. B. Corkum. Plasma perspective on strong field multiphoton ionization. *Phys. Rev. Lett.*, 71:1994–1997, 1993.

[16] M. Lewenstein, Ph. Balcou, M. Y. Ivanov, A. LHuillier, and P. B. Corkum. Theory of high-harmonic generation by low-frequency laser fields. *Phys. Rev. A*, 49:2117–2132, 1994.

[17] M. B. Gaarde, J. L. Tate, and K. J. Schafer. Macroscopic aspects of attosecond pulse generation. *J. Phys. B*, 41:132001, 2008.

[18] R. López-Martens, K. Varjú, P. Johnsson, J. Mauritsson, Y. Mairesse, P. Salières, M. B. Gaarde, K. J. Schafer, A. Persson, S. Svanberg, C. Wahlström, and A. L'Huillier. Amplitude and phase control of attosecond light pulses. *Phys. Rev. Lett.*, 94:033001, 2005.

[19] T. Pfeifer, A. Jullien, M. J. Abel, P. M. Nagel, L. Gallmann, D. M. Neumark, and S. R. Leone. Generating coherent broadband continuum soft-X-ray radiation by attosecond ionization gating. *Opt. Express*, 15:17120–17128, 2007.

[20] P. B. Corkum, N. H. Burnett, and M. Y. Ivanov. Subfemtosecond pulses. *Opt. Lett.*, 19:1870–1872, 1994.

[21] G. Sansone, E. Benedetti, F. Calegari, C. Vozzi, L. Avaldi, R. Flammini, L. Poletto, P. Villoresi, C. Altucci, R. Velotta, S. Stagira, S. De Silvestri, and M. Nisoli. Isolated single-cycle attosecond pulses. *Science*, 314:443–446, 2006.

[22] Z. Chang. Single attosecond pulse and XUV supercontinuum in the high-order harmonic plateau. *Phys. Rev. A*, 70:043802, 2004.

[23] H. Mashiko, S. Gilbertson, M. Chini, X. Feng, C. Yun, H. Wang, S. D. Khan, S. Chen, and Z. Chang. Extreme ultraviolet supercontinua supporting pulse durations of less than one atomic unit of time. *Opt. Lett.*, 34:3337–3339, 2009.

[24] X. Feng, S. Gilbertson, H. Mashiko, H. Wang, S. D. Khan, M. Chini, Y. Wu, K. Zhao,

and Z. Chang. Generation of isolated attosecond pulses with 20 to 28 femtosecond lasers. *Phys. Rev. Lett.*, 103:183901, 2009.

[25] K. Zhao, Q. Zhang, M. Chini, Y. Wu, X. Wang, and Z. Chang. Tailoring a 67 attosecond pulse through advantageous phasemismatch. *Opt. Lett.*, 37:3891–3893, 2012.

[26] H. Vincenti and F. Quéré. Attosecond lighthouses: how to use spatiotemporally coupled light fields to generate isolated attosecond pulses. *Phys. Rev. Lett.*, 108: 113904, 2012.

[27] K. T. Kim, C. Zhang, T. Ruchon, J. F. Hergott, T. Auguste, D. M. Villeneuve, P. B. Corkum, and F. Quéré. Photonic streaking of attosecond pulse trains. *Nature Photonics*, 7:651–656, 2013.

[28] B. E. Schmidt, A. D. Shiner, M. Giguère, P. Lassonde, C. A. Trallero-Herrero, J. Kieffer, P. B. Corkum, D. M. Villeneuve, and F. Légaré. High harmonic generation with long-wavelength few-cycle laser pulses. *J. Phys. B*, 45:074008, 2012.

[29] T. Popmintchev, M. C. Chen, O. Cohen, M. E. Grisham, J. J. Rocca, M. M. Murnane, and H. C. Kapteyn. Extended phase matching of high harmonics driven by mid-infrared light. *Opt. Lett.*, 33:2128–2130, 2008.

[30] P. Colosimo, G. Doumy, C. I. Blaga, J. Wheeler, C. Hauri, F. Catoire, J. Tate, R. Chirla, A. M. March, G. G. Paulus, H. G. Muller, P. Agostini, and L. F. DiMauro. Scaling strong-field interactions towards the classical limit. *Nature Physics*, 4:386–389, 2008.

[31] E. J. Takahashi, T. Kanai, K. L. Ishikawa, Y. Nabekawa, and K. Midorikawa. Coherent water window X-ray by phase-matched high-order harmonic generation in neutral media. *Phys. Rev. Lett.*, 101:253901, 2008.

[32] N. Ishii, K. Kaneshima, K. Kitano, T. Kanai, S. Watanabe, and J. Itatani. Carrier-envelope phase-dependent high harmonic generation in the water window using few-cycle infrared pulses. *Nature Communication*, 5:3331, 2014.

[33] Y. Deng, A. Schwarz, H. Fattahi, M. Ueffing, X. Gu, M. Ossiander, T. Metzger, V. Pervak, H. Ishizuki, T. Taira, T. Kobayashi, G. Marcus, F. Krausz, R. Kienberger, and N. Karpowicz. Carrier-envelope-phase-stable, 1.2 mJ, 1.5 cycle laser pulses at 2.1 μm. *Opt. Lett.*, 37:4973–4975, 2012.

[34] K.-H. Hong, C. J. Lai, J. P. Siqueira, P. Krogen, J. Moses, C. L. Chang, G. J. Stein, L. E. Zapata, and F. X. Kärtner. Multi-mJ, kHz, 2.1 μm optical parametric chirped-pulse amplifier and high-flux soft X-ray high-harmonic generation. *Opt. Lett.*, 39: 3145–3148, 2014.

[35] Y. Yin, J. Li, X. Ren, K. Zhao, Y. Wu, E. Cunningham, and Z. Chang. High-efficiency optical parametric chirped-pulse amplifier in BiB_3O_6 for generation of 3 mJ, two-cycle, carrier-envelope-phase-stable pulses at 1.7 μm. *Opt. Lett.*, 41:1142–1145, 2016.

[36] A. D. Shiner, C. Trallero-Herrero, N. Kajumba, H. C. Bandulet, D. Comtois, F. Légaré, M. Giguère, J. C. Kieffer, P. B. Corkum, and D. M. Villeneuve. Wavelength scaling of high harmonic generation efficiency. *Phys. Rev. Lett.*, 103:073902, 2009.

[37] T. Popmintchev, M. C. Chen, D. Popmintchev, P. Arpin, S. Brown, S. Ališauskas, G. Andriukaitis, T. Balèiunas, O. D. Mücke, A. Pugzlys, A. Baltuška, B. Shim, S. E. Schrauth, A. Gaeta, C. Hernández-García, L. Plaja, A. Becker, A. Jaron-Becker, M. M. Murnane, and H. C. Kapteyn. Bright coherent ultrahigh harmonics in the keV X-ray regime from mid-infrared femtosecond lasers. *Science*, 336:1287–1291, 2012.

[38] G. Doumy, J. Wheeler, C. Roedig, R. Chirla, P. Agostini, and L. F. DiMauro. Attosecond synchronization of high-order harmonics from mid-infrared drivers. *Phys. Rev. Lett.*, 102:093002, 2009.

[39] F. Silva, S. M. Teichmann, S. L. Cousin, M. Hemmer, and J. Biegert. Spatiotemporal isolation of attosecond soft X-ray pulses in the water window. *Nature Communication*, 6:6611, 2015.

[40] J. Li, X. Ren, Y. Yin, Y. Cheng, E. Cunningham, Y. Wu, and Z. Chang. Polarization gating of high harmonic generation in the water window. *Appl. Phys. Lett.*, 108: 231102, 2016.

[41] C. Iaconis and I. A. Walmsley. Spectral phase interferometry for direct electric-field reconstruction of ultrashort optical pulses. *Opt. Lett.*, 23:792–794, 1998.

[42] R. Trebino, K. W. DeLong, D. N. Fittinghoff, J. N. Sweetser, M. A. Krumbügel, B. A. Richman, and D. J. Kane. Measuring ultrashort laser pulses in the time-frequency domain using frequency-resolved optical gating. *Rev. Sci. Instrum.*, 68:3277–3295, 1997.

[43] H. G. Muller. Reconstruction of attosecond harmonic beating by interference of two-photon transitions. *Appl. Phys. B*, 74:s17–s21, 2002.

[44] Y. Mairesse, A. de Bohan, L. J. Frasinski, H. Merdji, L. C. Dinu, P. Monchicourt, P. Breger, M. Kovačev, R. Taïeb, B. Carré, H. G. Muller, P. Agostini, and P. Salières. Attosecond synchronization of high-harmonic soft X-rays. *Science*, 302:1540–1543, 2003.

[45] M. Hentschel, R. Kienberger, Ch. Spielmann, G. A. Reider, N. Milosevic, T. Brabec, P. Corkum, U. Heinzmann, M. Drescher, and F. Krausz. Attosecond metrology. *Nature*, 414:509–513, 2001.

[46] J. Itatani, F. Quéré, G. L. Yudin, M. Y. Ivanov, F. Krausz, and P. B. Corkum. Attosecond streak camera. *Phys. Rev. Lett.*, 88:173903, 2002.

[47] Y. Mairesse and F. Quéré. Frequency-resolved optical gating for complete reconstruction of attosecond bursts. *Phys. Rev. A*, 71:011401, 2005.

[48] M. Chini, S. Gilbertson, S. D. Khan, and Z. Chang. Characterizing ultrabroadband attosecond lasers. *Opt. Express*, 18:13006–13016, 2010.

[49] K. T. Kim, C. Zhang, A. D. Shiner, S. E. Kirkwood, E. Frumker, G. Gariepy, A. Naumov, D. M. Villeneuve, and P. B. Corkum. Manipulation of quantum paths for space-time characterization of attosecond pulses. *Nature Physics*, 9:159–163, 2013.

[50] K. T. Kim, D. M. Villeneuve, and P. B. Corkum. Manipulating quantum paths for novel attosecond measurement methods. *Nature Photonics*, 8:187–194, 2014.

[51] C. Zhang, G. G. Brown, K. T. Kim, D. M. Villeneuve, and P. B. Corkum. Full characterization of an attosecond pulse generated using an infrared driver. *Scientific Reports*, 6:26771, 2016.

[52] C. Liu, M. Reduzzi, A. Trabattoni, A. Sunilkumar, A. Dubrouil, F. Calegari, M. Nisoli, and G. Sansone. Carrier-envelope phase effects of a single attosecond pulse in two-color photoionization. *Phys. Rev. Lett.*, 111:123901, 2013.

[53] A. T. J. B. Eppink and D. H. Parker. Velocity map imaging of ions and electrons using electrostatic lenses: application in photoelectron and photofragment ion imaging of molecular oxygen. *Rev. Sci. Instrum.*, 68:3477–3484, 1997.

[54] R. Dörner, V. Mergel, O. Jagutzki, L. Spielberger, J. Ullrich, R. Moshammer, and H. Schmidt-Böcking. Cold target recoil ion momentum spectroscopy: a 'momentum microscope' to view atomic collision dynamics. *Phys. Rep.*, 330:95, 2000.

[55] E. Goulielmakis, Z. H. Loh, A. Wirth, R. Santra, N. Rohringer, V. S. Yakovlev, S. Zherebtsov, T. Pfeifer, A. M. Azzeer, M. F. Kling, S. R. Leone, and F. Krausz. Real-time observation of valence electron motion. *Nature*, 466:739–743, 2010.

[56] C. Ott, A. Kaldun, P. Raith, K. Meyer, M. Laux, J. Evers, C. H. Keitel, C. H. Greene, and T. Pfeifer. Lorentz meets fano in spectral line shapes: a universal phase and its laser control. *Science*, 340:716–720, 2013.

[57] A. R. Beck, D. M. Neumark, and S. R. Leone. Probing ultrafast dynamics with attosecond transient absorption. *Chem. Phys. Lett.*, 624:119–130, 2015.

[58] C. Ott, A. Kaldun, L. Argenti, P. Raith, K. Meyer, M. Laux, Y. Zhang, A. Blättermann, S. Hagstotz, T. Ding, R. Heck, J. Madro nero, F. Martín, and T. Pfeifer. Reconstruction and control of a time-dependent two-electron wave packet. *Nature*, 516:374–378, 2014.

[59] M. Uiberacker, Th. Uphues, M. Schultze, A. J. Verhoef, V. Yakovlev, M. F. Kling, J. Rauschenberger, N. M. Kabachnik, H. Schröder, M. Lezius, K. L. Kompa, H. G. Muller, M. J. J. Vrakking, S. Hendel, U. Kleineberg, U. Heinzmann, M. Drescher, and F. Krausz. Attosecond real-time observation of electron tunnelling in atoms. *Nature*, 446:627–632, 2007.

[60] Th. Uphues, M. Schultze, M. F. Kling, M. Uiberacker, S. Hendel, U. Heinzmann, N. M. Kabachnik, and M. Drescher. Ion-charge-state chronoscopy of cascaded atomic Auger decay. *New J. Phys.*, 10:025009, 2008.

[61] R. Pazourek, S. Nagele, and J. Burgdörfer. Attosecond chronoscopy of photoemission. *Rev. Mod. Phys.*, 87:765–802, 2015.

[62] K. Klünder, J. M. Dahlström, M. Gisselbrecht, T. Fordell, M. Swoboda, D. Guénot, P. Johnsson, J. Caillat, J. Mauritsson, A. Maquet, R. Taïeb, and A. LHuillier. Probing single-photon ionization on the attosecond time scale. *Phys. Rev. Lett.*, 106:143002, 2011.

[63] D. Guénot, K. Klünder, C. L. Arnold, D. Kroon, J. M. Dahlström, M. Miranda, T. Fordell, M. Gisselbrecht, P. Johnsson, J. Mauritsson, E. Lindroth, A. Maquet,

R. Taïeb, A. LHuillier, and A. S. Kheifets. Photoemission-time-delay measurements and calculations close to the 3s-ionization-cross-section minimum in Ar. *Phys. Rev. A*, 85:053424, 2012.

[64] D. Guénot, D. Kroon, E. Balogh, E. W. Larsen, M. Kotur, M. Miranda, T. Fordell, P. Johnsson, J. Mauritsson, M. Gisselbrecht, K. Varjù2, C. L. Arnold, T. Carette, A. S. Kheifets, E. Lindroth, A. L'Huillier, and J. M. Dahlström. Measurements of relative photoemission time delays in noble gas atoms. *J. Phys. B*, 47:245602, 2014.

[65] C. Palatchi, J. M. Dahlström, A. Kheifets, I. Ivanov, D. Canaday, P. Agostini, and L. DiMauro. Atomic delay in helium, neon, argon and krypton. *J. Phys. B*, 47:245003, 2014.

[66] M. Sabbar, S. Heuser, R. Boge, M. Lucchini, T. Carette, E. Lindroth, L. Gallmann, C. Cirelli, and U. Keller. Resonance effects in photoemission time delays. *Phys. Rev. Lett.*, 115:133001, 2015.

[67] A. L. Cavalieri, N. Müller, Th. Uphues, V. S. Yakovlev, A. Baltuška, B. Horvath, B. Schmidt, L. Blümel, R. Holzwarth, S. Hendel, M. Drescher, U. Kleineberg, P. M. Echenique, R. Kienberger, F. Krausz, and U. Heinzmann. Attosecond spectroscopy in condensed matter. *Nature*, 449:1029–1032, 2007.

[68] S. Neppl, R. Ernstorfer, E. M. Bothschafter, A. L. Cavalieri, D. Menzel, J. V. Barth, F. Krausz, R. Kienberger, and P. Feulner. Attosecond time-resolved photoemission from core and valence states of magnesium. *Phys. Rev. Lett.*, 109:087401, 2012.

[69] C. H. Zhang and U. Thumm. Attosecond photoelectron spectroscopy of metal surfaces. *Phys. Rev. Lett.*, 102:123601, 2009.

[70] Q. Liao and U. Thumm. Attosecond time-resolved photoelectron dispersion and photoemission time delays. *Phys. Rev. Lett.*, 112:023602, 2014.

[71] Q. Liao and U. Thumm. Attosecond time-resolved streaked photoemission from Mg-covered W(110) surfaces. *Phys. Rev. A*, 92:031401(R), 2015.

[72] F. Calegari, G. Sansone, S. Stagira, C. Vozzi, and M. Nisoli. Advances in attosecond science. *J. Phys. B*, 49:062001, 2016.

[73] S. Neppl, R. Ernstorfer, A. L. Cavalieri, C. Lemell, G. Wachter, E. Magerl, E. M. Bothschafter, M. Jobst, M. Hofstetter, U. Kleineberg, J. V. Barth, D. Menzel, J. Burgdörfer, P. Feulner, F. Krausz, and R. Kienberger. Direct observation of electron propagation and dielectric screening on the atomic length scale. *Nature*, 517:342–346, 2015.

[74] C. Lemell, S. Neppl, G. Wachter, K. Tökési, R. Ernstorfer, P. Feulner, R. Kienberger, and J. Burgdörfer. Real-time observation of collective excitations in photoemission. *Phys. Rev. B*, 91:241101, 2015.

[75] R. Locher, L. Castiglioni, M. Lucchini, M. Greif, L. Gallmann, J. Osterwalder, M. Hengsberger, and U. Keller. Energy-dependent photoemission delays from noble metal surfaces by attosecond interferometry. *Optica*, 2:405–410, 2015.

[76] M. J. Ambrosio and U. Thumm. Comparative time-resolved photoemission from the Cu(100) and Cu(111) surfaces. *Phys. Rev. A*, 94:063424, 2016.

[77] U. Thumm, Q. Liao, E. M. Bothschafter, F. Süßmann, M. F. Kling, and R. Kienberger. *Attosecond physics: attosecond streaking spectroscopy of atoms and solids, in Photonics: Scientific Foundations, Technology and Applications*, volume 1. John Wiley, Inc., Hoboken, NJ, USA, 2015.

[78] G. Sansone, F. Kelkensberg, J. F. Pérez-Torres, F. Morales, M. F. Kling, W. Siu, O. Ghafur, P. Johnsson, M. Swoboda, E. Benedetti, F. Ferrari, F. Lépine, J. L. Sanz-Vicario, S. Zherebtsov, I. Znakovskaya, A. LHuillier, M. Yu. Ivanov, M. Nisoli,

F. Martín, and M. J. J. Vrakking. Electron localization following attosecond molecular photoionization. *Nature*, 465:763–767, 2010.

[79] W. Siu, F. Kelkensberg, G. Gademann, A. Rouzée, P. Johnsson, D. Dowek, M. Lucchini, F. Calegari, U. De Giovannini, A. Rubio, R. R. Lucchese, H. Kono, F. Lépine, and M. J. J. Vrakking. Attosecond control of dissociative ionization of O_2 molecules. *Phys. Rev. A*, 84:063412, 2011.

[80] P. Cörlin, A. Fischer, M. Schönwald, A. Sperl, T. Mizuno, U. Thumm, T. Pfeifer, and R. Moshammer. Probing calculated O_2^+ potential-energy curves with an $\mathrm{XUV} - \mathrm{IR}$ pump-probe experiment. *Phys. Rev. A*, 91:043415, 2015.

[81] M. Lucchini, K. Kim, F. Calegari, F. Kelkensberg, W. Siu, G. Sansone, M. J. J. Vrakking, M. Hochlaf, and M. Nisoli. Autoionization and ultrafast relaxation dynamics of highly excited states in N_2. *Phys. Rev. A*, 86:043404, 2012.

[82] A. Trabattoni, M. Klinker, J. González-Vázquez, C. Liu, G. Sansone, R. Linguerri, M. Hochlaf, J. Klei, M. J. J. Vrakking, F. Martín, M. Nisoli, and F. Calegari. Mapping the dissociative ionization dynamics of molecular nitrogen with attosecond time resolution. *Phys. Rev. X*, 5:041053, 2015.

[83] L. S. Cederbaum and J. Zobeley. Ultrafast charge migration by electron correlation. *Chem. Phys. Lett.*, 307:205–210, 1999.

[84] L. Belshaw, F. Calegari, M. J. Duffy, A. Trabattoni, L. Poletto, M. Nisoli, and J. B. Greenwood. Observation of ultrafast charge migration in an amino acid. *J. Phys. Chem. Lett.*, 3:3751–3754, 2012.

[85] P. M. Kraus, B. Mignolet, D. Baykusheva, A. Rupenyan, L. Horný, E. Penka, G. Grassi, O. Tolstikhin, J. Schneider, and F. Jensen. Measurement and laser control of attosecond charge migration in ionized iodoacetylene. *Science*, 350:790–795, 2015.

[86] K. H. Hong, S. W. Huang, J. Moses, X. Fu, C. J. Lai, G. Cirmi, A. Sell, E. Granados, P. Keathley, and F. X. Kärtner. High-energy, phase-stable, ultrabroadband kHz OPCPA at 2.1 μm pumped by a picosecond cryogenic Yb : YAG laser. *Opt. Express*, 19:15538–15548, 2011.

[87] J. Tate, T. Auguste, H. G. Muller, P. Salières, P. Agostini, and L. F. DiMauro. Scaling of wave-packet dynamics in an intense midinfrared field. *Phys. Rev. Lett.*, 98:013901, 2007.

[88] K. Schiessl, K. L. Ishikawa, E. Persson, and J. Burgdörfer. Quantum path interference in the wavelength dependence of high-harmonic generation. *Phys. Rev. Lett.*, 99: 253903, 2007.

[89] M. V. Frolov, N. L. Manakov, and A. F. Starace. Wavelength scaling of high-harmonic yield: threshold phenomena and bound state symmetry dependence. *Phys. Rev. Lett.*, 100:173001, 2008.

[90] V. S. Yakovlev, M. Ivanov, and F. Krausz. Enhanced phase-matching for generation of soft X-ray harmonics and attosecond pulses in atomic gases. *Opt. Express*, 15: 15351–15364, 2007.

[91] E. L. Falc ao Filho, V. M. Gkortsas, A. Gordon, and F. X. Kärtner. Analytic scaling analysis of high harmonic generation conversion efficiency. *Opt. Express*, 17:11217–11229, 2009.

[92] J. A. Pérez-Hernández, L. Roso, and L. Plaja. Enhanced phase-matching for generation of soft X-ray harmonics and attosecond pulses in atomic gases. *Opt. Express*, 17: 9891–9903, 2009.

[93] D. R. Austin and J. Biegert. Strong-field approximation for the wavelength scaling of high-harmonic generation. *Phys. Rev. A*, 86:023813, 2012.

[94] P. Salières, B. Carré, L. Le Déroff, F. Grasbon, G. G. Paulus, H. Walther, R. Kopold, W. Becker, D. B. Milosevic, A. Sanpera, and M. Lewenstein. Feynman's path-integral approach for intense-laser-atom interactions. *Science*, 292:902–905, 2001.

[95] D. B. Milosevic and W. Becker. Role of long quantum orbits in high-order harmonic generation. *Phys. Rev. A*, 66:063417, 2002.

[96] G. Sansone, C. Vozzi, S. Stagira, and M. Nisoli. Nonadiabatic quantum path analysis of high-order harmonic generation: role of the carrier-envelope phase on short and long paths. *Phys. Rev. A*, 70:013411, 2004.

[97] T. Auguste, F. Catoire, P. Agostini, L. F. DiMauro, C. C. Chirila, V. S. Yakovlev, and P. Salières. Driving-frequency scaling of high-harmonic quantum paths. *New. J. Phys.*, 14:103014, 2012.

[98] A. T. Le, H. Wei, C. Jin, V. N. Tuoc, T. Morishita, and C. D. Lin. Universality of returning electron wave packet in high-order harmonic generation with mid-infrared laser pulses. *Phys. Rev. Lett.*, 113:033001, 2014.

[99] A. T. Le, H. Wei, C. Jin, and C. D. Lin. Strong-field approximation and its extension for high-order harmonic generation with mid-infrared lasers. *J. Phys. B*, 49:053001, 2016.

[100] A. Becker and F. H. M. Faisal. Intense-field many-body S-matrix theory. *J. Phys. B*, 38:R1–R56, 2005.

[101] A. T. Le, R. R. Lucchese, S. Tonzani, T. Morishita, and C. D. Lin. Quantitative rescattering theory for high-order harmonic generation from molecules. *Phys. Rev. A*, 80:013401, 2009.

[102] F. H. M. Faisal. Multiple absorption of laser photons by atoms. *J. Phys. B*, 6:L89–L92, 1973.

[103] H. R. Reiss. Effect of an intense electromagnetic field on a weakly bound system. *Phys. Rev. A*, 22:1786–1813, 1980.

[104] D. B. Milosevic, G. G. Paulus, and W. Becker. High-order above-threshold ionization with few-cycle pulse: a meter of the absolute phase. *Opt. Express*, 11:1418–1429, 2003.

[105] Z. Chen, T. Morishita, A. T. Le, and C. D. Lin. Analysis of two-dimensional high-energy photoelectron momentum distributions in the single ionization of atoms by intense laser pulses. *Phys. Rev. A*, 76:043402, 2007.

[106] M. V. Ammosov, N. B. Delone, and V. P. Krainov. Tunnel ionization of complex atoms and of atomic ions in an alternating electromagnetic field. *Sov. Phys – JETP*, 64:1191–1194, 1986.

[107] V. P. Krainov and V. M. Ristic. Electron energy spectra in tunneling ionization of atoms and ions by a strong low-frequency electromagnetic field. *Sov. Phys – JETP*, 74:789–792, 1992.

[108] M. B. Gaarde and K. J. Schafer. Quantum path distributions for high-order harmonics in rare gas atoms. *Phys. Rev. A*, 65:031406, 2002.

[109] J. A. Pérez-Hernández, J. Ramos, L. Roso, and L. Plaja. Harmonic generation beyond the strong-field approximation: phase and temporal description. *Laser Phys.*, 20:1044–1050, 2010.

[110] R. Kopold, D. B. Milosevic, and W. Becker. Rescattering processes for elliptical polarization: a quantum trajectory analysis. *Phys. Rev. Lett.*, 84:3831–3834, 2000.

[111] M. V. Frolov, N. L. Manakov, T. S. Sarantseva, M. Y. Emelin, M. Y. Ryabikin, and A. F. Starace. Analytic description of the high-energy plateau in harmonic generation by atoms: can the harmonic power increase with increasing laser wavelengths? *Phys. Rev. Lett.*, 102:243901, 2009.

[112] C. Hernández-García, J. A. Pérez-Hernández, T. Popmintchev, M. M. Murnane, H. C. Kapteyn, A. Jaron-Becker, A. Becker, and L. Plaja. Zeptosecond high harmonic keV X-ray waveforms driven by mid-infrared laser pulses. *Phys. Rev. Lett.*, 111:033002, 2013.

[113] L. He, Y. Li, Z. Wang, Q. Zhang, P. Lan, and P. Lu. Quantum trajectories for high-order-harmonic generation from multiple rescattering events in the long-wavelength regime. *Phys. Rev. A*, 89:053417, 2014.

[114] C. Jin, G. Wang, H. Wei, A. T. Le, and C. D. Lin. Waveforms for optimal sub-keV high-order harmonics with synthesized two- or three-colour laser fields. *Nature Communications*, 5:4003, 2014.

[115] M. Kitzler, N. Milosevic, A. Scrinzi, F. Krausz, and T. Brabec. Quantum theory of attosecond XUV pulse measurement by laser dressed photoionization. *Phys. Rev. Lett.*, 88:173904, 2002.

[116] X. M. Tong and C. D. Lin. Empirical formula for static field ionization rates of atoms and molecules by lasers in the barrier-suppression regime. *J. Phys. B*, 38:2593–2600, 2005.

[117] J. W. Cooper. Photoionization from outer atomic subshells. a model study. *Phys. Rev.*, 128:681–693, 1962.

[118] V. S. Yakovlev, J. Gagnon, N. Karpowicz, and F. Krausz. Attosecond streaking enables the measurement of quantum phase. *Phys. Rev. Lett.*, 105:073001, 2010.

[119] D. J. Kane. Recent progress toward real-time measurement of ultrashort laser pulses. *IEEE J. Quantum Electron.*, 35:421–431, 1999.

[120] J. Gagnon, E. Goulielmakis, and V. S. Yakovlev. The accurate FROG characterization of attosecond pulses from streaking measurements. *Appl. Phys. B*, 92:25–32, 2008.

[121] Z. Chen, T. Morishita, A. T. Le, M. Wickenhauser, X. M. Tong, and C. D. Lin. Analysis of two-dimensional photoelectron momentum spectra and the effect of the long-range coulomb potential in single ionization of atoms by intense lasers. *Phys. Rev. A*, 74:053405, 2006.

[122] T. Morishita, Z. Chen, S. Watanabe, and C. D. Lin. Two-dimensional electron momentum spectra of argon ionized by short intense lasers: Comparison of theory with experiment. *Phys. Rev. A*, 75:023407, 2007.

[123] H. Wei, T. Morishita, and C. D. Lin. Critical evaluation of attosecond time delays retrieved from photoelectron streaking measurements. *Phys. Rev. A*, 93:053412, 2016.

[124] H. Wei, A. T. Le, T. Morishita, C. Yu, and C. D. Lin. Benchmarking accurate spectral phase retrieval of single attosecond pulses. *Phys. Rev. A*, 91:023407, 2015.

[125] J. M. Dahlström and E. Lindroth. Study of attosecond delays using perturbation diagrams and exterior complex scaling. *J. Phys. B*, 47:124012, 2014.

[126] J. M. Dahlström, A. L'Huillier, and A. Maquet. Introduction to attosecond delays in photoionization. *J. Phys. B*, 45:183001, 2012.

[127] J. M. Dahlström, D. Guénot, K. Klünder, M. Gisselbrecht, J. Mauritsson, A. L'Huillier, A. Maquet, and R. Taïeb. Theory of attosecond delays in laser-assisted photoionization. *Chem. Phys.*, 414:53–64, 2013.

[128] E. S. Toma and H. G. Muller. Calculation of matrix elements for mixed extreme-ultravioletinfrared two-photon above-threshold ionization of argon. *J. Phys. B*, 35: 3435–3442, 2002.

[129] A. Maquet and R. Taïeb. Two-colour IR + XUV spectroscopies: the "soft-photon approximation". *J. Mod. Opt.*, 54:1847–1857, 2007.

[130] A. J. Galán, L. Argenti, and F. Martín. The soft-photon approximation in infrared-laser-assisted atomic ionization by extreme-ultraviolet attosecond-pulse trains. *New. J. Phys.*, 15:113009, 2013.

[131] G. Laurent, W. Cao, I. Ben-Itzhak, and C. L. Cocke. Attosecond pulse characterization. *Opt. Express*, 21:16914–16927, 2013.

[132] M. Lucchini, M. H. Brügmann, A. Ludwig, L. Gallmann, U. Keller, and T. Feurer. Ptychographic reconstruction of attosecond pulses. *Opt. Express*, 23:29502–29513, 2015.

[133] P. D. Keathley, S. Bhardwaj, J. Moses, G. Laurent, and F. X. Kärtner. Volkov transform generalized projection algorithm for attosecond pulse characterization. *New. J. Phys.*, 18:073009, 2016.

[134] E. P. Wigner. Lower limit for the energy derivative of the scattering phase shift. *Phys. Rev.*, 89:145–147, 1955.

[135] S. Nagele, R. Pazourek, J. Feist, and J. Burgdörfer. Time shifts in photoemission from a fully correlated two-electron model system. *Phys. Rev. A*, 85:033401, 2012.

[136] A. S. Kheifets and I. A. Ivanov. Delay in atomic photoionization. *Phys. Rev. Lett.*, 105:233002, 2010.

[137] A. S. Kheifets. Time delay in valence-shell photoionization of noble-gas atoms. *Phys. Rev. A*, 87:063404, 2013.

[138] J. M. Dahlström, T. Carette, and E. Lindroth. Diagrammatic approach to attosecond delays in photoionization. *Phys. Rev. A*, 86:061402, 2012.

[139] L. R. Moore, M. A. Lysaght, J. S. Parker, H. W. van der Hart, and K. T. Taylor. Time delay between photoemission from the 2p and 2s subshells of neon. *Phys. Rev. A*, 84: 061404, 2011.

[140] O. Zatsarinny and C. F. Fischer. Atomic structure calculations using MCHF and BSR. *Comput. Phys. Commun.* , 180:2041–2065, 2009.

[141] J. Feist, O. Zatsarinny, S. Nagele, R. Pazourek, J. Burgdörfer, X. Guan, K. Bartschat, and B. I. Schneider. Time delays for attosecond streaking in photoionization of neon. *Phys. Rev. A*, 89:033417, 2014.

[142] C. H. Zhang and U. Thumm. Electron-ion interaction effects in attosecond time-resolved photoelectron spectra. *Phys. Rev. A*, 82:043405, 2010.

[143] R. Pazourek, J. Feist, S. Nagele, and J. Burgdörfer. Attosecond streaking of correlated two-electron transitions in helium. *Phys. Rev. Lett.*, 108:163001, 2012.

[144] F. T. Smith. Lifetime matrix in collision theory. *Phys. Rev.*, 118:349–356, 1960.

[145] L. Eisenbud. *The formal properties of nuclear collisions*. PhD thesis, Princeton University, 1948.

[146] A. Maquet, J. Caillat, and R. Taïeb. Attosecond delays in photoionization: time and quantum mechanics. *J. Phys. B*, 47:204004, 2014.

[147] S. Nagele, R. Pazourek, J. Feist, K. Doblhoff-Dier, C. Lemell, K. Tokési, and J. Burgdörfer. Time-resolved photoemission by attosecond streaking: extraction of time information. *J. Phys. B*, 44:081001, 2011.

[148] C. D. Lin. Channel interaction and threshold behavior of photoionization. *Phys. Rev. A*, 9:171–180, 1974.

[149] D. L. Carroll, FORTRAN genetic algorithm driver (1999); http://cuaerospace.com/Technology/GeneticAlgorithm/GADriverFreeVersion.aspx.

[150] U. Fano. Effects of configuration interaction on intensities and phase shifts. *Phys. Rev.*, 124:1866–1877, 1961.

[151] H. Wang, M. Chini, S. Chen, C. Zhang, F. He, Y. Cheng, Y. Wu, U. Thumm, and Z. Chang. Attosecond time-resolved autoionization of argon. *Phys. Rev. Lett.*, 105: 143002, 2010.

[152] X. Wang, M. Chini, Y. Cheng, Y. Wu, X. Tong, and Z. Chang. Subcycle laser control and quantum interferences in attosecond photoabsorption of neon. *Phys. Rev. A*, 87: 063413, 2013.

[153] B. Bernhardt, A. R. Beck, X. Li, E. R. Warrick, M. J. Bell, D. J. Haxton, C. W. McCurdy, D. M. Neumark, and S. R. Leone. High-spectral-resolution attosecond absorption spectroscopy of autoionization in xenon. *Phys. Rev. A*, 89:023408, 2014.

[154] S. Chen, M. J. Bell, A. R. Beck, H. Mashiko, M. Wu, A. N. Pfeiffer, M. B. Gaarde, D. M. Neumark, S. R. Leone, and K. J. Schafer. Light-induced states in attosecond transient absorption spectra of laser-dressed helium. *Phys. Rev. A*, 86:063408, 2012.

[155] M. B. Gaarde, C. Buth, J. L. Tate, and K. J. Schafer. Transient absorption and reshaping of ultrafast XUV light by laser-dressed helium. *Phys. Rev. A*, 83:013419, 2011.

[156] M. Chini, B. Zhao, H. Wang, Y. Cheng, S. X. Hu, and Z. Chang. Subcycle ac stark shift of helium excited states probed with isolated attosecond pulses. *Phys. Rev. Lett.*, 109:073601, 2012.

[157] S. Pabst, A. Sytcheva, A. Moulet, A. Wirth, E. Goulielmakis, and R. Santra. Theory of attosecond transient-absorption spectroscopy of krypton for overlapping pump and probe pulses. *Phys. Rev. A*, 86:063411, 2012.

[158] W. C. Chu and C. D. Lin. Absorption and emission of single attosecond light pulses in an autoionizing gaseous medium dressed by a time-delayed control field. *Phys. Rev. A*, 87:013415, 2013.

[159] M. Wu, S. Chen, S. Camp, K. J. Schafer, and M. B. Gaarde. Theory of strong-field attosecond transient absorption. *J. Phys. B*, 49:062003, 2016.

[160] M. Chini, X. Wang, Y. Cheng, Y. Wu, D. Zhao, D. A. Telnov, S. I. Chu, and Z. Chang. Sub-cycle oscillations in virtual states brought to lght. *Sci. Rep.* , 3:1105, 2013.

[161] S. Chen, M. Wu, M. B. Gaarde, and K. J. Schafer. Quantum interference in attosecond transient absorption of laser-dressed helium atoms. *Phys. Rev. A*, 87:033408, 2013.

[162] A. R. Beck, B. Bernhardt, E. R. Warrick, M. Wu, S. Chen, M. B. Gaarde, K. J. Schafer, D. M. Neumark, and S. R. Leone. Attosecond transient absorption probing of electronic superpositions of bound states in neon: detection of quantum beats. *New. J. Phys.*, 16:113016, 2014.

[163] Y. Cheng, M. Chini, X. Wang, A. González-Castrillo, A. Palacios, L. Argenti, F. Martín, and Z. Chang. Reconstruction of an excited-state molecular wave packet with attosecond transient absorption spectroscopy. *Phys. Rev. Lett.*, 94:023403, 2016.

[164] A. Kaldun, A. Blättermann, V. Stooß, S. Donsa, H. Wei, R. Pazourek, S. Nagele, C. Ott, C. D. Lin, J. Burgdörfer, and T. Pfeifer. Observing the ultrafast buildup of a Fano resonance in the time domain. *Science*, 354:738–741, 2016.

[165] W. C. Chu and C. D. Lin. Theory of ultrafast autoionization dynamics of Fano resonances. *Phys. Rev. A*, 82:053415, 2010.

[166] V. Gruson, L. Barreau, Á. Jiménez-Galan, F. Risoud, J. Caillat, A. Maquet, B. Carré, F. Lepetit, J. F. Hergott, T. Ruchon, L. Argenti, R. Taïeb, F. Martín, and P. Salières. Attosecond dynamics through a Fano resonance: monitoring the birth of a photoelectron. *Science*, 354:734–738, 2016.

Publications

1. A. Kaldun, A. Blättermann, V. Stooß, S. Donsa, **H. Wei**, R. Pazourek, S. Nagele, C. Ott, C. D. Lin, J. Burgdörfer, and T. Pfeifer. Observing the ultrafast buildup of a Fano resonance in the time domain. *Science*, 354:738–741, 2016.

2. **Hui Wei**, Toru Morishita, and C. D. Lin. Critical evaluation of attosecond time delays retrieved from photoelectron streaking measurements. *Phys. Rev. A*, 93:053412, 2016.

3. Anh-Thu Le, **Hui Wei**, Cheng Jin, and C. D. Lin. Strong-field approximation and its extension for high-order harmonic generation with mid-infrared lasers. *J. Phys. B*, 49:053001, 2016.

4. **Hui Wei**, Anh-Thu Le, Toru Morishita, Chao Yu, and C. D. Lin. Benchmarking accurate spectral phase retrieval of single attosecond pulses. *Phys. Rev. A*, 91:023407, 2015.

5. Chao Yu, **Hui Wei**, Xu Wang, Anh-Thu Le, Ruifeng Lu, and C. D. Lin. Reconstruction of two-dimensional molecular structure with laser-induced electron diffraction from laser-aligned polyatomic molecules. *Scietific Reports*, 5:15753, 2015.

6. Anh-Thu Le, **Hui Wei**, Cheng Jin, Vu Ngoc Tuoc, Toru Morishita, and C. D. Lin. Universality of returning electron wave packet in high-order harmonic generation with midinfrared laser pulses. *Phys. Rev. Lett.*, 113:033001, 2014.

7. Cheng Jin, Guoli Wang, **Hui Wei**, Anh-Thu Le, and C. D. Lin. Waveforms for optimal sub-keV high-order harmonics with synthesized two- or three-colour laser fields. *Nature Communications*, 5:4003, 2014.

8. Qianguang Li, Xiao-Min Tong, Toru Morishita, **Hui Wei**, and C. D. Lin. Fine structures in the intensity dependence of excitation and ionization probabilities of hydrogen atoms in intense 800-nm laser pulses. *Phys. Rev. A*, 89:023421, 2014.

9. Qianguang Li, Xiao-Min Tong, Toru Morishita, Cheng Jin, **Hui Wei**, and C. D. Lin. Rydberg states in the strong field ionization of hydrogen by 800, 1200 and 1600nm lasers. *J. Phys. B*, 47:204019, 2014.

Appendix A

Abbreviations

IAP	Isolated attosecond pulse
XUV	Extreme ultraviolet
HHG	High-order harmonic generation
IR	Infrared
APT	Attosecond pulse train
CEP	Carrier-envelope phase
SFA	Strong-field approximation
PG	Polarization gating
DOG	Double-optical gating
GDOG	Generalized DOG
SPIDER	Spectral phase interferometry for direct electric field reconstruction
FROG	Frequency-resolved optical gating
RABITT	Reconstruction of attosecond beating by interference of two-photon transitions
FROG-CRAB	Frequency-resolved optical gating for complete reconstruction of attosecond bursts
PROOF	Phase retrieval by omega oscillation filtering
swPROOF	scattering wave PROOF

CPA	Chirped pulse amplification
OPA	Optical parametric amplification
OPCPA	Optical parametric chirped pulse amplification
ATI	Above threshold ionization
VMI	Velocity map imaging
COLTRIMS	Cold target recoil ion momentum spectroscopy
ATAS	Attosecond transient absorption spectroscopy
FWHM	Full width at half maximum
TL	Transform-limited
RPAE	Random-phase approximation with exchange
TDSE	time-dependent Schrödinger equation
QO	Quantum orbit
QRS	Quantitative rescattering theory
SAE	Single-active-electron
KFR	Keldysh-Faisal-Reiss
ADK	Ammosov-Delone-Krainov
GDD	Group delay dispersion
PCGPA	Principal component generalized projection algorithm
LSGPA	Least square generalized projection algorithm
DVR	Discrete variable representation
GA	Genetic algorithm
FSI	first-second-order interference
C-C	Continuum-continuum
MBPT	Many-body perturbation theory
CLC	Coulomb-laser-coupling
DLC	Dipole-laser coupling

Appendix B

Copyright approval from the publishers

Dear Hui Wei,

I apologise for the inconvenience you have experienced using the CCC Republication Service, and I will now grant your intended reuse via email.

Thank you for your email and for taking the time to seek this permission.

Regarding:

Anh-Thu Le et al 2016 J. Phys. B: At. Mol. Opt. Phys. 49 053001

When you transferred the copyright in your article to us and chose to publish on a subscription basis, we granted back to you certain rights. This included the right to include all or part of the Final Published Version of the article within a thesis or dissertation provided it was not then published commercially. Please note you may need to obtain separate permission for any third party content you included within your article.

We are happy for your thesis or dissertation to be made available via your institution's library and/or your institutional repository.
You may submit your thesis or dissertation (including the article) via ProQuest if that is a requirement of your university. However, we do not then allow the article to be published commercially or made publicly available by ProQuest, so it would need to be removed from your thesis or dissertation prior to publication online or in print. Your institution should be able to withhold the IOP article section of your thesis from the ProQuest version. However, you should still reference the article, include the abstract and provide a DOI link to it on IOPscience so that people know that it has been published.

Any other commercial use of your thesis or dissertation would also require our permission, if it included your IOP article.

Please include citation details, "© IOP Publishing. Reproduced with permission. All rights reserved" and for online use, a link to the Version of Record.

Please note, if your article was published on a gold open access basis, then you would be able to publish your article with ProQuest and use it for any other commercial purpose under the terms of the CC BY licence.

In the meantime, I wish you the best of luck with the completion of your dissertation.

Many thanks.

Kind regards,

Kathryn Shaw

Copyright & Permissions Team
Gemma Alaway – Senior Rights & Permissions Adviser
Kathryn Shaw - Rights & Permissions Assistant

Contact Details
E-mail: permissions@iop.org

For further information: http://iopscience.iop.org/page/copyright

Please see our Author Rights Policy http://ioppublishing.org/author-rights/

Please note: We do not provide signed permission forms as a separate attachment. Please print this email and provide it to your institution as proof of permission.

Please note: Any statements made by IOP Publishing to the effect that authors do not need to get permission to use any content where IOP Publishing is not the publisher is not intended to constitute any sort of legal advice. Authors must make their own decisions as to the suitability of the content they are using and whether they require permission for it to be published within their article.

Dear Hui Wei:

Thank you very much for getting in touch. This letter is to inform you of AAAS's policy on author use of his/her AAAS journal article(s) in a thesis or dissertation that he/she is writing.

After publication of a manuscript in a AAAS journal:

1. The author may reprint figure(s)/table(s) in print and electronic format, in a thesis or dissertation written by the author as part of a course of study at an educational institution.
Credit must be given to the first appearance of the material in the appropriate issue of the AAAS journal.

2. The author may reprint his/her manuscript (the entire article), in print format, in a thesis or dissertation written by the author as part of a course of study at an educational institution. Credit must be given to the first appearance of the material in the appropriate issue of the AAAS journal.

3. If the thesis or dissertation is to be published in electronic format, the accepted version of the manuscript (the accepted version of the paper before Science's copy-editing and production) should be used and a link to the work on the AAAS journal website included.

4. Permission covers the distribution of your thesis or dissertation on demand by a third party distributor (e.g. ProQuest / UMI), provided the AAAS material covered by this permission remains in situ and is not distributed by that third party outside of the context of your thesis or dissertation.

5. The author may not permit others to reproduce the AAAS journal manuscript in a thesis or dissertation. In these cases, requesting parties should be instructed to contact AAAS directly for permission.

If you have any questions regarding this policy, please just let me know.

Kind regards,

(Ms.) Elizabeth Sandler
Rights & Permissions
Science/AAAS
1200 New York Ave. NW
Washington, DC 20005
Tel: + 1-202-326-6765
esandler@aaas.org

Dear Dr. Wei,

Thank you for writing. Kindly refer to our Copyright FAQ located at https://journals.aps.org/copyrightFAQ.html, specifically:

Q) – "As the author of an APS-published article, may I include my article or a portion of my article in my thesis or dissertation?"

A) – "Yes, the author has the right to use the article or a portion of the article in a thesis or dissertation without requesting permission from APS, provided the bibliographic citation and the APS copyright credit line are given on the appropriate pages."

I hope this is helpful to you.

Sincerely,

Michele Hake
help@aps.org